Imperial College
London

Slow, cold beams of polar molecules for precision measurements

By
Nicholas Edward Bulleid

Thesis submitted in partial fufillment of the
requirements for the degree of
Doctor of Philosophy in Physics
of
Imperial College London

October 4, 2013

Declaration

I declare that this thesis is my own work. Where I have used the work of others the sources are appropriately references and acknowledged.

Previous Publications

Parts of this thesis have been published in the following articles:

X. Zhuang, A. Le, T. C. Steimle, N. E. Bulleid, I. J. Smallman, R. J. Hendricks, S. M. Skoff, J. J. Hudson, B. E. Hinds and M. R. Tarbutt, Franck-Condon factors and radiative lifetime of the $A^2\Pi_{1/2}$-$X^2\Sigma_+$ transition of ytterbium monofluoride, YbF, *Physical Chemistry Chemical Physics*, **13**, 19013, (2011)

N. E. Bulleid, R. J. Hendricks, E. A. Hinds, S. A. Meek, G. Meijer, A. Osterwalder and M. R. Tarbutt, Traveling-wave deceleration of heavy polar molecules in low-field-seeking states, *Physical Review A: Atomic, Molecular, and Optical Physics*, **86**, 021404, (2012)

N. E. Bulleid, S. M. Skoff, R. J. Hendricks, B. E. Sauer, E. A. Hinds and M. R. Tarbutt, Characterization of a cryogenic beam source for atoms and molecules, *Physical Chemistry Chemical Physics*, **15**, 12299, (2013)

Abstract

This thesis reports on the use of buffer gas cooling to produce slow and intense molecular beams, with the aim of creating a source of molecules that can be used to measure the electron electric dipole moment. A beam of Yb is extracted from a buffer gas cell by entrainment in a flow of helium. The beam is characterised and simulations are performed of the helium flow through the cell to better understand the effect this has on the beam characteristics. The velocity of the beam is found to vary between $65\,\mathrm{m\,s^{-1}}$ and $204\,\mathrm{m\,s^{-1}}$ depending on the helium flow through the cell, in agreement with the predictions of the simulations. The temperature of the beam is 2.4 K and the minimum divergence is 12°. The percentage of Yb that is extracted from the cell is ~10%.

Sources which use a pulsed valve to produce a supersonic jet are also characterised at cryogenic temperatures. The addition of a thermalisation cell is found to produce beams that are slower, colder and more intense. The peak beam intensity is 4.5×10^{10} molecules per seradian per pulse, the velocity $(206 \pm 5)\,\mathrm{m\,s^{-1}}$ and the translational temperature is $(12.3 \pm 0.5)\,\mathrm{K}$.

An electric decelerator is used to decelerate a pulse of YbF molecules from $300\,\mathrm{m\,s^{-1}}$ to $276\,\mathrm{m\,s^{-1}}$ by confining them to a travelling trap. Simulations of the molecules in the decelerator show that its acceptance is greater than those demonstrated previously. A detailed understanding of this deceleration is developed.

The Franck-Condon factors for the $A^2\Pi_{1/2}(v = 0) - X^2\Sigma^+(v = 0, 1, 2)$ transition of YbF are measured. The results show that, using three lasers, the molecule could be laser-cooled.

Acknowledgements

I would like to thank my supervisors, Mike Tarbutt and Ben Sauer, for their guidance throughout the course of my PhD. I would also like to thank Ed Hinds and Danny Segal for their insight and assistance during our weekly meetings, and Sam Meek and Andreas Osterwalder for our collaboration. I am grateful to Jon Dyne and Steve Maine for their help in the workshop, many parts of the experiment would never have existed without them. Thanks to the support staff at Cd-adapco for answering my many questions about CFD and thanks also to Sanja Maricic for keeping everything organised and always looking out for me. This thesis would not have been possible without Team Buffer Gas and I'd like to thank Rich Hendricks and Sarah Skoff for making me feel at home in the lab. Thanks also to the rest of the CCM for making my time at Imperial such a pleasure. Finally I'd like to thank my friends and family for their support before, during and after my PhD.

Contents

List of Figures

List of Tables

Chapter 1

Introduction

1.1 Cold molecules

The production of cold atoms has always been of great interest for precision measurements [1]. Notable measurements include the definition of the second using a Caesium fountain [2], the measurement of the fine structure constant photon recoil of Rubidium [3] and determination of the Rydberg constant from spectroscopy of atomic hydrogen [4, 5]. Sources of cold, slow-moving molecules would increase the number of fundamental physics measurements that can be undertaken as molecules have properties that atoms do not, such as chirality [6] and large electric dipole moments [7, 8]. These properties also help to improve the current generation of precision measurements, such as the electron EDM measurement [9, 10].

Cold molecules have many other potential and realised applications. As the temperature of the molecules is decreased it becomes possible to control the collisions of molecules with external electric fields. Reaction dynamics of these molecules can then be studied in more detail [11, 12]. A Bose-Einstein condensate (BEC) can be formed from a high density molecular gas at low temperatures. This creates the possibility of having a BEC where the dominant particle interaction is via dipole-dipole forces and the stability is influenced by the trapping geometry [7]. Schemes for trapping cold molecules have been proposed and tested [13, 14], along with a method for using these trapped molecules as a basis for a quantum computer [15].

Methods for creating the cold, slow-moving molecules necessary for these applications are more complex than for atoms, just as molecules have a more complicated internal structure than atoms. Laser cooling, the mainstay of cold atom research, is only feasible

with a small subset of molecules due to the effect this complexity has on the decay channels for an excited electron in a molecule. As the atoms in a molecule can vibrate with respect to each other every electronic energy level is split into several vibrational levels. In turn these are split into rotational energy levels, from the rotation of one atom around the other. An electron has some probability of decaying to any vibrational state so there is some probability that an electron will decay to a state that it cannot be excited from, reducing the number of photons that can be scattered. Extra lasers operating at different frequencies can be used to increase the number of photons scattered, and so increase the amount of thermal energy that can be removed from the molecule. The number of extra lasers that are required depends on the Franck-Condon factors of the vibrational levels. This is the probability that an electron will decay to a particular vibrational level and can be used to calculate the number of photons which will be scattered before the electron decays to a dark state. Recently laser cooling of molecules has been achieved with SrF [16], YO [17] and CaF [18]. In the experiment to decelerate SrF three lasers were required to scatter $\gtrsim 10^4$ photons, which reduced the velocity of the molecules from $\sim 140\,\mathrm{m\,s^{-1}}$ to $< 50\,\mathrm{m\,s^{-1}}$.

As laser cooling can only be applied to certain molecules a variety of other techniques have been developed to produce and trap cold ensembles of molecules. Indirect methods of creating cold molecules, in which pre-cooled atoms are combined to form molecules, have been explored. Both photoassociation [19, 20] and Feshbach resonances [21] can be used to produce molecules when two atoms collide. The first works by exciting the colliding atoms into a bound state with a resonant photon and the second by magnetically tuning a bound state of the molecule into resonance with the free atom state. Both these processes produce molecules in highly vibrational, weakly bound states so an optical transfer is required to obtain molecules in their ground vibrational state [22, 23]. Molecular Bose-Einstein condensates have been observed by using a Feshbach resonance to convert a cold Fermi gas of atoms into a cold gas of molecules [24].

A direct method for producing cold molecules is to mix an ensemble of hot molecules with pre-cooled atoms. This can be done by trapping both atoms and molecules in a single trap and allowing them to thermalise. This sympathetic cooling has been used to cool molecular ions [25] but can also be used with neutral molecules [26]. For electric field traps the molecule atom pair must be chosen carefully to reduce the percentage of collisions that are inelastic, as these can cause the molecules to be lost from the trap. These losses can be

reduced if a microwave trap is used [27]. An alternative method for cooling hot molecules with cold atoms is buffer gas cooling. Here the atoms are confined in a cryogenically cooled copper chamber and transfer translational energy from the molecules to the walls of the chamber. Once the molecules have been cooled they are confined by an external magnetic field [28]. To prevent the molecules from reaching the walls of the chamber, where they would condense and be lost, a high density of atoms is required. The atomic species used as a buffer gas must then be chosen such that the vapour pressure is significant at cryogenic temperatures [29].

Some of the methods used to trap molecules requre them to be travelling slowly before they can be loaded into the trap. This can be achieved by velocity filtering a beam, to obtain a slower selection of molecules. An early method for velocity filtering used a series of rotating disks to select a particular velocity class of a molecular beam [30]. Curved magnetic [31] and electrostatic [32] guides can be used to extract the slow tail in the velocity distribution of a beam of particles. Molecules that are travelling too fast to be confined by the electric or magnetic fields will not be guided round the curve and so be removed from the beam.

Beyond simply filtering the velocity of a molecular beam lies deceleration of the beam. A number of schemes have been explored that focus on utilising the interaction between molecules and inhomogeneous electric or magnetic fields [33]. Depending on the state of the molecule it will experience a force either towards or away from an area of high field. Molecules in that state are then high or low field seekers. Decelerators have been designed which can slow both low [34, 35] and high [36, 37] field seekers. To reduce the length of a decelerator, molecules can be excited to a Rydberg state [38]. These states have a high electric dipole moment so the molecules experience an enhanced force due to the Stark effect. Decelerators have also been built which confine molecules in three dimensional traps that travel with the molecules though the decelerator using electric [39] and magnetic [40] fields. This method of deceleration can be applied to molecules in a state which becomes high field seeking at low energies as the molecules remain close to the zero point of the field. By chirping the frequency of the traps the molecules can be decelerated and even held at rest [41].

Other schemes for slowing molecular beams have been developed. Photostop is a technique where a molecule is photodissociated such that the excess kinetic energy imparted by the photon to the dissociating fragments cancels out the forward motion of the molecules.

This has been experimentally verified for molecules of NO made from NO_2 [42]. A beam of NO has also been slowed to low velocities in the lab frame through collisions with an Ar beam [43]. Fulton *et al* have successfully slowed a molecular beam using the interaction between an induced dipole moment and a deep periodic optical lattice [44]. The lattice is created by crossing two near-counterpropagating laser beams.

These are some methods for cooling an ensemble of molecules, and for slowing a beam of molecules. In the following section different procedures that have been used to create beams of molecules are discussed.

1.2 Molecular beams

1.2.1 Supersonic jets

A method for creating a beam of cold molecules that has seen much use in the field of spectroscopy is the supersonic free jet [45]. A supersonic free jet is formed when gas held in a reservoir at high pressure is allowed to expand through a small aperture into a volume with a lower background pressure. During the expansion the thermal motion of the molecules is converted into forward velocity through interparticle collisions, leading to a cold but fast beam of molecules. These sources have been used extensively in the spectroscopy of metal clusters [46] and molecules [47].

A number of advances and alterations to the supersonic free jet have been made. In 1975 Smalley *et al* found that by seeding molecules into a supersonic jet of monatomic gas lower translational and rotational temperatures could be obtained compared to expanding a purely molecular gas [48]. The monatomic carrier gas reaches a lower temperature during the supersonic expansion than the molecules due to differences in the heat capacity ratio between the two species. It then acts as a refrigerant for the seeded molecules, cooling them to temperatures lower than what would be possible if a pure molecular gas was expanded. In 1979 Liverman *et al* developed a pulsed valve based on a design by Gentry and Giese [49, 50]. With this valve they could generate molecular beam pulses of equal intensity and internal temperature to a continuous source, with a lower average gas load on the pumping system. Since then many other valve designs have been used in the production of supersonic beams, such as valves using piezoelectric materials [51, 52] and solenoid valves based on fuel injectors [53].

Seeding the species of interest into the supersonic expansion led to an increase in the

number of molecules which could be cooled and analysed [54]. Radicals were created in the jet through pulsed photodissociation [55] and metal clusters were created through laser ablation of a rod [56]. The rod was positioned in the gas flow prior to the supersonic expansion so that as the gas expanded at the exit of the channel it cooled both the carrier gas and the metal clusters. A rotating rod is often used in these sources as continual ablation of a single point leads to a reduction in signal from alterations in the surface of the metal. Liquid metal has also been used as an ablation source to reduce this effect. As a liquid surface can self-regenerate on a timescale shorter than the repetition rate of the ablation laser this removes the need for a rotating rod [57].

The method of seeding a supersonic jet through laser ablation was extended in two directions. The first was to improve the thermalisation of the metal clusters with the carrier gas before it expands. This was done by adding a $\sim$1 cm^3 volume before the expansion nozzle where the carrier gas and metal clusters could collide, and the heat generated from the ablation be carried to the walls. This resulted in a colder carrier gas before the expansion and so a slower supersonic beam of metal clusters [58, 59]. Optimum cluster formation occurred when the ablation coincided with the highest helium pressure in the chamber and the helium could act as a buffer gas, reducing the kinetic energy of the plume. The second extension to producing metal clusters from laser ablation was to create metal containing radicals by ablating the metal into a mixture of an inert carrier gas and a reactant. Sources have been developed to create radicals in a continuous supersonic jet [60] and a pulsed jet where the metal is ablated before [61] and after [62] the supersonic expansion.

1.2.2 Buffer gas beams

Another method which has been recently developed for creating beams of atoms or molecules is the buffer gas beam source [63]. This is based on the buffer gas cooling method for trapping molecules described above. Typically a low pressure of buffer gas is flowed continuously through a cryogenically cooled reservoir, or buffer gas cell, with a volume of $\sim$10 cm^3. The molecule of interest is loaded into the cell either through a capillary tube or via laser ablation [64]. The buffer gas reduces the size of the ablation plume [65], reducing the number of molecules lost to the walls, and cools the molecules by transporting heat to the walls. Both helium and neon have been used as buffer gases [66]. Neon has the advantage of freezing out on any surface in a liquid helium cryostat, improving the vacuum

outside the buffer gas cell, but care must be taken that the neon does not freeze inside the gas fill line. Simulations of a 14 K neon buffer gas beam show that it will have a larger number of slow moving molecules than a 4.2 K helium beam which is useful if only the slow tail of the velocity distribution is required [67].

The mean forward velocity of the molecular beam depends on the mass flow of the buffer gas through the cell. If the mass flow is low the molecules diffuse to the aperture, resulting in a slow but weak beam, or if it is high they are swept to the aperture resulting in an intense but fast beam. At very high flows the velocity approaches the velocity expected in a supersonic expansion [68]. This velocity can be reduced by attaching a second cell to the exit of the aperture. The second cell has a large aperture covered in a mesh and slits in the side to allow helium to escape the cell leading to a lower pressure in the second cell than in the first. A high mass flow can then be used to sweep a high percentage of molecules out the first cell and in the second cell helium that is reflected by the mesh reduces the forward velocity of the molecules. Using a mesh also reduces the number of collisions downstream of the aperture by increasing the divergence of the helium beam. These collisions boost the forward velocity of the molecular beam so quickly reducing the number density beyond the second aperture leads to a slower molecular beam. Beams with a velocity as low as $40\,\mathrm{m\,s^{-1}}$ have been reported using this method [69].

1.3 Creating a cold, slow, intense beam

The aim of this thesis is to present ways to improve the precision of the electron electric dipole moment experiment performed at Imperial College London [9] and other experiments requiring slow molecular beams, by creating and slowing a cryogenically cooled beam of polar molecules. It can be shown [70] that the statistical uncertainty of the EDM experiment is inversely proportional to T and $\sqrt{N}$, where T is the interaction time and N is the total number of molecules detected. The uncertainty can then be reduced by decreasing the velocity of the molecules, to increase the interaction time, and by increasing the number density of molecules in the beam. When designing a source, the feasibility of producing a stable beam for a long period of time must also be considered as the EDM experiment is run continuously for long periods of time. In the majority of this thesis YbF is used to form a beam as this is the molecule currently used in the EDM experiment.

Chapters 2 and 3 discuss the creation of cryogenic sources of polar molecules. In

chapter 2 the effect that the helium flow through a buffer gas cell has on the number of molecules extracted is investigated. This is achieved by characterising a buffer gas source of Yb and performing computer simulations of the helium flow. Yb is used for these experiments as it is easier to create and detect than YbF, while having similar physical properties to YbF. As such it is an excellent probe atom for testing the dynamics in buffer gas sources. Chapter 3 details the properties of pulsed molecular beams from cryogenic sources. A solenoid based valve is used to produce a molecular beam and sources with and without a thermalisation chamber are compared. In chapter 4 a travelling wave decelerator is used to reduce the forward velocity of a beam created with a pulsed cryogenic source. The viability of laser cooling YbF is also explored by measuring the Franck-Condon factor of YbF. This is discussed in chapter 5. The suitability of these sources for the current EDM experiment are presented in chapter 6, along with a buffer gas source that has been designed to provide a high flux of molecules at speeds lower than a room temperature source.

Chapter 2

Creating a Beam with Continuous Helium Flow

This chapter describes an experiment where a buffer gas cell is used to produce a beam of cold Yb atoms. The cell is attached to the cold head of a closed-cycle cryocooler which cools the cell to 4 K. Helium is flowed into the cell and out of a small aperture to create a high density buffer gas inside the cell and form a beam which the Yb is entrained into. The Yb is produced in the cell by laser ablation of a solid metal target. It diffuses through the cell and is swept out the aperture by the motion of the helium. The Yb beam is characterised and the effect the helium flow has on the beam is investigated.

2.1 Experiment

The buffer gas cell used for these measurements is shown in figure 2.1. It is a copper cube with an inner length of 30 mm and 10 mm thick walls. Three sides of the buffer gas cell are equipped with windows to allow optical access for probe and ablation lasers. These windows fit loosely into an inset around the hole in the cell. Indium wire is used to fill the rest of the inset and is pressed into the gap by an aluminium cover. The indium bonds with the surrounding material so is able to maintain a vacuum under cryogenic conditions.

On the top of the cell a copper disk is attached using the same method as is used to seal the windows. A slit is made in this copper disk to allow the helium to exit the cell and form a beam. Two slit apertures are used with dimensions of 0.75×4 mm and 1×8 mm referred to, respectively, as the short and long slits. They both have a depth of 1 mm. The choice of aperture allows us to vary the helium number density in the cell for

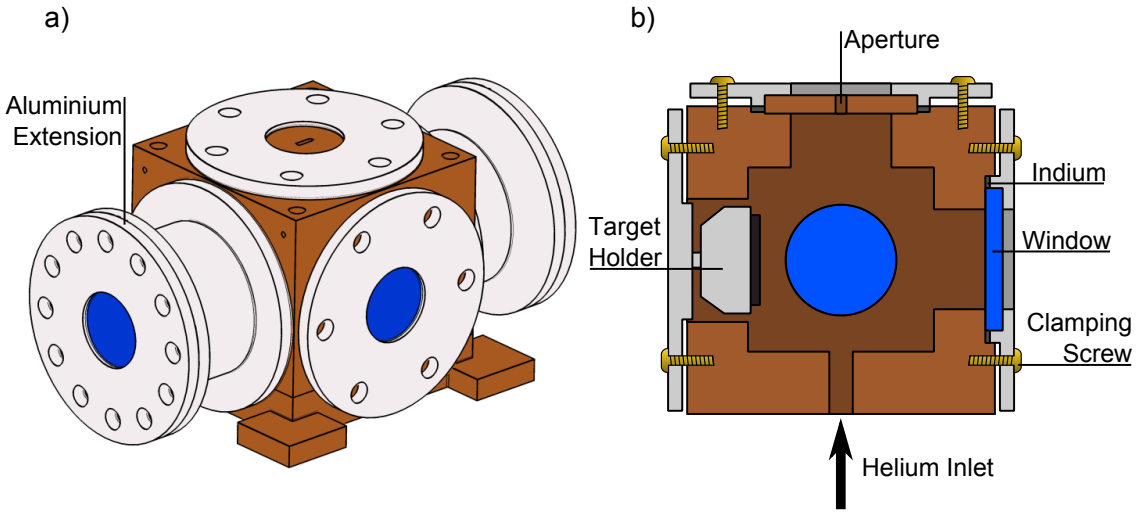

Figure 2.1: a) Isometric and b) cross-sectional view of the buffer gas cell.

the same helium flow through the cell. The helium inlet tube was a 2 mm tube positioned in the centre of the bottom side, opposite the aperture. The helium flow through the cell was regulated with a MKS 1179A mass flow controller.

At the back of the cell a holder for the solid precursor is inserted. It is attached by a grub screw to an aluminum cover. A Spectron Nd:YAG laser is used to ablate the solid metal target. The fundamental wavelength (1064 nm) of the laser is used. The ablation laser is run at a repetition rate of 5 Hz and the pulse width is 7 ns. The power per pulse used is varied between 20 mJ and 140 mJ and the size of the laser on the target is 1.5 mm.

When the target has been ablated many times there can be a significant build-up of ablation material on the windows. This reduces the intensity of the probe laser passing through the cell making absorption measurements less accurate. To prevent this from occurring the two windows used for the probe laser are positioned away from the centre of the cell by 35 mm long aluminium extensions. The same problem does not occur on the window which the ablation laser passes through as the material is ablated off the window with each pulse.

The buffer gas cell is cooled by a SRDK-415D cryocooler from Sumitomo Heavy Industries. This works on a similar principle as a refrigerator, except helium is used as the refrigerant. The helium is compressed in a F-50H compressor unit then fed into the cold head where it expands to cool two stages, the warm plate which provides 35 W of cooling at 50 K and the cold plate which provides 1.5 W of cooling at 4.2 K. To reduce the heat

load on the cold plate a radiation shield is attached to the warm plate to reflect infra-red radiation from the room temperature components. It is made from polished aluminium to minimise the amount of radiation absorbed from the hot side, and emitted on the cold side.

The temperature of the cold plate is measured with a Lakeshore Cernox CX-1050-CH-1.4D thermometer and the warm plate temperature is measured with a homemade temperature sensor calibrated to the commercial thermometer. The typical base temperature of the cold plate is 3.2 K. This rises slightly when helium is flowed through the cell, and when the ablation laser is fired, resulting in a typical temperature of 4 K while the experiment is running. An electrical feedthrough is used to bring the wires required for the thermometers into the vacuum chamber. The wires are 0.13 mm thick to reduce the heat load on the plates.

The cell and cryocooler are contained in a vacuum chamber custom made from ISO250 steel tubing with viewing ports welded on at 90° angles, shown in figure 2.2. KF flanges are used to create a vacuum seal between the various components and the chamber is evacuated using a roughing pump and a turbomolecular pump (Leybold Turbovac 361) positioned at the bottom of the chamber. The speed at which the turbomolecular pump removes helium from the chamber is too low to prevent helium building up outside the aperture so a second pumping scheme must be used to avoid the helium adversely affecting the molecular beam.

To quickly remove helium from the area above the cell a copper cylinder is coated with coconut charcoal and attached to the cold plate. Coconut charcoal is a very good absorber of helium at temperatures lower than 10 K [71] and is bonded to the copper using Stycast 2850FT mixed with 24LV catalyst. A total surface area of 780 cm^2 is covered in charcoal, which gives a pumping speed of 3900 $l\,s^{-1}$. Reflective tape is applied to the outward facing side to further reduce IR radiation reaching the buffer gas cell.

The charcoal can only absorb a certain amount of helium before it becomes saturated. The length of time helium can be flowed through the cell before the charcoal becomes saturated varies with the flow rate used, but is typically a few hours. When the charcoal is saturated the amount of helium in the area outside the cell increases, which increases the thermal contact between the charcoal sorbs and the surrounding warm surfaces. The temperature of the sorbs then increases and more helium is desorbed from the surface. This leads to a rapid increase in the pressure in the chamber, and the temperature of the

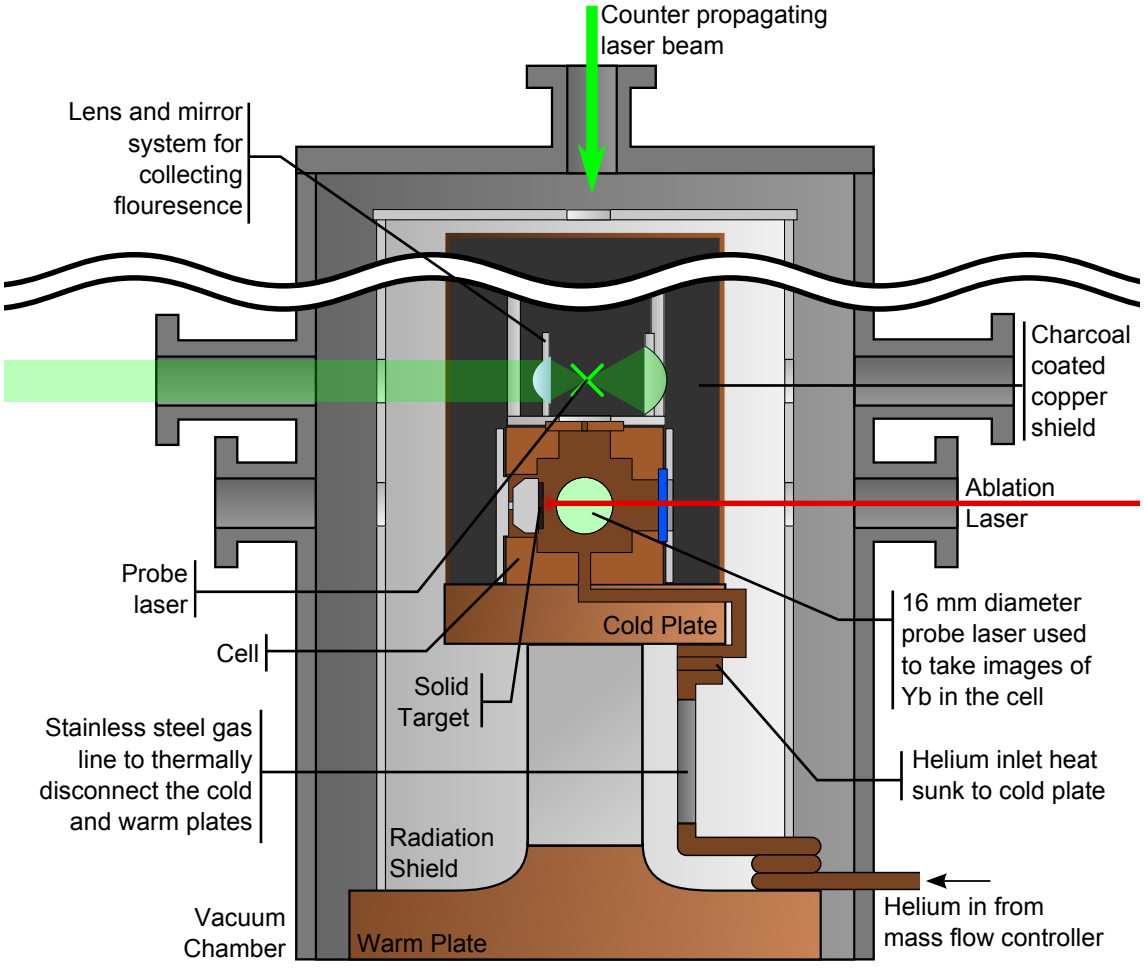

Figure 2.2: A cross-section of the apparatus used in our beam characterisation experiments.

cold plate. The turbomolecuar pump removes the helium from the chamber and after ∼30 minutes the temperature of the cold plate returns to 3.2 K.

Yb and other ablation products are also deposited on the charcoal sorbs. These are not removed when the cold plate is heated so over time the amount of helium the charcoal can absorb before it becomes saturated is reduced. Baking the sorbs at 500 K can remove some of the ablation products but once the sorbs have been used for a few months the capacity of the charcoal is greatly reduced. The charcoal must then be removed from the copper and new charcoal attached to effectively absorb the helium leaving the cell.

Helium is introduced into the cell with a stainless steel gas line which is fed through the vacuum chamber, with the joint sealed by a Swagelok fitting. To ensure the helium was cooled before it reached the cell the stainless steel was connected to a copper pipe and thermally anchored to the warm and cold plates. Between the two plates the gas line is converted back to stainless steel to provide a thermal disconnect between the two temperatures. These joints were welded as it was found the Swagelok fittings between copper and stainless steel leaked at low temperatures due to the different thermal expansion coefficients of the two metals.

2.1.1 Detection Scheme

The layout of the optical components is shown in figure 2.3. The detection laser used is a Menlo Orange One-SHG. This is a commercial amplified fibre laser combined with a periodically poled crystal of lithium niobate to frequency double the light to 556 nm. This excites the Yb atoms on the $^1S_0 \rightarrow {}^3P_1$ transition. A small fraction of the beam is split off to measure the frequency while the main beam is coupled into a fibre and taken to the experiment table. The absolute frequency of the laser is measured with a WS6 High Finesse Wavemeter which is accurate to 600 MHz. Precise measurement of the relative frequency change is taken by recording the transmission through a low finesse Fabry-Perot cavity with a free spectral range of 150 MHz.

Laser induced fluorescence (LIF) is collected at two detection regions installed 23 mm and 132 mm from the aperture, shown in figure 2.4. They both comprise of a spherical mirror with a radius of curvature of 25 mm and an aspheric lens with a back focal length of 10.5 mm. These are positioned so the molecular beam passes through the focal point of the lens and is two focal lengths from the mirror so the fluorescence is collimated when it passes through the windows in the shields. Outside the vacuum chamber there is a second

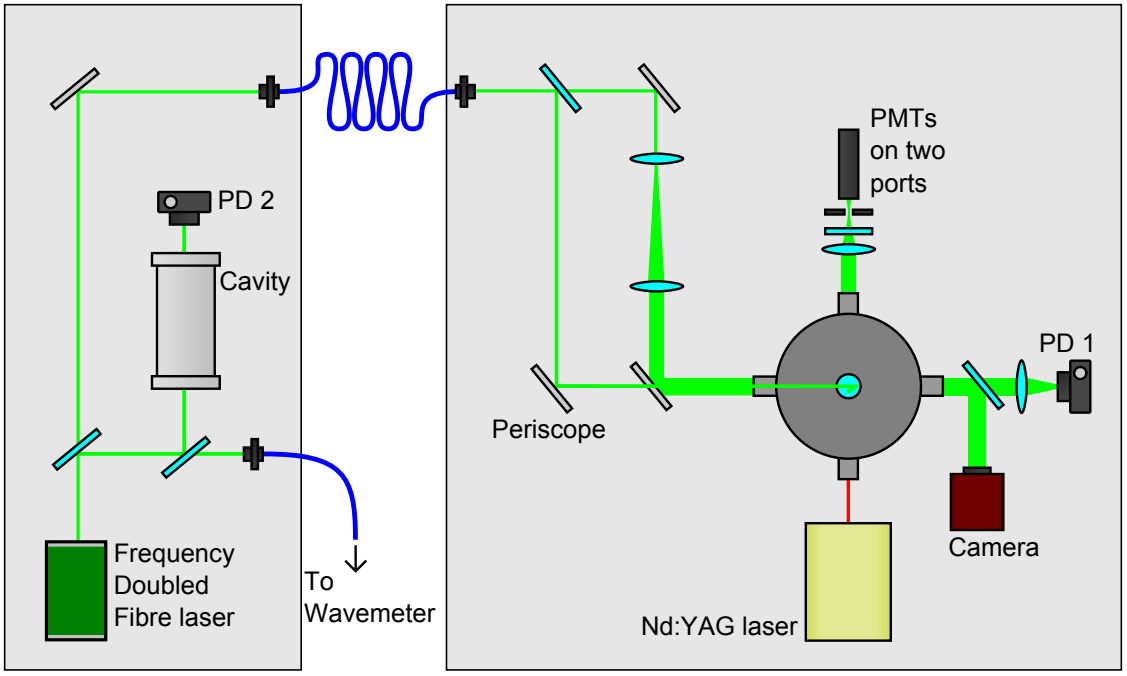

Figure 2.3: Layout of the laser on the optical table.

aspheric lens which focuses the light through an IR filter, a 10 nm wide 550 nm band pass filter and an adjustable iris. The iris is opened to 2 mm to reduce the amount of extraneous light detected. The focussed and filtered fluorescence is collected from the lower detection region by a Hamamatsu R760 photomultiplier tube, and from the upper detection region by a Hamamatsu R2228 photomultiplier tube. The current from the PMTs is collected by a home-made PMT amplifier and converted to a photon count rate using a measured calibration curve.

Absorption images are taken inside the cell by sending a 16 mm diameter laser beam through the cell and then focusing it onto a Marlin F033B camera. The absorption of the beam is used to generate a density plot of the Yb inside the cell. The shutter speed of the camera is 20 µs but the processing of each image requires at least 2 ms so one image is taken per shot. The time between the ablation pulse and the shutter opening is increased every shot so the evolution of the Yb over time can be studied. To remove the effects of power fluctuations in the probe laser and interference in the cell windows, every second image is taken without firing the ablation laser and the difference of the two images taken. The probe laser is also focussed onto a photo-diode to record the temporal change in the fractional absorption for each ablation pulse.

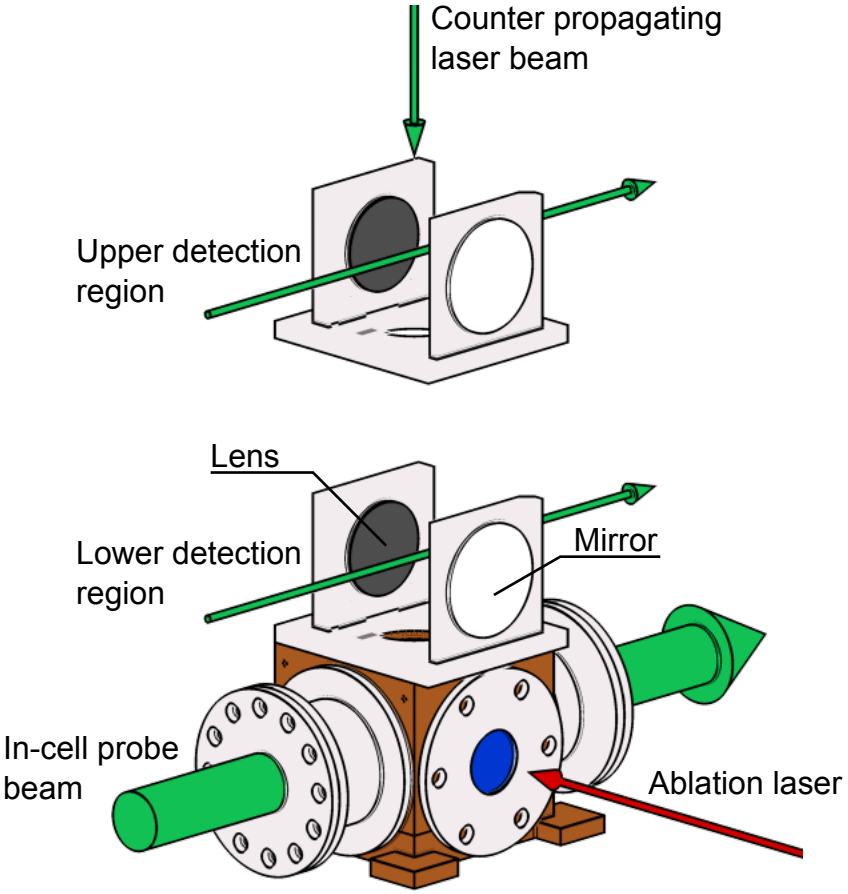

Figure 2.4: Arrangement of the detection regions and probe lasers with respect to the buffer gas cell.

For each ablation shot fired a time-of-flight profile is recorded from each detector for 15 ms with a sample rate of 100 000 points/s. The timing of the ablation laser and the other components of the experiment are controlled by a computer running ScanMaster, a program developed within the group. This program also handles data collection and compression. It is interfaced with the experimental equipment using a digital in/out and a digital-analogue-converter card from National Instruments.

2.2 Theory

Inside a buffer gas cell the particle motion can be approximated using two methods depending on the distance a helium atom travels before it collides with another atom, known as the mean free path. Kinetic theory is used in the low pressure limit when the mean free path is much larger than a characteristic distance. If this characteristic distance is the length of the cell then kinetic theory can be used to predict the properties of the gas in the cell and the helium motion is known as free molecular flow. If the mean free path is larger than the width of the aperture, kinetic theory can be used to predict the properties of the gas as it leaves the cell and the beam is effusive. In the high pressure limit, when the mean free path is much smaller than the length of the cell, the gas can be considered as a continuous fluid and the Navier-Stokes equations used to calculate its properties. The flow through the cell is then hydrodynamic and, if the pressure difference across the aperture is high enough, the beam is supersonic.

The set of equations that should be used to describe the particle motion can be determined by calculating the Knudsen number, Kn, which is inversely proportional to the number of collisions,

$$\mathrm{Kn} = \frac{\lambda}{L} = \frac{1}{\sqrt{2} n_0 \sigma L}, \tag{2.1}$$

where λ is the mean free path, L is the characteristic length, n_0 is the number density in the cell and σ is the scattering cross section of the buffer gas. In the case where $\mathrm{Kn} > 1$ the gas is in the free molecular regime while for $\mathrm{Kn} < 0.01$ it is hydrodynamic. Between these two regimes is a transitional regime where effects from both regimes must be considered. Bounds on the Knudsen number can be found by estimating the number density in the cell for effusive and supersonic flow through the aperture.

2.2.1 Effusive Flow

The number density in the cell is related to the particle flux out of the cell. This can be calculated for an effusive beam by considering the number of buffer gas particles inside the cell that will reach the aperture in a time $\mathrm{d}t$ [72]. The number density, n, of particles that have a speed between v and $v + \mathrm{d}v$ and come from the solid angle $\mathrm{d}\omega$ is

$$n = \frac{\mathrm{d}N}{\mathrm{d}V} = n_0 \frac{\mathrm{d}\omega}{4\pi} f(v)\,\mathrm{d}v, \tag{2.2}$$

where n_0 is the number density of all particles in the cell and $f(v)$ is the distribution of speeds in the cell. Of the particles with this speed and direction, those that reach the aperture in time $\mathrm{d}t$ will be contained in a cylindrical volume whose axis is parallel to the direction of motion of the particles, given by an angle θ relative to the normal of the plane of the aperture. The volume of this cylinder is $\mathrm{d}V = v\cos\theta A\,\mathrm{d}t$ where A is the area of the aperture. The number of atoms contained within this cylinder is,

$$\mathrm{d}N = n_0 \frac{\mathrm{d}\omega}{4\pi} f(v)\,\mathrm{d}v\,\mathrm{d}V = n_0 \frac{\mathrm{d}\omega}{4\pi} f(v) v\cos\theta\, A\,\mathrm{d}t\,\mathrm{d}v. \tag{2.3}$$

The distribution of speeds in the cell is a Maxwell distribution of the form

$$f(v) = \frac{4}{\sqrt{\pi}} \left(\frac{m}{2kT}\right)^{3/2} v^2 \exp\left(\frac{-mv^2}{2kT}\right). \tag{2.4}$$

Inserting this into equation 2.3 and integrating over all speeds and directions, the particle flux through the aperture is,

$$\frac{\mathrm{d}N}{\mathrm{d}t} = \frac{n_0}{4}\sqrt{\frac{8k_BT}{\pi m}}A = \frac{n_0\bar{v}A}{4} \tag{2.5}$$

where A is the area of the aperture and $\bar{v}$ is the average molecular velocity. As the flow of buffer gas into the cell is equal to the flow out this gives us an upper bound for the number density in the cell,

$$n_0 < \frac{4\dot{N}_{\mathrm{in}}}{A\bar{v}}, \tag{2.6}$$

where $\dot{N}_{\mathrm{in}}$ is the particle flow into the cell, which is set by the mass flow controller. This upper bound does not take into account the transmittance of the aperture. When the length of the aperture becomes much larger than the characteristic width of the aperture the transmittance will decrease due to increased collisions with the walls and the number density in the cell will increase. Particles that are travelling faster are more likely to reach the aperture so the most probable velocity in the beam is equal to $\sqrt{3k_{\mathrm{B}}T/m}$ [30].

Using the upper bound for the number density in the cell the Knudsen number can be calculated from equation 2.1. The aperture area is $0.75 \times 4\,\text{mm}$, the length of the cell or the width of the aperture is used for the characteristic length and a helium scattering cross section of $2.6 \times 10^{-19}\,\text{m}^2$ is used [73]. Figure 2.5 shows the Knudsen number across the range of flows we are interested in. The Knudsen number in the aperture is equal to 1 at 1 SCCM so the beam will be effusive at flows below this. At 1 SCCM, and in the case of effusive flow through the aperture, the gas in the cell has a Knudsen number of 0.02 so is in the transition regime. For effusive flow through the aperture the Knudsen number in the cell is equal to 0.01 at a flow of 2.4 SCCM.

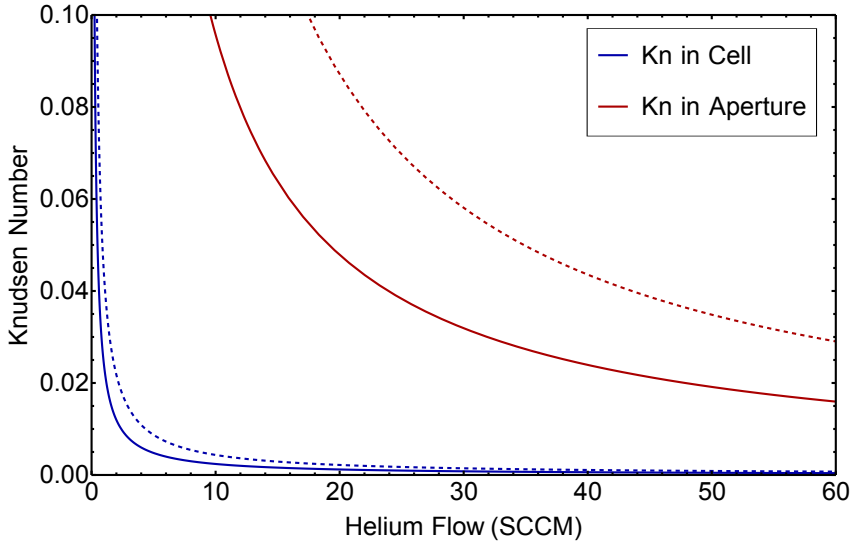

Figure 2.5: Knudsen number in the cell and aperture in the case of effusive flow (solid line) and supersonic flow (dashed line) through the thin aperture.

2.2.2 Supersonic Flow

When the helium is expanding supersonically from the aperture the gas can be considered a continuous fluid and we can apply the continuity equation, $\nabla \cdot (\rho \mathbf{u}) = 0$ [72], where ρ is the density of the gas and $\mathbf{u}$ is the bulk velocity vector. Assuming one dimensional flow the continuity equation can be integrated over the volume inside the aperture

$$\iiint_V \nabla \cdot (\rho \mathbf{u})\, \mathrm{d}V = \oint_S \rho \mathbf{u} \cdot \mathbf{n}\, \mathrm{d}S = \rho_2 u_2 A_2 - \rho_1 u_1 A_1 = 0, \tag{2.7}$$

where A_1 and A_2 are the cross-sectional areas of the flow at two points in the aperture, ρ_1 and ρ_2 are the densities at these points and u_1 and u_2 are the bulk velocities at these

points. By rearranging equation 2.7 it can be seen that the mass flow at the first point is equal to the mass flow at the second, so the mass flow is constant across the aperture and equal to $\rho\, uA$. The particle flow through the aperture is then,

$$\frac{\mathrm{d}N}{\mathrm{d}t} = n_a u_a A, \tag{2.8}$$

where n_a and u_a are, respectively, the number density and bulk velocity in the aperture and A is the area of the aperture.

The number density and bulk velocity in the aperture can be found by considering the stagnation enthalpy of a streamline, h_0, which is defined as,

$$h_0 = \frac{u^2}{2} + h \tag{2.9}$$

where u is the bulk velocity and h is the enthalpy at some position along the streamline. The difference in enthalpy between two points can be expressed as [72]

$$h_1 - h_2 = \int_{T_2}^{T_1} c_\mathrm{P}\, \mathrm{d}T = \int_{T_2}^{T_1} \frac{k_\mathrm{B}}{m} \frac{\gamma}{\gamma - 1}\, \mathrm{d}T, \tag{2.10}$$

where γ is the ratio of the specific heats at constant pressure and constant volume, $c_\mathrm{P}/c_\mathrm{V}$. Combining this with equation 2.9 and assuming an ideal gas the bulk velocity can be expressed in terms of the temperature,

$$u = \sqrt{2\frac{\gamma}{\gamma - 1}\frac{k_\mathrm{B}}{m}(T_0 - T)}. \tag{2.11}$$

Using the isentropic relation between pressure and temperature equation 2.11 can be expressed in terms of pressure,

$$u = \sqrt{\frac{2\gamma}{\gamma - 1}\frac{k_\mathrm{B}T}{m}\left[\left(\frac{P_0}{P}\right)^{(\gamma-1)/\gamma} - 1\right]}. \tag{2.12}$$

An important quantity for supersonic flow is the Mach number, $M = u/a$, where a is the speed of sound,

$$a = \sqrt{\gamma\frac{k_\mathrm{B}T}{m}}. \tag{2.13}$$

Equation 2.12 then becomes,

$$M = \frac{u}{a} = \sqrt{\frac{2}{\gamma - 1}\left[\left(\frac{P_0}{P}\right)^{(\gamma-1)/\gamma} - 1\right]}. \tag{2.14}$$

Once the beam is supersonic the properties can be expressed in terms of the Mach number. Rearranging 2.14 gives an expression for the pressure, and the number density

$$\frac{P}{P_0} = \frac{n}{n_0} = \left(1 + \frac{\gamma - 1}{2}M^2\right)^{-\gamma/(\gamma-1)}. \tag{2.15}$$

Inserting this into equation 2.12 the velocity can also be expressed in terms of the Mach number,

$$u = M\sqrt{\frac{\gamma k_{\mathrm{B}} T_0}{m}}\left(1+\frac{\gamma-1}{2}M^2\right)^{-1/2} \tag{2.16}$$

At the aperture the Mach number is equal to one. Inserting these equations into equation 2.8 and setting $M = 1$ gives the lower bound for number density in the cell,

$$n_0 > \frac{\dot{N}_{\mathrm{in}}}{A}\left(\frac{\gamma k_B T_0}{m}\frac{2}{\gamma+1}\right)^{-1/2}\left(\frac{2}{\gamma+1}\right)^{-\gamma/(\gamma-1)} \tag{2.17}$$

Figure 2.5 shows the expected Knudsen number in the cell in the case of supersonic flow through the aperture. The Knudsen number in the cell is 0.01 at a flow of 4.4 SCCM and 0.01 in the aperture at a flow of 174 SCCM. For the flows used in the experiment, 1 SCCM to 60 SCCM, the flow through the aperture will be in the transitional region between effusive and hydrodynamic flow. For the majority of the flows used the gas in the cell will be in the hydrodynamic regime.

The velocity of a supersonic beam is altered from the velocity in the cell by collisions downstream of the aperture. The maximum velocity that can be achieved is when all the thermal motion of the particles has been converted to forward motion by these collisions. There will then be no more collisions in the beam and the velocity will be constant. This final velocity can be found from 2.11 and the condition that $T << T_0$,

$$u_{\max} = \sqrt{2\frac{k_{\mathrm{B}} T_0}{m}\frac{\gamma}{\gamma-1}} = v_p\sqrt{\frac{\gamma}{\gamma-1}} \tag{2.18}$$

where v_p is the most probable velocity in the cell.

2.2.3 Thermalisation and Extraction

To ensure the Yb beam is as cold as possible it must have fully thermalised with the helium before it leaves the cell. The number of collisions, N, required for the Yb to reach a temperature $T_N = T_b + \delta T_b$, where T_b is the temperature of the helium, is given by [74],

$$N = -\kappa \ln\left(\frac{\delta T_b}{T_0 - T_b}\right), \tag{2.19}$$

where $\kappa = \frac{(M+m)^2}{2Mm}$, M is the mass of Yb, m is the mass of helium and T_0 is the initial temperature of the Yb. To cool Yb from 2000 K to within 5% of the 4 K helium temperature, 208 collisions are required. The farthest distance a Yb atom will have travelled after N collisions is given by,

$$l_N = N\lambda = \frac{N}{\sqrt{2}n_0\sigma} \tag{2.20}$$

where λ is the mean free path. The time taken to travel this distance is

$$t_N = N\lambda\sqrt{\frac{\pi M}{8k_{\mathrm{B}}T}}, \tag{2.21}$$

where M is the mass of a Yb atom. At 10 SCCM the farthest that a Yb molecule can travel before becoming thermalised is 16 mm so all the molecules will be thermalised before they reach the aperture. The time taken to thermalise the molecules at this flow rate is 0.7 ms.

The number of thermalised molecules that leave the cell will depend on the regime inside the cell. When the gas in the cell is in the free molecular regime there is no motion towards the exit of the cell by the helium so the Yb will diffuse uniformly though the cell. The extraction efficiency is then the ratio of the cell area to the aperture area. In our cell this can be calculated to be 0.03% which imposes a lower limit on the intensity of the molecular beam.

As the Yb is diffusing through the cell the timescale for gas to leave the cell is related to the diffusion constant, D. This can be calculated for diffusion from one gas into another using the Chapman-Enskong approximation [75]

$$D = \frac{3}{16}\left(\frac{2\pi k_{\mathrm{B}}T}{\mu}\right)^{1/2}\frac{1}{n_0\bar{\sigma}_{\mathrm{D}}}, \tag{2.22}$$

where $\bar{\sigma}_{\mathrm{D}}$ is the thermally averaged diffusion cross section. A value of $10^{-18}\,\mathrm{m}^2$ is used as typical for this cross section [76]. For the lowest order diffusion mode the time constant, τ_{diff}, for diffusion through a cubic cell of length L is [77]

$$\tau_{\mathrm{diff}} = \frac{L^2}{3\pi^2 D}. \tag{2.23}$$

For our cell this gives us a diffusive time scale of 27 ms to 161 ms for the flows used in the experiment.

If Yb is being swept out the cell by the motion of the helium the theoretical limit for the extraction efficiency is 100%, when all the helium in the cell is travelling towards the aperture faster than the Yb can diffuse through it. In this case the timescale for the Yb to leave the cell is simply the ratio of the number of atoms in the cell to the rate they are leaving the cell,

$$\tau_{\mathrm{adv}} = \frac{n_0 V}{\dot{N}} \tag{2.24}$$

where V is the volume of the cell. Under the condition of supersonic expansion from the aperture the advective time scale is 180 ms. From this model it would seem that the majority of the molecules would diffuse to the walls of the cell as the characteristic time

for diffusion is shorter than the time it takes the helium to sweep the atoms of out the cell. This would lead to a low fraction of molecules leaving the cell, however the real dynamics are more complicated than suggested by this simple model and are explained in the following sections.

The advective extraction efficiency is reduced if the flow through the cell becomes unstable. This occurs if the flow is turbulent rather than laminar, and results in chaotic eddies and vortices appearing. Whether the flow will be laminar or not is determined by the Reynolds number. If the Reynolds number is above a characteristic value of ∼2000 [78] the flow becomes turbulent. The Reynolds number can be expressed in terms of the Mach number and Knudsen number,

$$\mathrm{Re} = \frac{\mathrm{M}}{\mathrm{Kn}}\sqrt{\frac{\gamma\pi}{2}}. \tag{2.25}$$

As the Mach number in the aperture is 1 for supersonic flow an upper limit for the Reynolds number can be calculated to be ∼100 at 60 SCCM. This is well below the characteristic Reynolds number so no turbulent flow is expected near the aperture.

2.3 Model

The flow of helium through our cell was simulated using a finite element modelling program. This method was chosen as it reveals the variation in flow properties across the cell, and the effect this has on the molecular beam produced. The high density of helium in the cell results in continuum conditions which are best solved using the Navier-Stokes equations. The computational fluid dynamics program Star-CCM+ was chosen to model the helium flow as it is based on these equations.

Finite element modelling software splits the simulation area into a mesh, with each mesh cell having uniform properties. During an iteration the effect of each cell on its neighbour is computed and each cell is altered to reflect these changes. Various properties are measured at each iteration to monitor the status of the simulation. For a steady state solution the model has converged once these properties become constant.

The equation of state used for the helium gas was the Peng-Robinson equation of state [79]. The physical properties of the gas to be studied can either be taken from a database present in the program or supplied by the user. As low temperatures are present in our simulation the properties of helium shown in Table 2.1 were used. The Reynolds number

is below the characteristic value so no turbulent effects were taken into account in the simulation.

Property	Value
Acentric Factor	-0.3854[a]
Critical Pressure	2.275 bar[b]
Critical Temperature	5.195 K[c]
Dynamic Viscosity	Interpolated table[d]
Molecular Weight	4.0026 kg/kmol[b]
Specific Heat	5197.61 J/(kg K)[b]
Thermal Conductivity	Interpolated table[e]

Table 2.1: Thermophysical values of helium used in the simulation. Sources are [a] Calculated value, [b] Default value from Star-CCM+, [c] value from NIST, ref [80], [d] values $<$ 5.17 K from ref. [81], values $>$ 5.17 K from NIST ref. [80] [e] ref. [82].

To create the region used by Star-CCM+ the internal volume of the cell was extracted from a 3-D representation. A cylindrical volume with radius 100 mm and height 300 mm was used to create far field boundary conditions. As the cell is cooled to 4 K all the boundaries are set to this temperature. Additionally the pressure at the far field outlet is set to zero and the mass flow at the inlet is varied between 1 SCCM and 60 SCCM for different simulations. The boundary conditions applied to the cell walls are such that the helium pressure remains constant and the velocity is equal to zero (no-slip condition). As the helium gas in the aperture has a high Knudsen number the slip condition is applied so the velocity does not go to zero at the edge of the aperture. Initially the area inside the cell is uniformly filled with gas at a pressure that approximately corresponds to the mass flow used. The system is then iterated to resolve a steady state solution. This is determined to be when the pressure in the centre of the cell changes less than 1×10^{-4} Pa in 1000 iterations.

The evolution of Ytterbium inside the buffer gas cell is modelled by applying a scalar field which represents the atomic number density. The motion is governed by the transport equation,

$$\frac{\partial c}{\partial t} = \nabla \cdot (D \nabla c) - \nabla \cdot (\vec{v} c), \tag{2.26}$$

where c is the value of the number density, $\vec{v}$ is the velocity of the helium and D is the diffusion coefficient. The interaction between the helium and the Yb is split between

the diffusive term and the advective term. As the diffusive term contains equation 2.22 it includes the physical properties of Yb while the advective term only depends on the velocity of the helium. A source term has not been included as we are interested in the evolution of an initial distribution. The value of the number density at the cell walls is set to zero to replicate the condensation of the Yb on the cold copper. An Implicit Unsteady solver, in which each time step is converged through several iterations, was used to model the evolution of the number density with time. One time step was set to be 0.1 ms as this is much smaller then the time-scale for the motion of Yb through the cell via either diffusion or advection.

2.4 Results

2.4.1 Helium Number Density

Figure 2.6a) shows a plane taken through the centre of the cell when the simulation has converged and the flow at the inlet is 20 SCCM. The number density is found to be almost constant in the cell and decreases quickly across the aperture. Figure 2.6b) shows the number density along the centre line for the short and long slits, normalised to the number density inside the cell. The dashed lines show the beginning and end of the aperture. The greatest change in the number density occurs inside the aperture and a few aperture lengths to either side. Within two aperture lengths of the cell exit the number density has been reduced to 10% of its value in the cell. At these distances the number density is low so the gas can no longer be considered a continuous fluid and the Navier-Stokes equations will return non-physical results. The change in number density shown in the figure is similar for the short and long slit, which is expected as their widths are similar. Simulations of gas flow through a slit aperture have also been performed by Sazin *et al.* using the Direct Simulation Monte Carlo method [83]. This technique does not use the Navier-Stokes equations so is valid at low number densities. They observed a similar change in number density along the centre line of an aperture.

A value for the number density in the cell is extracted from a point in the centre of the cell and compared to the analytical bounds calculated from equations 2.6 and 2.17. Figure 2.7a) shows the number density in the cell for the short slit. With this slit the number density in the cell lies close to the limit for effusive flow at 5 SCCM then tends to the supersonic limit with increasing flow. As the long slit is larger than the short slit a lower

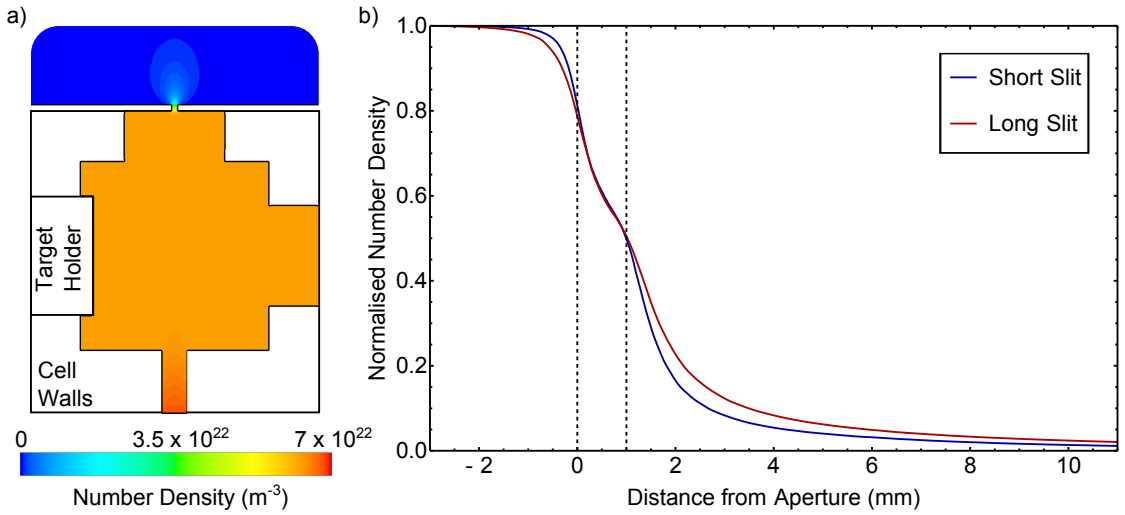

Figure 2.6: Helium number density a) inside the cell and b) as a function of distance along the centre line, for a flow of 20 SCCM. The dashed lines indicate the start and end of the aperture.

pressure is required in the cell to maintain the same flow rate through the aperture. The upper and lower limits on the number density are then smaller than those for the short slit. At low flows the simulated number density is higher than the theoretical maximum. This may be due to the finite depth of the aperture not being taken into account in the theoretical value, or errors in the simulation due to high Knudsen numbers in the aperture. Overall the simulated number density is in good agreement with the theoretical values.

2.4.2 Flow through the cell

Figure 2.8 shows a vector plot of the helium flow through the cell. The arrows show the direction the helium is flowing and the colour indicates the magnitude of the velocity at that point on a log scale. At low flows the majority of the gas in the cell is travelling towards the aperture while at higher flows only the gas in the centre of the cell is travelling towards the aperture, with gas at the outer edges of the cell forming recirculation areas where the gas travels back toward the inlet. As the flow is increased the width of the central column decreases and the recirculation regions fill more of the cell. The flow velocity in this central column increases as the flow increases, so the helium travels through the cell faster at higher flows. The time for helium to travel from the inlet to the outlet along the centre line is 48 ms at 5 SCCM and 4.4 ms at 60 SCCM. This is faster than the expected

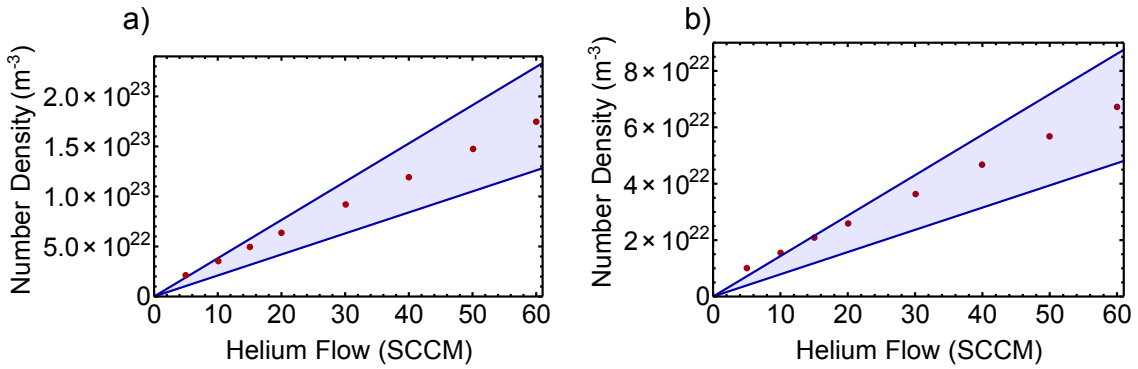

Figure 2.7: The simulated number density of helium in the cell as a function of flow for a) the short slit and b) the long slit. The solid lines are the upper and lower limits to the number density. The upper limit corresponds to effusive flow through the aperture and is calculated from equation 2.6. The lower bound assumes supersonic flow at the aperture and is calculated from equations 2.17. The points are the number densities obtained from the finite element model.

time for helium to leave the cell from equation 2.24 as the volume of helium travelling towards the outlet is smaller than the volume of the cell.

Figure 2.9a) shows how the Yb evolves in the cell over time with a helium flow of 20 SCCM. The experimental images were taken with a CCD camera as described in section 2.1.1. An ablation pulse with an energy of 24 mJ was used to produce Yb which, after 2 ms, appears at the bottom of the window. The flow of helium then sweeps the Yb upwards towards the aperture. At 10 ms an area of lower density appears in the middle of the image which is due to the fact that the helium in the centre of the cell travels faster than the helium at the edges of the cell. After 18 ms the majority of the Yb has been swept out of this region. As the Yb atoms in the recirculation regions are not being swept to the exit they remain there for up to 70 ms. There is always some Yb present in the centre of the image as the probe laser interacts with atoms across the whole cell, and the Yb is only swept out of the centre of the cell. By examining absorption images at other flow rates it can be seen that at lower flows the Yb distribution fills the window. This is due to the fact that the diffusive time-scale is shorter than the advective time-scale, so the Yb diffuses into the flow channel faster then it can be swept out. At higher flows the region of lower density becomes more pronounced as the helium is travelling faster in the flow channel and the Yb takes longer to diffuse out of the recirculation regions.

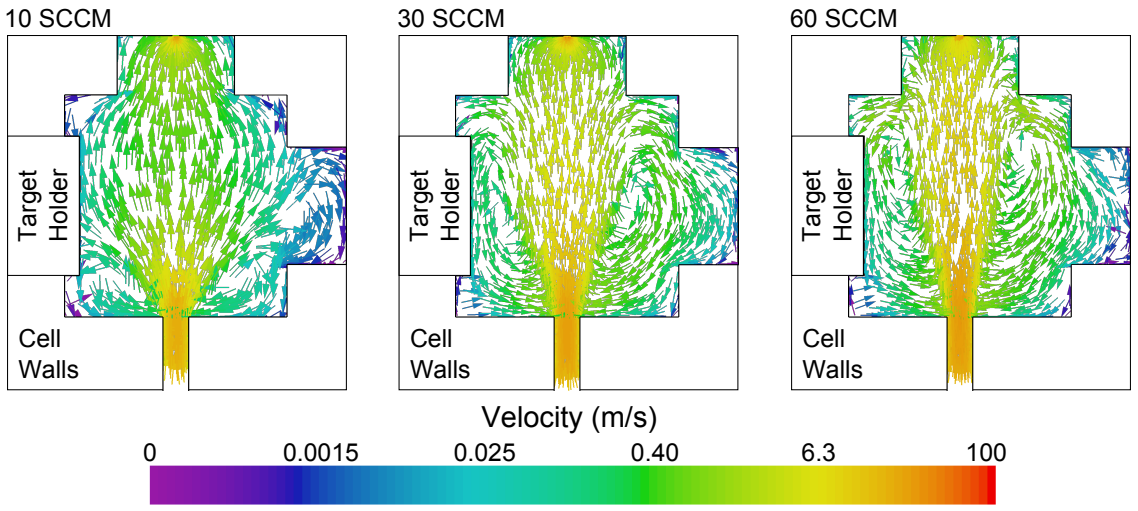

Figure 2.8: Vector plot of helium velocity through the cell. Arrows indicate the direction of the helium bulk velocity and the colour is the magnitude on a log scale.

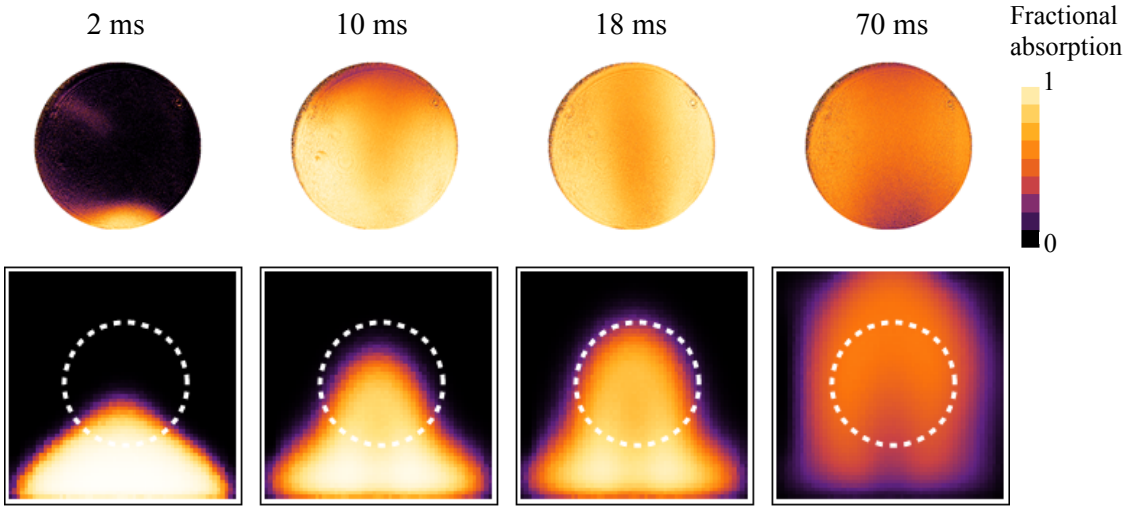

Figure 2.9: Comparison of the experimental (top) and simulated (bottom) Yb distribution in the cell as a function of time after the ablation pulse [84] - Reproduced with permission of the PCCP Owner Societies.

Images from the simulations were created by recording the Yb density across the cell with a 3-D grid of points. The points were summed in one direction to obtain a 2-D image of the number density in the cell. This is converted to fractional absorption to obtain an image which is equivalent to the images produced via absorption through the cell. The initial position of the Yb in figure 2.9 is a sphere of radius 15 mm centred 5 mm below the bottom of the cell and the initial density was chosen so that the degree of absorption approximately matches the experimental images. The simulated images predicts all the main features present in the experiment.

Time-of-Flight Profiles

Figure 2.10 shows a measured and simulated time-of-flight profile for a flow of 30 SCCM. The experimental profile was taken 23 mm above the cell while the simulated profile was recorded in the centre of the aperture. This difference will shift the profile by 500 µs at most. The measured beam intensity consists of a short peak centred at 10 ms and a low amplitude long tail of atoms arriving at later times. The simulated profile shows the same features as the experimental profile apart from the initial increase in the beam intensity. This increase is highly dependent on the position of the initial Yb plume and changes as the ablation laser is moved across the target. As such it is difficult to fully replicate the shape of the profile in the simulation. The shared feature of the profiles is the presence of two decay rates in the beam intensity whose origins will be explained below. An exponential function of the form $A_1\, e^{-x/t_1} + A_2\, e^{-x/t_2}$ was fitted to the profiles and is shown in figure 2.10.

Figure 2.11 shows how the two time constants, t_1 and t_2, change with increasing flow in both the experiment and the simulation. At low flows a single exponential fits to the decay, implying that there is only one process that extracts Yb atoms from the cell. Above 10 SCCM the time constant due to the tail in the profile begins to increase and is of the same order as the expected time for Yb to diffuse through helium. The time constant of the early peak decreases with increasing flow to a value of the same order as the time it takes helium to leave the cell in the central column. The short peak can then be assigned to Yb atoms that thermalise with helium in the central column and are quickly swept out the cell. The longer tail is due to atoms that thermalise in the recirculation regions and must diffuse to the aperture or the central column where they will be swept out the cell. There is good agreement between the time-constants from the measured and simulated

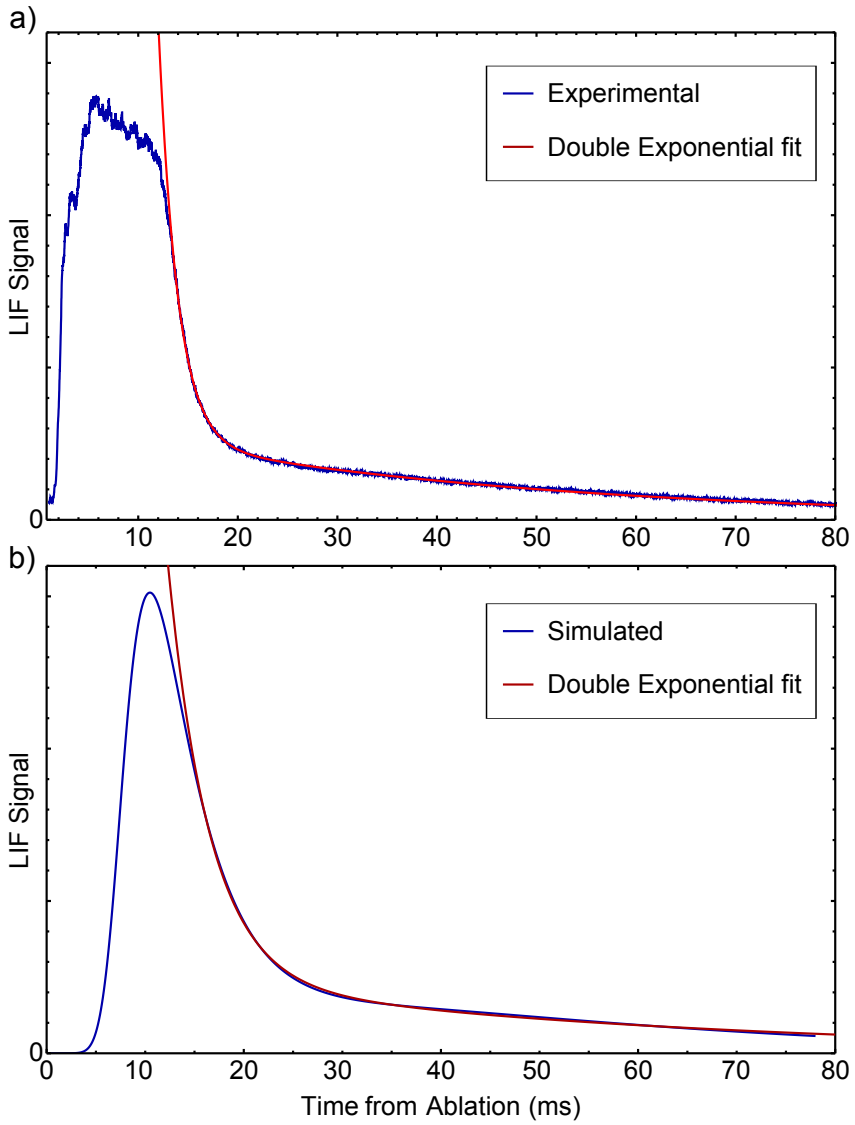

Figure 2.10: a) Experimental time-of-flight profile recorded with a PMT, 23 mm above the aperture and b) simulated time-of-flight profile recorded inside the aperture. There is a flow of 30 SCCM through the cell for both. A double exponential fit to the decay is also shown.

time-of-flight profiles, apart from the long time constant at high flows. At these flows the slow time constant from the measured time-of-flight profile appears to decrease as there is a more complicated shape than a double exponential. A small, broad bump appears, centred near 40 ms. This is probably because the initial distribution of atoms is confined to a smaller region and several diffusion modes play a role.

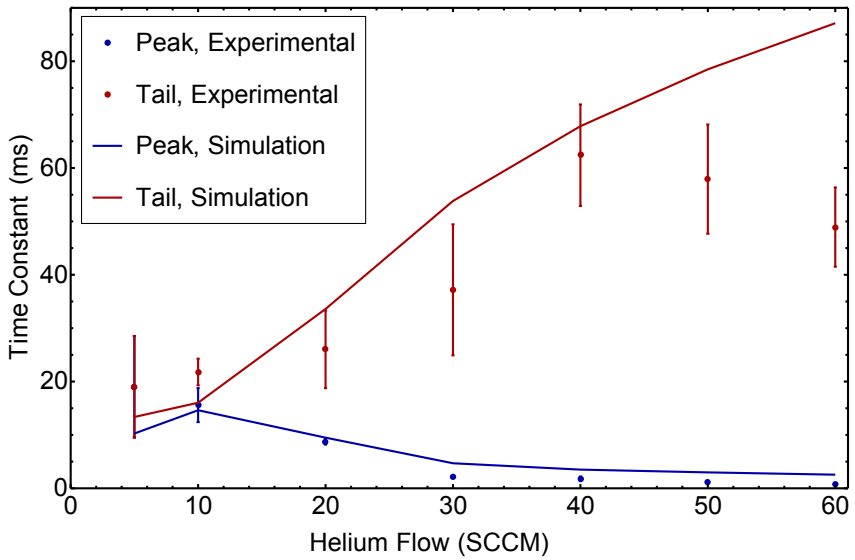

Figure 2.11: Change in the two time constants, t_1 and t_2, with flow. Points are experimental values and the joined lines are results from the simulations. The error bars on the smaller time constants are smaller than the size of the points.

Figure 2.12 shows a time-of-flight profile for the short and long slits. The profile recorded when the long slit was used is shorter as both time constants depend on the number density inside the cell. The slow time constant in the time-of flight profile observed when the long slit is used is 1.9 ± 0.1 times slower than when the short slit is used and the fast time constant is slower by a factor 2.2 ± 0.1. The change in the time constants between the short and long slit are independent of flow. This is expected from equations 2.23 and 2.24 as both scale linearly with number density in the cell.

2.4.3 Temperature in the cell

To measure the temperature of Yb in the cell the frequency of the probe laser is scanned across the $^1S_0 \rightarrow {}^3P_1$ transition at 556 nm. As the laser is scanned the fractional absorption of the probe laser is detected on a photo-diode as described in section 2.1.1. As the

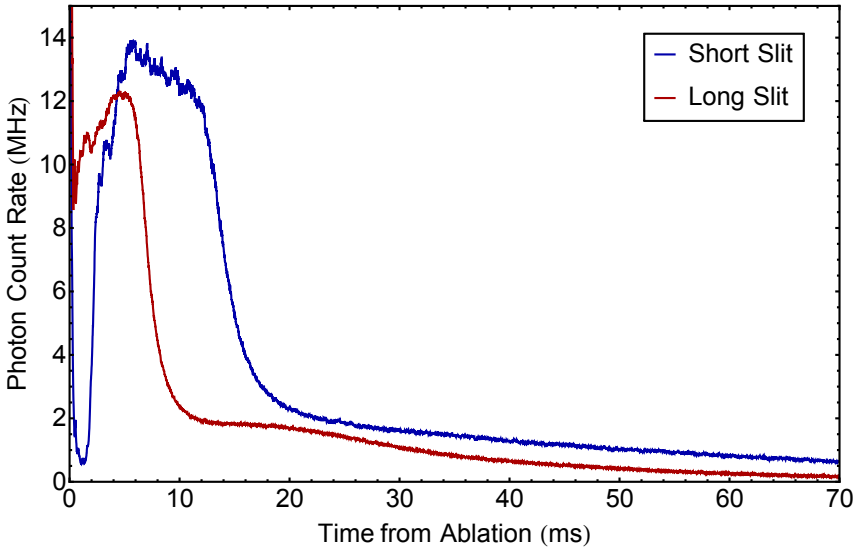

Figure 2.12: Time-of-flight profiles recorded 23 mm above the cell for the short and long slit. There was a helium flow of 30 SCCM through the cell.

probe laser is interacting with the same atoms across the whole time profile, the maximum absorption observed as a function of time is used to generate the absorption spectrum. The logarithm of the absorption is taken to obtain the optical depth as a function of frequency, shown in figure 2.13 and the spectral line is then fitted to a Voigt function,

$$V(\Delta) = \int_{-\infty}^{\infty} \frac{e^{-\Delta'^2/(2\sigma^2)}}{\sigma\sqrt{2\pi}} \times \frac{\gamma/2}{\pi((\Delta-\Delta')^2 + (\gamma/2)^2)}\, \mathrm{d}\Delta', \tag{2.27}$$

where Δ is the detuning between the laser frequency and the central frequency of the transition, σ is the width of the Gaussian component and γ is the full width at half maximum of the Lorentzian component. It is found from the fitted function that the dominant line broadening mechanism is Doppler broadening, with a significant contribution from pressure broadening at high flows. The width of the Gaussian component is used to calculate the temperature of the Yb from the equation

$$T = \left(\frac{\sigma\, c}{f_0}\right)^2 \frac{M}{k_\mathrm{B}}, \tag{2.28}$$

where f_0 is the central frequency of the transition and M is the mass of Yb.

Figure 2.14 shows the change in temperature in the cell as a function of time. An ablation energy of 94 mJ was used to produce the Yb atoms. The temperature of the Yb begins high after it is produced then decreases on a timescale on the order of 10 ms. This is slower than the expected time for the Yb to thermalise with the helium so the Yb temperature can be used as a measure of the helium temperature. A single exponential

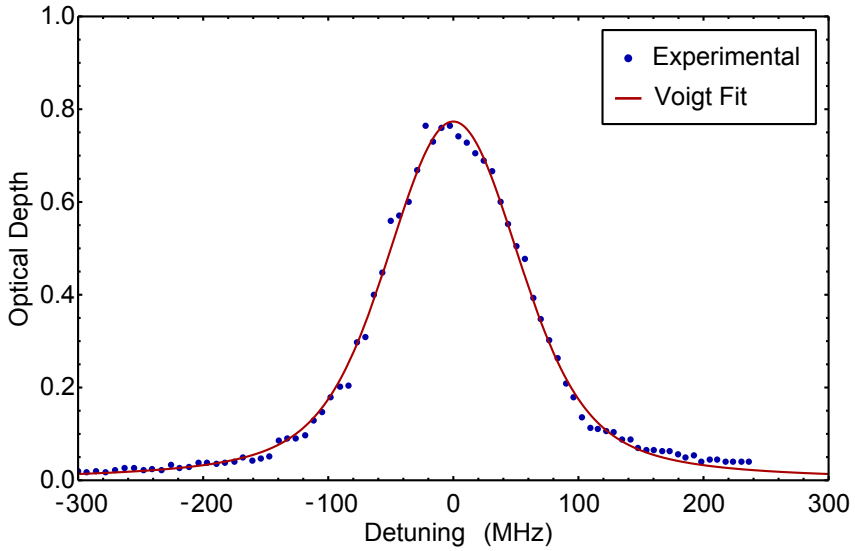

Figure 2.13: Optical depth of Yb in the cell as a function of detuning. The Voigt function fit to the spectral line is also shown. The central frequency of the transition is 539.538 THz [85]

model was fit to the temperature decay of the form

$$T(t) = T_f + (T_i - T_f) \exp\left(-\frac{t}{\tau}\right), \tag{2.29}$$

where T_i is the initial temperature of the helium, T_f is the final temperature of the helium and τ is the timescale for the diffusion of heat through the helium. This model fits well at all values of the helium flow through the cell. The fit to the data is shown in figure 2.14 for two values of the flow. The final temperature is $(4.7 \pm 1.0)\,\mathrm{K}$ independent of flow and the average initial temperature is $(14 \pm 4)\,\mathrm{K}$ with a trend to higher temperatures at higher flows. The uncertainty in these temperatures is the standard error of the results at different flows.

The thermal diffusivity α of a gas is

$$\alpha = \frac{k}{C_p \rho}, \tag{2.30}$$

where k is the thermal conductivity, C_p is the heat capacity at constant pressure and ρ is the density. The thermal diffusion time constant can be found by substituting the thermal diffusivity for the diffusion constant in equation 2.23. Using the values from table 2.1 the heat capacity at constant pressure (specific heat) is $5197.61\,\mathrm{J\,kg^{-1}\,K^{-1}}$ and the thermal conductivity at 4.7 K is $9.00 \times 10^{-3}\,\mathrm{W\,m^{-1}\,K^{-1}}$. The density was calculated

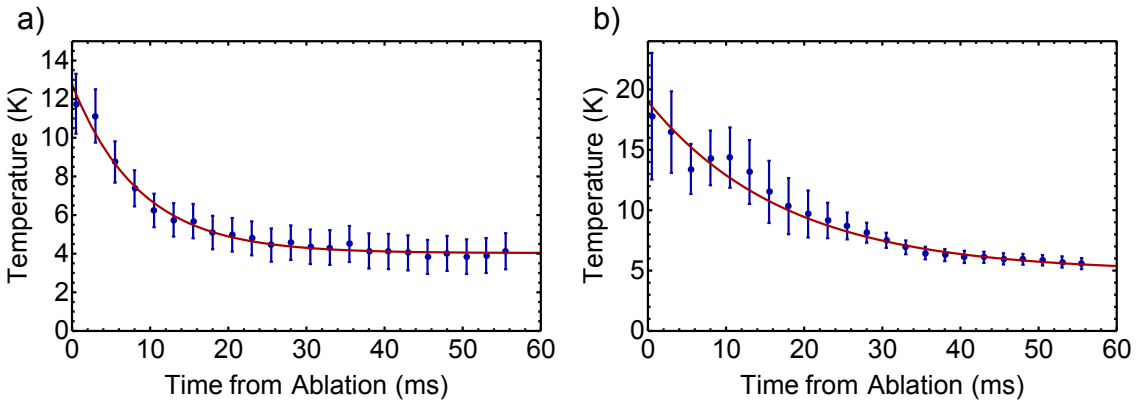

Figure 2.14: Temperature of atoms inside the cell as a function of time after ablation for flows of a) 20 SCCM and b) 60 SCCM. The solid lines are fits to a single exponential model. The error bars are obtained from the Voigt fits to the spectra and appear non-statistical because the data points are correlated.

from the number density obtained from the simulated results. The thermal diffusion time calculated using equation 2.30 is shown in figure 2.15, along with the measured values of τ. The model fits our measurements well and supports the theory that the change in temperature with time is due to the helium thermalising with the walls, rather than the Yb thermalising with the helium.

The widths of the Lorentzian components of the Voigt fits lie in the range of 6 MHz to 22 MHz. They do not show any dependence on time. These widths are much greater than the natural width of the transition so are most likely entirely due to pressure broadening. The pressure broadening cross-section for the 556 nm Yb transition can be found with the equation

$$\sigma_b = \frac{\gamma}{n_{\mathrm{He}}\bar{v}}, \tag{2.31}$$

where γ is the full width at half maximum of the Lorentzian component, in units of angular frequency. Using the same values for n_{He} as used before and a mean thermal velocity of $158\,\mathrm{m\,s^{-1}}$ for helium at 4.7 K a pressure broadening cross section of $(1170 \pm 50) \times 10^{-20}\,\mathrm{m^2}$ is found. This value is independent of flow. The pressure broadening cross-section of this transition was previously investigated in a helium buffer gas of 700 K [86]. Their results give a cross-section of $(197 \pm 5) \times 10^{-20}\,\mathrm{m^2}$ at 700 K. An increasing cross-section with decreasing temperature has been observed in other pressure broadening measurements done at low temperatures [87].

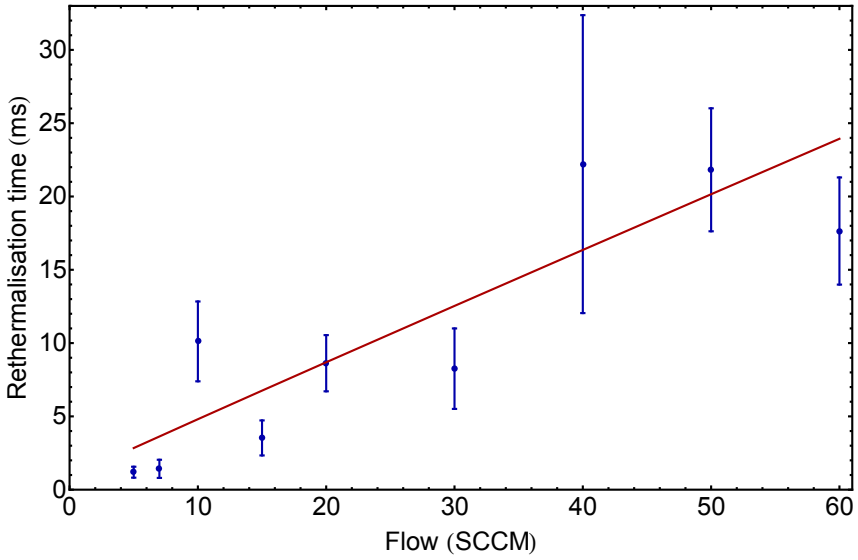

Figure 2.15: Time constant for rethermalisation of the helium following laser ablation. The line shows the time constant for the lowest-order heat diffusion mode in a cubic cell of helium.

2.4.4 Translational temperature of the beam

To measure the longitudinal translational temperature of the beam the spectrum induced by the counter-propagating laser beam is obtained from laser induced fluorescence at the lower detector, as described in section 2.1.1. Doppler broadening is the dominant line broadening mechanism in the beam so a Gaussian function is fitted to the spectral line. The width of the Gaussian is used in equation 2.28 to calculate the longitudinal temperature of the beam.

Figure 2.16 shows the longitudinal temperature as a function of flow for the two slits, averaged over the whole pulse. A pulse energy of 134 mJ was used to ablate the Yb target. At low flows the gas diffuses quickly out the cell on the order of 10 ms and, as the helium in the cell has not fully thermalised with the walls in this time, the temperature of the beam is observed to be larger than the cell temperature. Above 10 SCCM the temperature of the beam is independent of flow with a weighted mean of (2.4 ± 0.3) K for the short slit and (3.2 ± 0.4) K for the long slit. The temperatures in the beam are lower than in the cell, showing that there is some cooling during the expansion from the slit. This effect has been observed in other buffer gas experiments [68, 66].

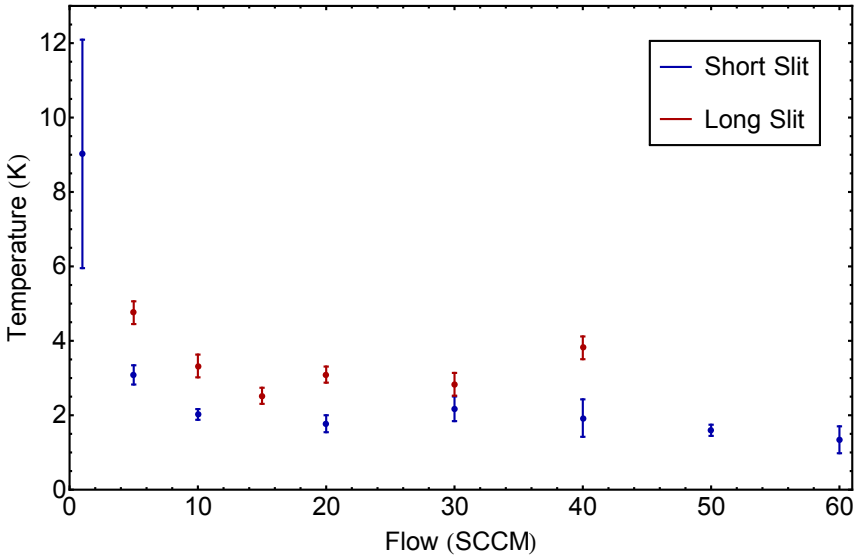

Figure 2.16: Temperature of the atomic beam as a function of flow for the short and long slits.

2.4.5 Velocity

The forward velocity of the beam is obtained by recording spectra simultaneously from the perpendicular and counter-propagating probe lasers at the lower detection region, as described in section 2.1.1. The spectra from the counter-propagating laser is Doppler shifted such that a spectral line has a central frequency of

$$f = \left(1 - \frac{v}{c}\right) f_0, \tag{2.32}$$

where f_0 is the central frequency of the spectral line observed with the perpendicular probe laser, and v is the forward velocity of the Yb atoms. This velocity can be compared to the bulk velocity obtained from the simulation. Before presenting the results we need to consider how the velocity is obtained from the model.

The transport equation used by the finite element model assumes that the bulk velocity of the Yb is the same as the helium at each point in the simulation. It is therefore only possible to extract the bulk velocity of the helium from the model. Figure 2.17 shows the magnitude of the helium velocity both in the cell and along the central axis. Downstream of the aperture the velocity increases to a maximum value then begins to decrease. The distance from the aperture at which the velocity begins to decrease corresponds to the distance at which the Navier-Stokes equations begin to return non-physical results. There will be few collisions beyond this distance and the velocity will not change significantly. The maximum velocity can therefore be taken to be the final velocity of the beam.

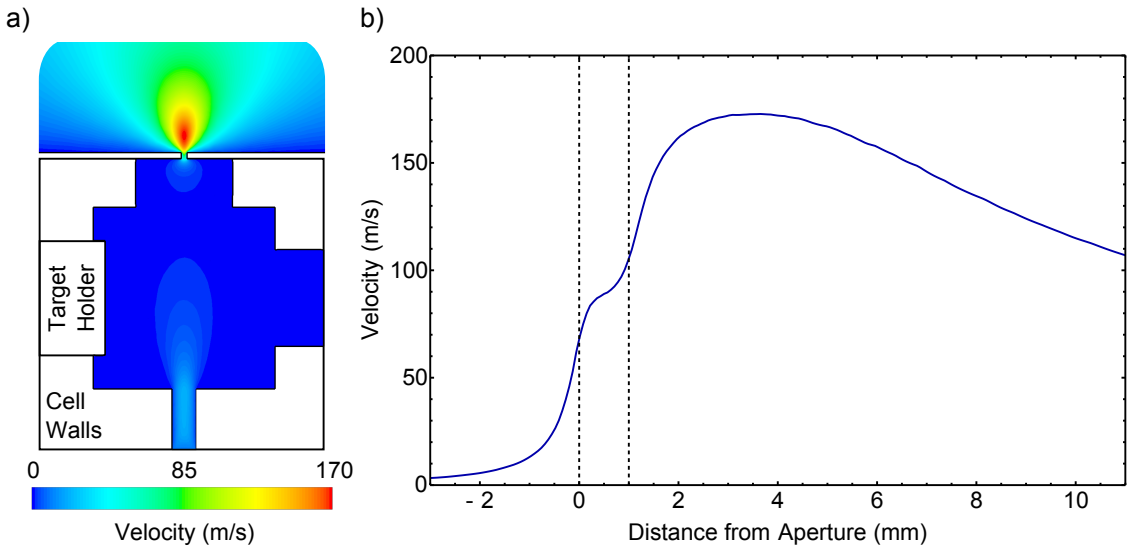

Figure 2.17: Velocity of Yb a) in the cell and b) as a function of distance from the aperture for a flow of 20 SCCM. The dashed lines are the beginning and end of the aperture.

Figure 2.18 plots the maximum velocity from the simulation along with the Yb velocity measured from the experiment for the short and long slit. The whole pulse is used to calculate the velocity. Pulse energies of 134 mJ were used to ablate the Yb target. The uncertainty in the velocity measurements are due to the low-finesse optical cavity used to measure the relative frequency. This error is independent of the pressure in the cell so the standard deviation can be calculated by combining the measurements taken at different flow rates. The number of measurements taken at each flow rate was then used to calculate a standard error.

There is good agreement between the simulated and measured velocities indicating there is very little velocity slip between the Yb and helium in the beam for both slits. The dashed lines in the plot are the supersonic and effusive velocities of helium, and the effusive velocity of Yb at 4 K. At high flows the measured velocity tends to the supersonic velocity of helium, while at low flows it tends towards the thermal velocity of Yb. This is expected as the Yb beam becomes more effusive as the helium flow is lowered. At low flows the simulated velocity drops below the thermal velocity of helium. This is due to the fact that the Navier-Stokes equations calculate the bulk velocity of the helium which is unaffected by the thermal velocity. The velocity of the Yb beam is slightly higher than the simulations at low flows as the Yb has a thermal component of velocity which must be added to the bulk velocity. The flows used in the experiment are not low enough for

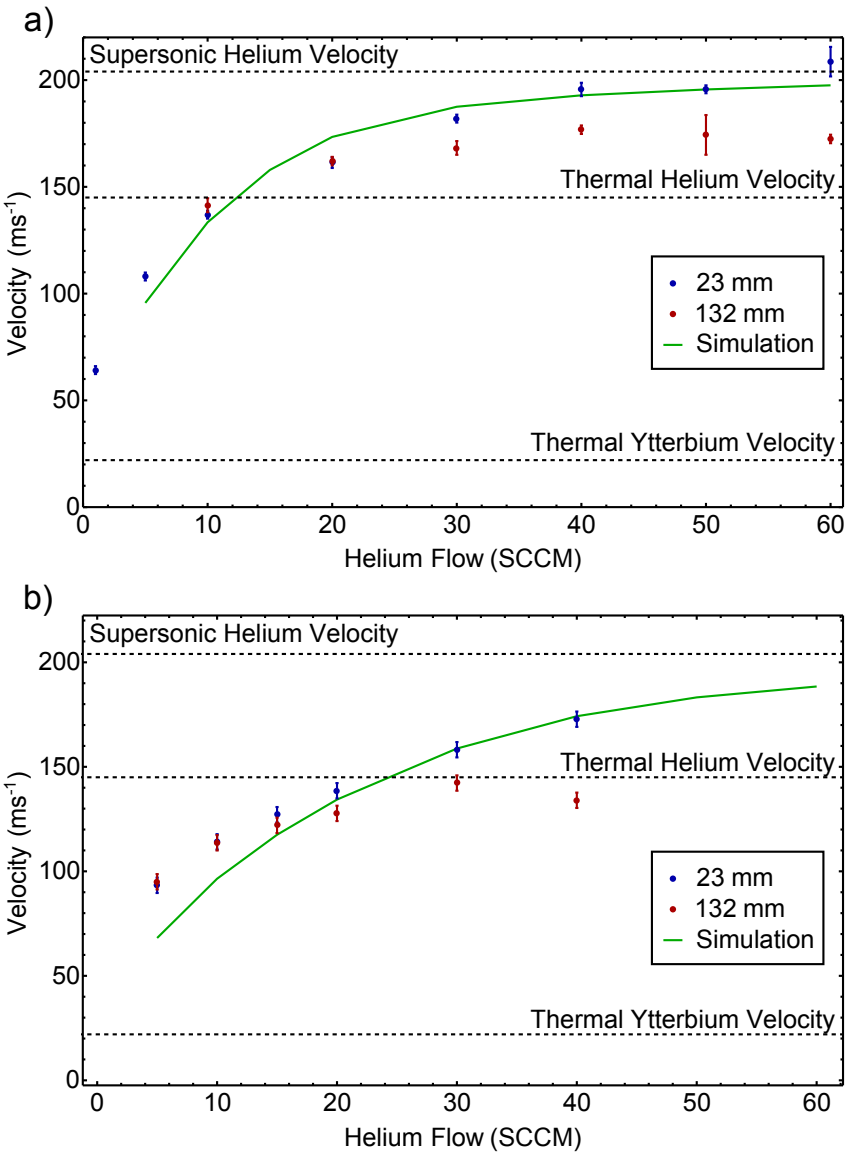

Figure 2.18: Velocity of the atomic beam at various flows for a) the short slit and b) the long slit. Results for the detection regions 23 mm and 132 mm from the aperture are shown. The solid line is the simulated beam velocity.

the final velocity of the beam to be limited by the Yb thermal velocity so the bulk helium velocity is a good prediction of the velocity of the Yb beam. The velocity of the Yb beam when using the long slit is lower than when the short slit is used in both the experiment and simulation. This is a consequence of the lower number density in the cell as the helium in the aperture will experience fewer collisions and so have a slower velocity.

Figure 2.18 also shows the velocity as measured 132 mm from the aperture. At high flows the velocity measured at this detector is lower than the velocity measured at the detector 23 mm above the aperture. This is due to an increased helium number density outside the cell at high flows which causes the mean free path of the helium to become smaller than the distance between the two detectors. The Yb atoms then experience increased collisions as they approach the second detector and the velocity of the beam is decreased. The intensity of the beam at the top detector is also decreased, by 36% at 40 SCCM, and the temperature of the beam is increased, to 12 K at 40 SCCM. These effects could be negated by increasing the helium pumping between the first and second detectors. Decreasing the velocity of a buffer gas beam via increased collisions beyond the aperture has been investigated by Lu *et al.* in [69].

By integrating over a short interval in the time of flight profile the change of velocity with time can be found. A gate length of 50 µs was used to obtain the velocity as a function of arrival time. Figure 2.19 shows the change in velocity with time for 10 SCCM, 30 SCCM and 60 SCCM when using the short slit. The solid line is a fit to the exponential function $v_f + \Delta v \exp(-t/\tau)$ where v_f is the final velocity of the molecular beam, Δv is the difference between the initial velocity and the final velocity and τ is a time constant. The time constant for the short slit ranges from 2.5 ms at 5 SCCM to 5 ms at 60 SCCM. These results are consistent with the observation that the He and Yb cool together through thermalisation with the cell walls, however the time constants are smaller than the time constants for the temperature in the cell. This may be due to the fact that the velocity of the beam is due to the temperature of the helium near the aperture. This helium is close to a cold copper surface so will cool faster than the helium in the centre of the cell where the temperature of the cell is measured.

2.4.6 Divergence

The divergence of the molecular beam, $\Delta\theta$, can be expressed as

$$\Delta\theta = 2\tan^{-1}(\Delta v_{\mathrm{FWHM}}/(2v_f)), \tag{2.33}$$

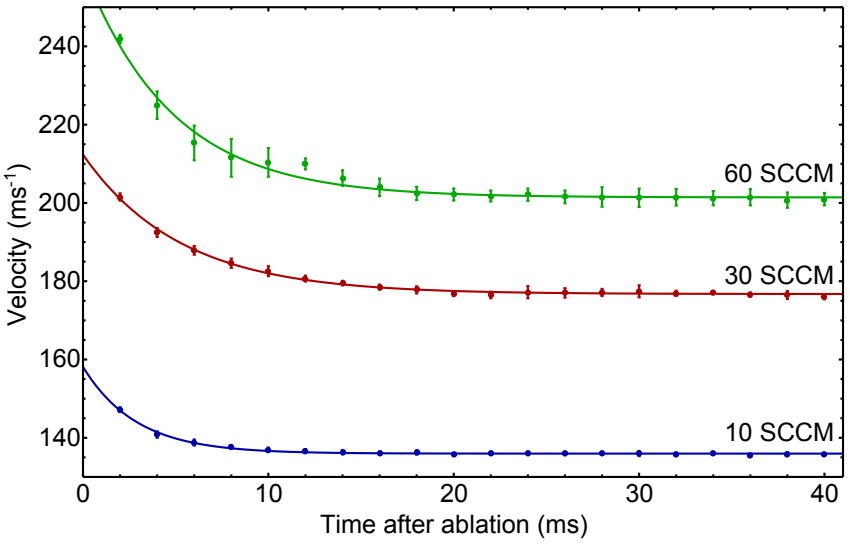

Figure 2.19: Change in the velocity of the atomic beam with time for the short slit, at 10 SCCM, 30 SCCM and 60 SCCM.

where Δv_{FWHM} is the full width at half maximum of the transverse velocity and v_f is the velocity in the forward direction. To obtain the divergence of the molecular beam the transverse velocity was measured from the Doppler width of absorption profiles taken 23 mm above the cell, with the probe laser parallel to the long edge of the aperture.

The divergence of the beam depends on the number of collisions that occur in and around the aperture. When the flow through the aperture is hydrodynamic the helium close to the aperture will be highly collimated so collisions here will decrease the divergence. If the helium flow is increased the number density, and the number of collisions, downstream of the aperture will increase. These collisions will broaden the transverse spread of the beam, and so increase the divergence. When the flow is decreased the beam becomes effusive and the molecules will experience fewer collisions overall, leading to a larger divergence in the beam.

The minimum divergence can be estimated by assuming the Yb atoms are fully entrained from collisions in the aperture and experience no collisions further downstream. The Yb would then be travelling at the supersonic velocity of the helium with the transverse temperature remaining the same as in the cell. The forward velocity in this case is given by equation 2.18 while the velocity width is

$$\Delta v_{\mathrm{FWHM}} = \sqrt{8\ln(2)\frac{k_{\mathrm{B}}T}{m_{\mathrm{Yb}}}}. \tag{2.34}$$

Using the small angle approximation the minimum divergence is then

$$\Delta\theta_{\min} = \sqrt{\frac{8\ln(2)}{5}\frac{m_{\mathrm{He}}}{m_{\mathrm{Yb}}}}, \tag{2.35}$$

which is equal to 9 degrees.

Figure 2.20 shows the divergence of our beam for the different slits. The change in the divergence with flow is similar for the short and long slit. At low flows the Yb experiences few collisions in the aperture so the divergence is high. As the flow increases and there are more collisions in the aperture the divergence quickly decreases to a minimum of 12°, which is close to the above estimate of the minimum divergence. As the flow increases beyond 60 SCCM it is presumed that the increasing number of collisions far from the aperture will increase the divergence, however we have not used flows high enough to observe this effect.

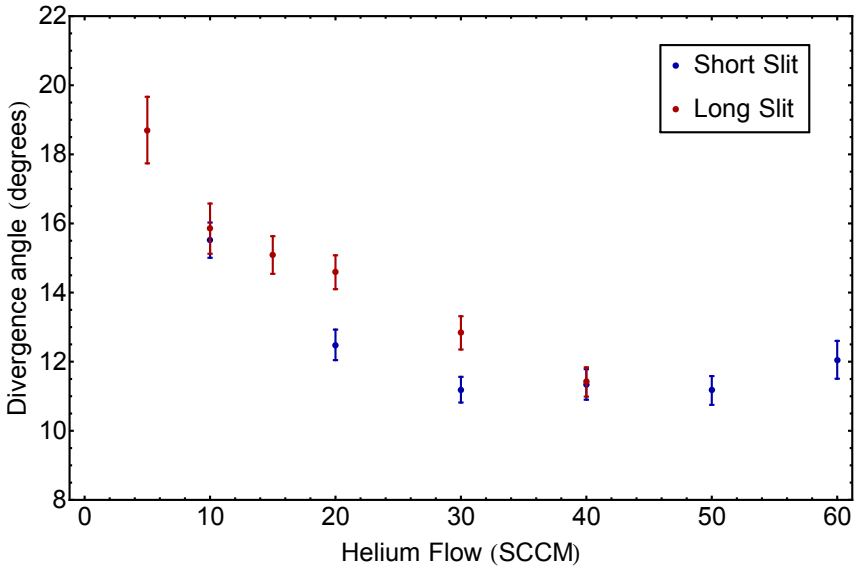

Figure 2.20: Divergence angle, $\Delta\theta$, as a function of flow for the short and long slits.

2.4.7 Extraction Efficiency

In this section we determine the efficiency of extracting Yb out of the cell by simultaneously measuring the fractional absorption in the cell and the fluorescence in the beam with an ablation power of 94 mJ. The fractional absorption of Yb atoms in the cell is measured using the methods described in section 2.1.1. The probe laser is scanned across the ${}^1S_0 \rightarrow {}^3P_1$ transition and the maximum fractional absorption for each ablation plume

used to produce a spectrum. A Voigt profile is fit to the spectral line and the fractional absorption on resonance taken from this fit. This value is converted to a number density by considering the rate equations for a two level system [76]. The Doppler broadening, pressure broadening and saturation of the atomic transition are all taken into account for this calculation. The volume of the probe laser inside the cell is $6.0 \times 10^{-6}\,\mathrm{m}^3$ so an upper estimate on the total number of Yb in the cell is made by assuming all the Yb is located in this volume. A lower limit on the total atom number is set by assuming that the Yb uniformly fills the cell.

To convert the number of photons detected by the PMT to a number of photons scattered by the atoms in the beam the detection efficiency of the PMT must be determined. This is done by simultaneously recording the absorption in the beam and the fluorescence detected by the PMT then comparing the photon scattering rates between the two. As the absolute photon scattering rate can be determined from the fractional absorption the detection efficiency of the PMT, ε, is given by

$$\varepsilon = \frac{V_\mathrm{a} R_\mathrm{f}}{V_\mathrm{f} R_\mathrm{a}}, \tag{2.36}$$

where V_a and V_f are the detection regions of the absorption and fluorescence measurements, R_a is the absolute photon scattering rate and R_f is the photon rate detected at the PMT. The detection efficiency of the PMT is then used to convert the measured scattering rate in the beam to an absolute scattering rate. By taking into account the number of photons scattered by each atom, and integrating over the whole pulse, the number of atoms per steradian per pulse can be found. The divergence angles measured in section 2.4.6 are then used to obtain the total number of atoms that leave the cell.

The simulated extraction efficiency was also calculated. It was assumed that if the Yb reached the aperture it would leave the cell. The value of the scalar field which represents the Yb number density was recorded across a plane in the centre of the aperture for each time step. The number density was assumed to vary linearly between each time step so the total atom number can be found by calculating the volume of the atoms which pass through the aperture between each time step. This is given by $uA\delta t$ where δt is the time step. The total number of atoms in the cell at the beginning of the simulation can be found by multiplying the number density in each mesh cell by the volume of each mesh cell. As the initial number of molecules and the number of molecules which leave the cell are known the extraction efficiency can be calculated. This was done for various plume positions.

The upper and lower limits of the experimental extraction efficiency are shown in figure 2.21a) as a function of flow through the cell. At low flows the plume will fill most of the cell so the extraction efficiency is expected to follow the lower curve. As the flow increases the size of the plume will decrease and the upper curve will be a better indication of the extraction efficiency. Applying this to the data shows that, for this cell geometry, the extraction efficiency is close to 1% at flows less than 10 SCCM then increases to almost 10% at 60 SCCM. There is also a slight decrease in the range of 10 SCCM to 30 SCCM. This trend is replicated by the simulated extraction efficiency of a 5 mm radius sphere offset from the centre of the cell by 8 mm towards the aperture, shown in figure 2.21b). The simulated extraction efficiency is slightly higher than the experimental extraction efficiency which can be attributed to differences in the initial distribution of the ablation plume. The effect the initial position has on the extraction efficiency can be found by simulating the same sphere in the centre of the cell and in the bottom corner of the cell. At 60 SCCM the extraction efficiency is 40% for the sphere in the centre of the cell and 0.7% for the sphere in the far corner. The initial distribution used to produce figure 2.21b) was chosen as it is similar to the ablation plume observed with a closed cell [76].

Figure 2.22 shows the simulated motion of Yb atoms inside the cell for three flows. Below ∼10 SCCM the central column of helium that travels towards the aperture fills most of the cell. As the diffusion time is fast the Yb plume quickly fills the cell and the overlap with the initial plume is large. At low flows most of the Yb is lost to the walls but as the diffusion time increases more Yb is swept to the aperture and the extraction efficiency increases. Between 10 SCCM and 30 SCCM the size of the central column and the Yb plume decreases so the overlap between the two decreases. More Yb is then trapped in the recirculation areas where it diffuses to the walls faster than it is swept out the cell. Above 30 SCCM the helium velocity is the dominant process for the motion of Yb atoms through the cell so less Yb is lost through diffusion to the walls. The majority of the Yb atoms remain in the recirculation region and the increase in the extraction efficiency comes from the tail of the time-of-flight profile. The images show that the atoms that are born in the recirculation regions are less likely to reach the aperture. The maximum extraction efficiency can then be obtained by ensuring there is a large overlap between the initial plume and a region where the helium travels to the aperture faster than the diffusion time to the walls.

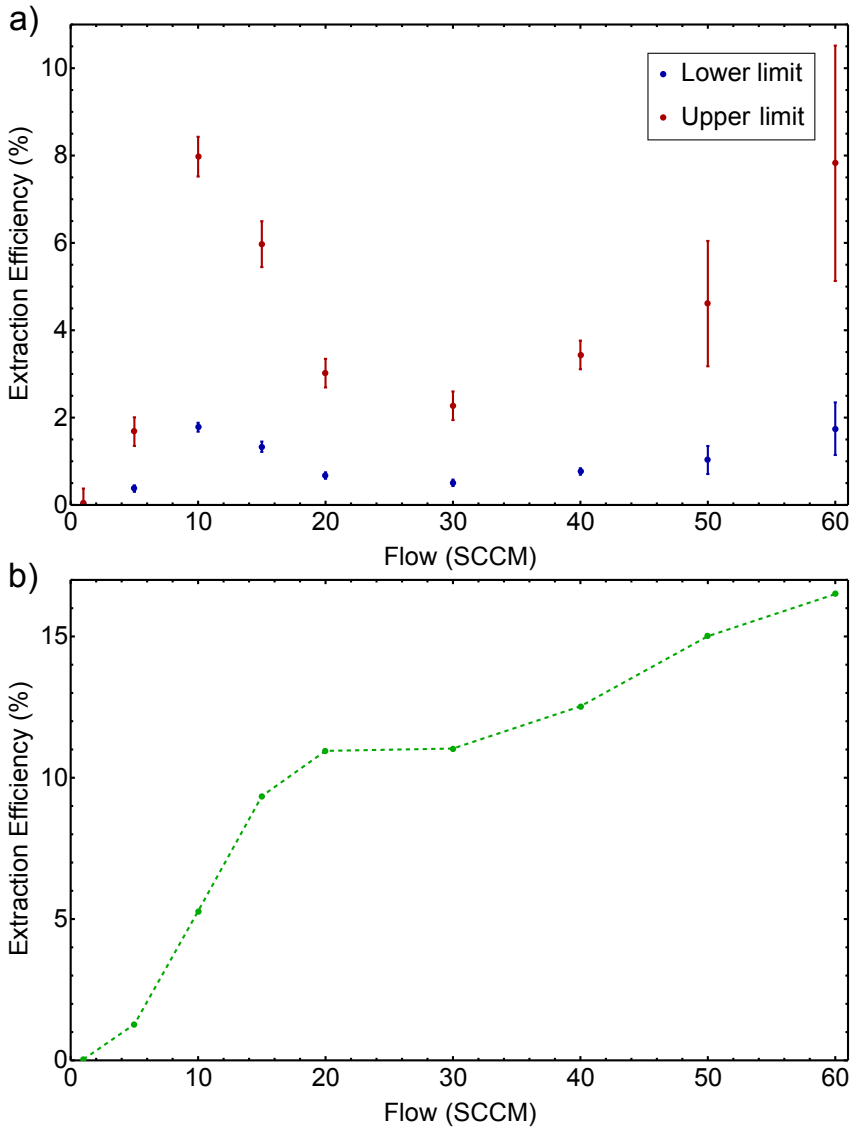

Figure 2.21: a) Upper and lower limits for the experimental extraction efficiency and b) simulated extraction efficiency. The lower limit assumes a uniform distribution of Yb atoms throughout the cell. The upper limit assumes the atoms are confined to the region of the probe laser.

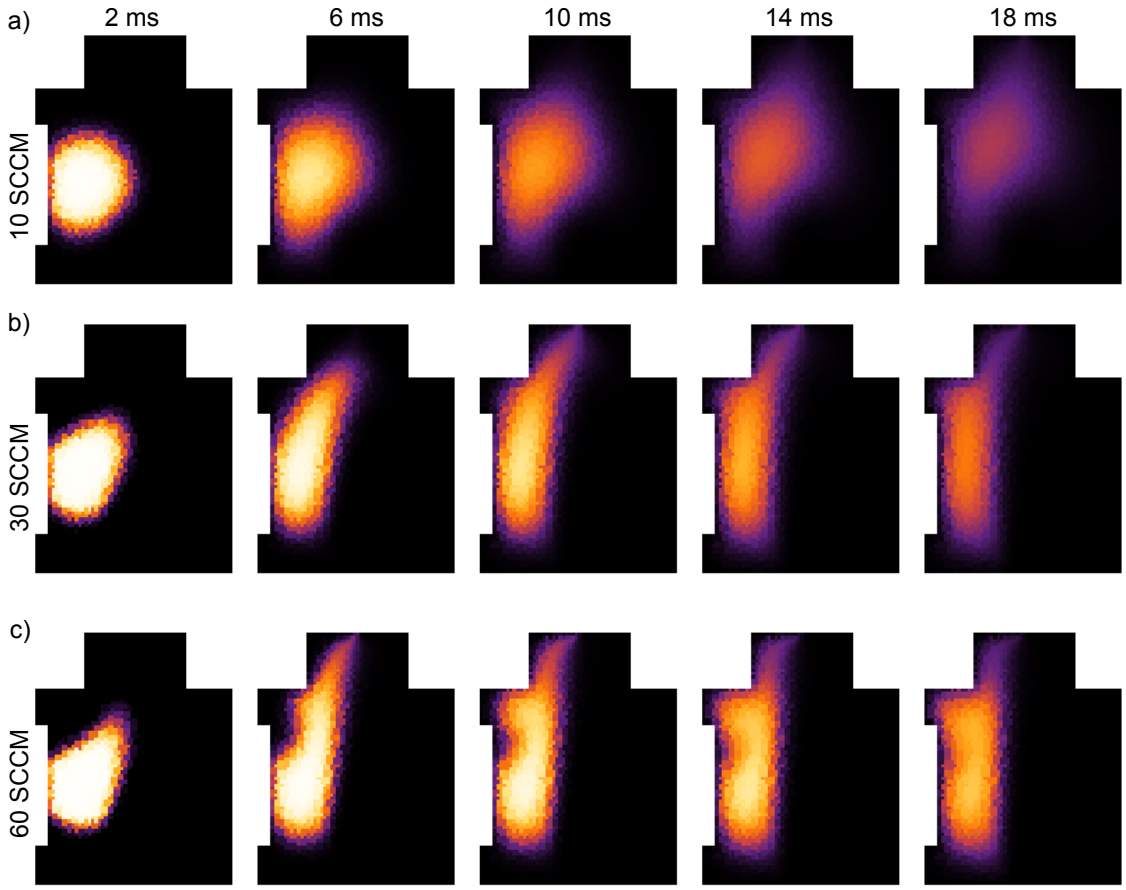

Figure 2.22: Evolution of Yb atoms in the cell for a flow of a) 10 SCCM b) 30 SCCM and c) 60 SCCM.

2.5 Conclusion

The properties of a Yb atomic beam produced from a buffer gas cell were measured. The Yb was produced through laser ablation of a solid metal target. It was found that this ablation raised the temperature of the helium in the cell by about 10 K. The helium then re-thermalised with the walls on a timescale set by the diffusion of heat to the walls, between 5 ms and 20 ms for the densities used in the experiment. This is longer than the expected thermalistion time of the atoms with the helium. A pressure broadening cross-section of $(1170 \pm 50) \times 10^{-20}\,\mathrm{m}^2$ at 4.7 K was observed for the Yb 556 nm transition.

The velocity of the atomic beam was measured with a slit aperture of dimensions $4 \times 0.75 \times 1$ mm. The average velocity was found to increase from $65\,\mathrm{m\,s^{-1}}$ at 1 SCCM to $204\,\mathrm{m\,s^{-1}}$ at 60 SCCM, which corresponds to the supersonic velocity of helium at 4 K. The velocity is also affected by the temperature of the helium in the cell as the atoms which leave the cell first are faster than the atoms that leave later. The temperature of the beam is (2.4 ± 0.3) K at flows above 5 SCCM showing that there is some cooling as the beam expands out of the aperture. The beam is exceptionally well collimated with a minimum divergence of 12° for flows of 30 SCCM to 40 SCCM which fits with a simple model where all collisions occur in the aperture where the gas flow is highly collimated.

A slit of dimensions $8 \times 1 \times 1$ mm was also used. The velocity of the beam was $100\,\mathrm{m\,s^{-1}}$ at 10 SCCM and $154\,\mathrm{m\,s^{-1}}$ at 40 SCCM. These velocities are lower compared to those when the smaller slit was used, which can be attributed to the lower helium number density in the cell for the same flow. The divergence of the beam is similar for both slits and the temperature appears to be slightly higher for the larger slit.

The motion of helium in the cell was modelled using a computational fluid dynamics program. The velocity of the atomic beam fits well with the bulk helium velocity predicted by the simulation. The helium flow was found to have a large effect on the extraction efficiency of the cell. Atoms loaded into the central column, where the helium is travelling fastest towards the aperture, are swept out quickly and efficiently. Atoms that are loaded into other areas of the cell, where the helium is travelling away from the aperture and has a low velocity, must diffuse to the central column before they are extracted from the cell. These effects create a time-of-flight profile consisting of a peak with a long tail. As the flow is increased the width of the peak decreases, as the helium is travelling faster, while the length of the tail increases, as it takes longer for the Yb to diffuse to the central

column. To optimise the extraction efficiency the majority of the Yb must be loaded into the central column at a flow for which the transit time of helium through the cell is shorter than the diffusion time to the walls.

Chapter 3

Creating a Beam with Pulsed Helium Flow

3.1 Introduction

Molecular beams that are both slow and intense have been created using a buffer gas source, however using a supersonic jet of helium to produce a molecular beam is expected to have some advantages over a buffer gas source for certain applications. It is also of interest to directly compare a cryogenic buffer gas source to a cryogenic supersonic jet source. In this chapter the molecular beams produced from two cryogenic pulsed supersonic sources have been characterised.

To create a supersonic jet gas is typically held in a valve at high pressure, then released into vacuum through a small nozzle. As the gas expands, its thermal motion is converted into forward motion through collisions, cooling the expanding gas. As the gas travels further from the valve nozzle the forward velocity of the beam continues to increase, while the number of collisions decreases. The forward velocity then tends towards a limiting value given by equation 2.18. This limiting velocity is reduced by decreasing the initial temperature of the gas. As the temperature is lowered the gas will begin to condense in the valve and so the pressure will decrease. At a certain temperature the vapour pressure will no longer by sufficient for supersonic expansion. The corresponding limiting velocity is the minimum supersonic velocity that can be achieved for a particular gas. Table 3.1 shows the final velocity of a number of noble gases at their boiling point at 1 bar. As 2.18 depends on both the mass and the temperature of the carrier gas, a heavy atom with a high boiling point can have a supersonic velocity close to that of a lighter and colder atom. The

heavier atoms will transfer more energy to the molecules in the direction perpendicular to the beam direction and so increase the divergence of the beam. It is therefore preferential to use lighter atoms [88]. Noble gases are used as carrier gases for supersonic jets as they do not react with the species of interest.

Gas	Helium	Neon	Argon	Krypton	Xenon
T (K)	4.4	27.3	87.4	121.5	166.6
$u_{\max}$ ($\mathrm{m\,s^{-1}}$)	204	237	301	244	229

Table 3.1: Final forward velocity, $u_{\max}$, calculated from equation 2.18 for a number of noble gases at temperature T, where T is the boiling point of the element at 1 bar.

As the valve is only open for a short time per pulse the amount of helium entering the vacuum chamber is reduced. This increases the lifetime of the charcoal sorbs used to absorb the helium, and reduces the background gas level in the chamber. Shorter molecular pulses can also be produced, as they are limited by the length of the gas pulse rather than the diffusion time through the helium. The valve is typically opened for 200 µs leading to pulses that are much shorter than the 50 ms long pulses that the buffer gas cell produces. This makes supersonic jet sources attractive for use with a travelling wave decelerator. In the first part of this chapter a pulsed jet source is characterised for use with the travelling wave decelerator, which is described in chapter 4.

3.2 Cryogenic Supersonic Jet

In the experiment described in this section a General Valve Series 99 solenoid valve was used to produce a supersonic molecular beam at cryogenic temperatures using the cryocooler assembly described in 2.1. This valve produces a supersonic jet of helium into which YbF is seeded. The high density of helium above the valve nozzle acts as a refrigerant for the YbF molecules, cooling all the degrees of freedom of the molecule. The molecules are also accelerated forward by the motion of the helium atoms, leading to a cold molecular pulse travelling at the supersonic speed of helium.

3.2.1 Source Construction

A series 99 valve contains a solenoid and a magnetic armature as shown in figure 3.1a). When a current passes through the solenoid the armature is pulled back into the valve.

This retracts a plastic poppet, allowing gas to leave the valve. When no current flows through the solenoid a spring behind the armature applies force to the poppet to keep the valve closed. The faceplate is screwed onto the main body of the valve and compresses a copper gasket to prevent gas leaking out. As this valve was designed to work at room temperature it was found that certain modifications could be made to improve its performance at low temperatures.

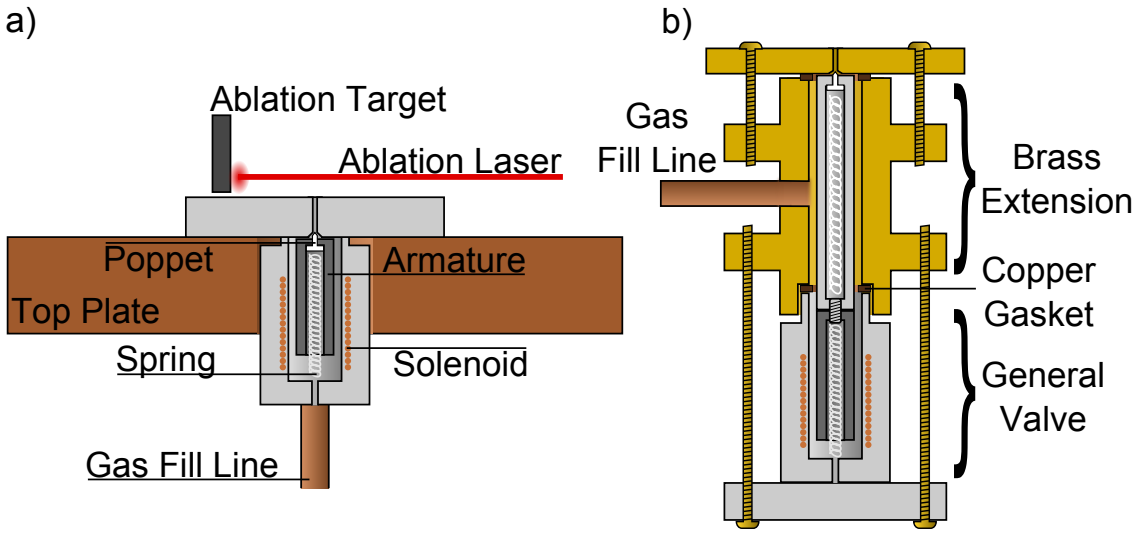

Figure 3.1: a) The on-axis valve set up using a stock General Valve Series 99 solenoid valve. b) The modified valve.

It was discovered in initial experiments that the ability of the solenoid valve to create a slow gas jet at cryogenic temperatures is hindered by the fact that the solenoid heats the gas as it travels through the valve. This effect has been reported by other groups studying solenoid valves at cryogenic temperatures [89, 90]. The steel construction of the valve also reduces the thermal conductivity of the valve, increasing the time it takes to thermalise with the cold plate. As the velocity of a supersonic jet is dependent on the temperature of the gas in the valve these effects result in a faster beam. To prevent the gas from interacting with the solenoid as it travels through the cell an extension was added to the main body of the valve, as shown in figure 3.1b). A new gas fill line was added to the extension to provide a path to the outlet that did not pass the solenoid. The original gas feed line was blocked with a Swaglok blank. The extension was made of brass, which has a higher thermal conductivity than steel, to decrease the time the valve takes to thermalise with the cold plate. An extension was also made for the armature and connected with a

grub screw. The spring in the original armature was then in contact with this grub screw, rather than the poppet. To ensure the valve remained sealed a second spring was inserted into the armature extension to apply pressure to the poppet. It was found that the length of the armature extension had to be accurate to within 100 µm for the valve to operate correctly. If it was too long there was insufficient space for the valve to open fully when the solenoid was activated and if it was too short gas would continually leak out the front of the valve. The length was altered by introducing a spacer between the armature and its extension.

To open the valve a custom circuit was built which applied a large voltage difference across the solenoid for a short time, 200 µs unless otherwise stated. A large voltage was required to ensure the valve was fully opened in the short time the current was being applied. As the large currents generated when the valve closed could damage the thin wires used for the temperature sensors 0.25 mm thick wire was used to connect the valve to the electrical feedthrough.

The valve was mounted on a copper 'top' plate 122 mm above the cold plate, as shown in figure 3.2. This provided sufficient clearance for the valve to sit on-axis above the cold plate. The top plate was mounted on four copper legs but could be thermally disconnected from the cold plate by replacing the copper legs with steel legs. This allowed the temperature of the top plate to be set using heaters so that different carrier gases, such as neon, could be used. YbF was created by ablating a solid precursor of 70% Yb and 30% AlF_3, which was positioned 3 mm from the nozzle of the valve. This target was a disc with a diameter of 15.5 mm and a depth of 3 mm. For the majority of the experiments described in this section the ablation laser used was the same as described in 2.1. Any variations will be indicated in the corresponding section. The beam was characterised using two techniques. Firstly a fast ionisation gauge (FIG) was used to measure the gas pulse. Secondly the LIF detection setup described in section 2.1.1 was used to directly probe the YbF molecules at various positions above the valve nozzle. The molecules were excited on the $A^2\Pi_{1/2}(v=0) \leftarrow X^2\Sigma^+(v=0)$ transition from the ground rotational level at a wavelength of 552 nm.

3.2.2 Fast ion gauge measurements

Supersonic pulses of helium were recorded with a fast ion gauge (FIG). The stock solenoid valve was cooled to cryogenic temperatures and the FIG was positioned above the radiation

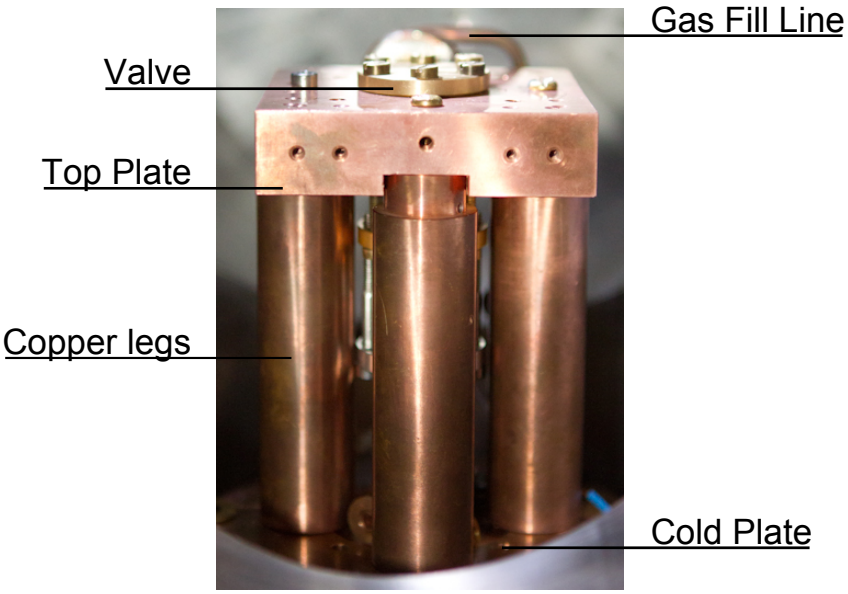

Figure 3.2: Photograph of the top plate used to hold the valve above the cold plate. Copper legs are used to thermally anchor the top plate to the cold plate.

shield shown in figure 2.2, 230 mm from the valve nozzle. The FIG could not be positioned closer to the valve as it contained a heated filament which would increase the temperature of the cold plate. The length of time a voltage was applied to the valve was varied from 200 µs to 1000 µs. The voltage required to produce a gas pulse increased from ~70 V at 1000 µs to ~300 V at 200 µs. A higher voltage was required for shorter pulse times as the solenoid must be retracted faster to ensure the valve opens fully.

The gas pulse produced by the valve can be disrupted if a surface is positioned too close to the valve nozzle. To ensure the ceramic target used to produce the YbF would have no effect on the expanding gas, rods with different diameters were placed 3 mm from the nozzle. Figure 3.3 shows the time-of-flight profile of the gas pulse as it passes the FIG without a rod, and with rods of diameter 10 mm and 15.5 mm next to the nozzle. All the profiles consist of a peak at 750 µs followed by a long tail. The peak corresponds to the time the gas pulse passes the FIG and the long tail is due to the slow pumping of helium from the room temperature section of the vacuum chamber. The shape of the profile does not change significantly when there is a rod next to the nozzle. There is a change in the amplitude of the gas pulse however this can be attributed to slight changes in the voltage applied to the valve. This indicates that a target with a diameter of up to 15.5 mm can be used without affecting the gas jet.

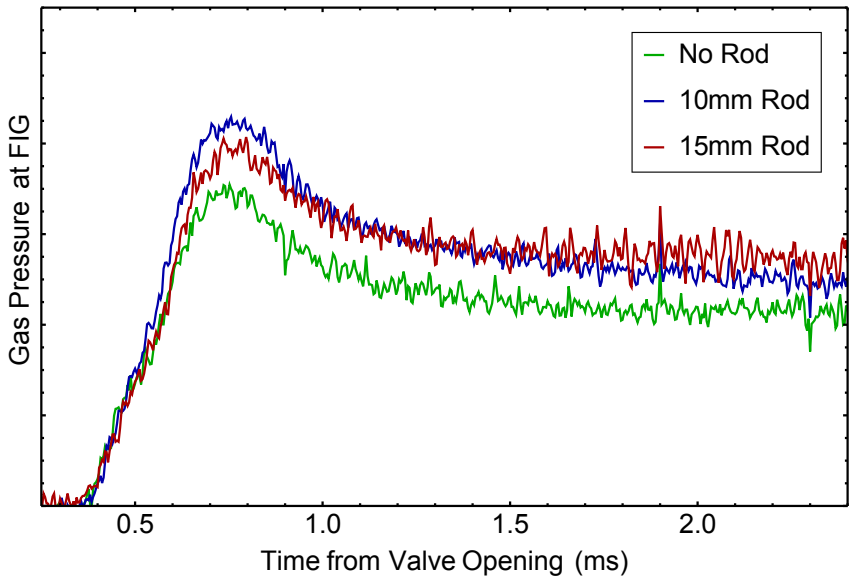

Figure 3.3: Time-of-flight profiles showing the pressure recorded by a fast ion gauge when different diameter rods are used to simulate the presence of a target.

Figure 3.4a) shows a time-of-flight profile of a gas pulse measured 698 mm from the valve nozzle in the vacuum system described in section 4.3. The pumping speed was better in this vacuum system so no long tail is seen in the profile. A Gaussian distribution was fit to the profile and the position of the peak used to gauge the forward velocity of the gas pulse. Figure 3.4b) shows how the forward velocity varied with the voltage applied to the valve. All the velocities measured are higher than the supersonic velocity expected for helium at the temperature of the top plate, and the velocity increases as the voltage across the solenoid increases. This fits with the model of helium gas being heated inside the valve by the solenoid. With a voltage of 160 V across the solenoid the velocity of the gas corresponds to a temperature of 7.0 K, whereas a voltage of 200 V heated the gas to 8.8 K.

3.2.3 Molecular Beam Characterisation

In a supersonic jet the number of molecules emitted at a given time with forward velocity between v and $v + dv$ can be approximated by a Gaussian of the form [91]

$$f(v)dv = Av^3 \exp\left(-\frac{M}{2k_BT}(v - v_0)^2\right) dv, \tag{3.1}$$

where M is the mass of the molecules, v_0 is the centre velocity of the pulse, T is the translational temperature of the molecules and A is a normalisation constant. Applying

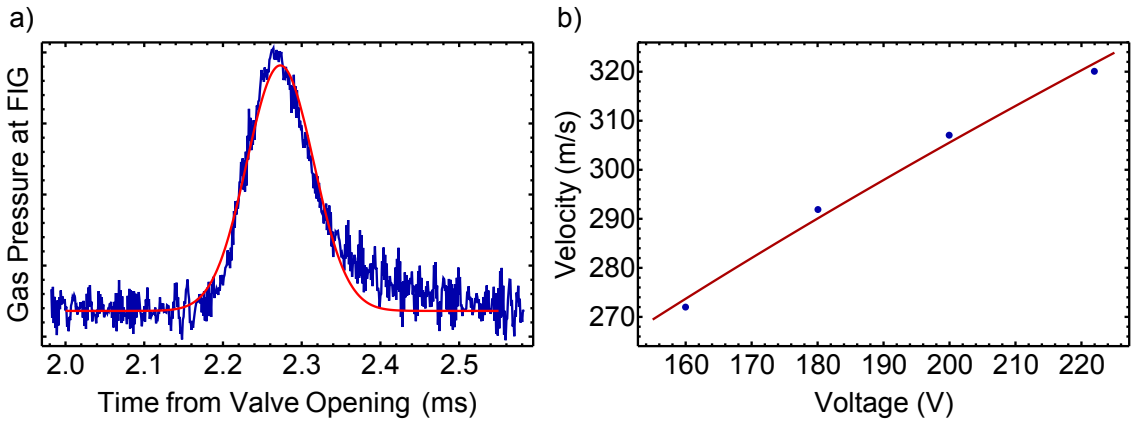

Figure 3.4: a) A time-of-flight profile of the helium gas pulse measured with a fast ion gauge 698 mm downstream of the valve, with 200 V across the solenoid. b) The change in the forward velocity of the molecular pulse as the voltage applied to the valve is increased.

the Jacobian of the transformation from velocity to time space ($dv = -\frac{L}{t^2}dt$ where L is the distance from the valve nozzle to the detector) results in an equation which describes the time-dependent signal produced by these molecules

$$g(t)dt = \frac{L}{t^2} f\left(\frac{L}{t}\right) dt = A\frac{L^4}{t^5} \exp\left(-4\ln 2\,\frac{(t-t_0)^2}{w(t)^2}\right) dt, \tag{3.2}$$

where $w(t) = (8\ln 2\, k_\mathrm{B} T t^2/(M v_0^2))^{1/2}$ is the time-dependent FWHM of the pulse. In order to obtain the full time-of-flight profile for the molecular pulse it is necessary to convolute this function with a function that describes the rate of emission from the valve over time. This gives the pulse some initial width that is not due to the temperature of the molecules. This has the effect that the width of a single time-of-flight profile can only be used to obtain an upper limit to the temperature. When there are two well-separated detection regions present in the molecular beam a value for the translational temperature can be obtained using the equation [92]

$$T = \frac{M v_0^2}{8\ln 2\, k_\mathrm{B}} \frac{w_2(t_2)^2 - w_1(t_1)^2}{t_2^2 - t_1^2}, \tag{3.3}$$

where w_1, w_2, t_1 and t_2 are the widths and central arrival times recorded at the upstream and downstream detection regions.

The time-of-flight profile of the molecular beam was recorded using the LIF setup described in section 2.1.1. The profile was integrated to obtain the total number of photons detected per pulse. To convert this to the number of molecules in the beam the detection efficiency was determined. The solid angle of the detection region, and any absorption

from the optical components, was measured by placing a 0.5×0.5 mm LED with a known power output at the focal point of the LIF imaging system inside the vacuum chamber. A Thorlabs PM100 power meter was then used to measure the power at the position of the PMT. The fraction of light transmitted by the detection optics was found by comparing the known output of the LED with the power measured at the PMT position. This value was combined with the quantum efficiency of the PMT taken from the manufacture's datasheet to obtain the efficiency of the detection region, η_D which was found to be 0.4%. The following equation could then be used to calculate the total number of molecules per steradian per pulse,

$$N_{\text{mol}} = \frac{N_D}{\eta_D} \frac{d^2}{A}, \tag{3.4}$$

where N_D is the number of photons detected per pulse, d is the distance between the aperture and the detection region and A is the area of the molecular beam that is detected. The main uncertainty in this calculation is the fraction of light transmitted by the detection optics and results in a value for the detection efficiency which is accurate to within a factor 2.

Helium and Neon Carrier Gases

The stock solenoid valve was used to produce a molecular beam with both helium and neon carrier gases. Figure 3.5 shows time-of-flight profiles of the molecular pulse when helium carrier gas was used, along with fits to equation 3.2. For these profiles the distance between the detectors was 255 mm and the top plate was at 7.3 K. The largest number of molecules per pulse was obtained when a voltage of 233 V was applied to the valve with 2 bar backing pressure. A pulse energy of 128 mJ was used to ablate the target at 5 Hz.

The position of the peaks in the time-of-flight profiles were compared to obtain the velocity of the molecular pulse. For the profiles shown the forward velocity was found to be $400\,\text{m}\,\text{s}^{-1}$, which corresponds to an initial helium temperature of 15 K. From the measurements of the helium pulse with a FIG it is known that a voltage of 233 V across the solenoid will heat helium in the valve by ~4 K. This leaves some velocity slip between the expected velocity of the helium and the velocity of the molecules. This velocity slip has been observed in other supersonic molecular beams [93, 94]. Altering the repetition rate of the valve changed the velocity of the molecular pulse from $340\,\text{m}\,\text{s}^{-1}$ at 1 Hz to $425\,\text{m}\,\text{s}^{-1}$ at 10 Hz. Decreasing the repetition rate allows the valve more time to cool between pulses so decreases the temperature and velocity of the carrier gas. The translational temperature

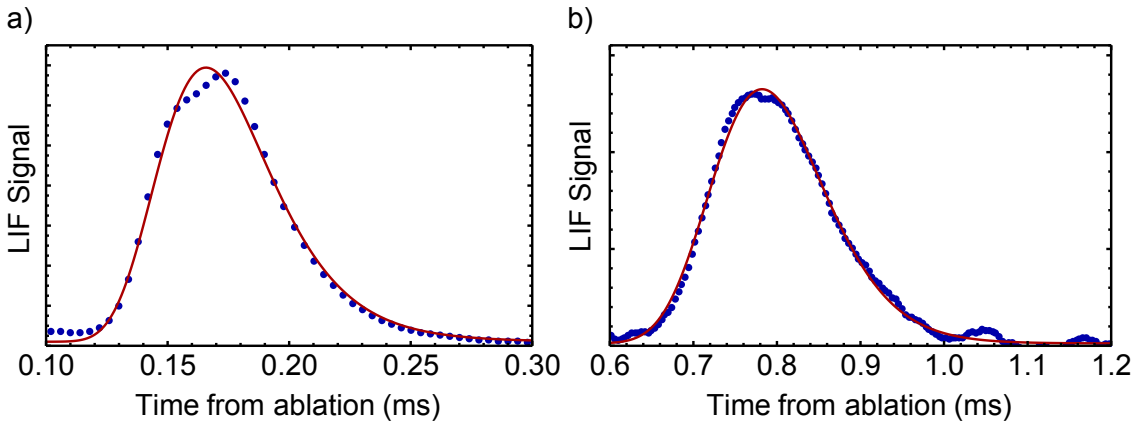

Figure 3.5: Time-of-flight profiles of YbF, a) 50 and b) 305 mm from the valve nozzle. The solid lines are fits to equation 3.2.

of the molecular pulse was calculated from equation 3.3 and found to be 23 K. This is higher than has been observed in other supersonic molecular beams and suggests that the number of collisions between the helium and YbF is insufficient to cool the molecules to the helium temperature.

Figure 3.6 shows the number of molecules per steradian per pulse as a function of the number of times the ablation laser is fired. The number of molecules detected decreases as the target is ablated. The number of detected molecules is halved after 1000 shots, or 3 minutes when the ablation laser is fired at 5 Hz. After a long period of ablation deep channels are visible on the surface of the target and the area appears darker. This change in the surface of the target alters the interaction with the ablation laser and decreases the yield of YbF. Filing down the target until it is flat can refresh the surface, however this is impractical for sustained production of a YbF beam. By rotating the target the lifetime of the target is increased and a molecular beam can be produced for significantly longer before the target must be refreshed.

Neon was also used as a carrier gas with the solenoid valve and the effect of altering the temperature of the top plate was explored. A lower backing pressure of 1.2 bar was used, at this pressure the neon will liquefy at 28 K. To optimise the number of molecules detected the voltage applied to the solenoid was increased to 417 V. The temperature of the top plate was altered with resistive heaters attached to the copper, and measured with the temperature sensors described in 2.1.

The forward velocity was found to decrease with decreasing top plate temperature,

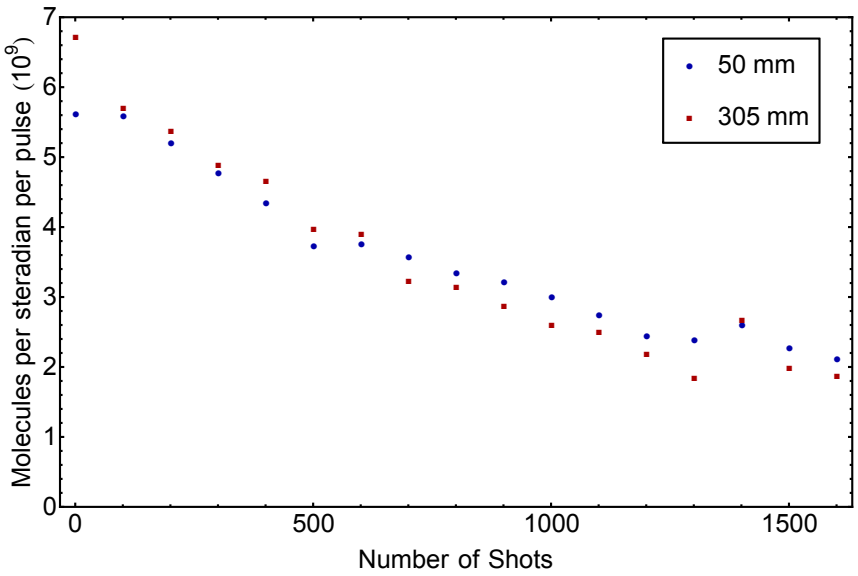

Figure 3.6: Number of molecules per steradian per pulse recorded at two detectors, as a function of the number of times the target was ablated.

from 373 m s^{-1} when the top plate was held at 30 K to 330 m s^{-1} when the top plate was at 24.5 K. When the temperature of the top plate was reduced further the neon gas froze inside the gas line and no molecular beam was detected. Temperatures lower than the boiling point of neon could be used as the heat from the solenoid vapourised enough neon inside the valve to produce a supersonic expansion. This enabled the production of a beam with a velocity lower than the helium jet characterised. The translational temperature of the pulse was found to be 11 K with no dependence on the top plate temperature. This is lower than the temperature observed with a helium carrier gas as the heavier neon removes more energy with each collision. The number of molecules produced per steradian per pulse was similar to that produced with a helium carrier gas.

Stock and Modified Solenoid Valves

In a different experiment, molecular beams produced with the stock and modified solenoid valves were detected in a single region, 698 mm from the valve nozzle. The ablation laser used was a Nd:YAG, frequency doubled to 532 nm with a pulse energy of 20 mJ and fired at 10 Hz. The top plate had a temperature of 4.2 K. A voltage of 185 V was used to open the valve.

A time-of-flight profile was recorded using LIF and equation 3.2 was fit to the profiles.

The translational temperature was taken from equation 3.2 and the lowest value was found to be 6.8 K for both the stock and modified valves. This is an upper limit on the temperature of the pulse as there is a single detector, however it is expected to be close to the true temperature as the detector is far from the source. The translational temperature is expected to be the same for both valves as it does not depend on the initial temperature of the gas. It is due to the expansion from the nozzle, which was not altered between the two valves. The fact that the temperature is lower than previously measured could be due to the lower ablation energy required when using the frequency doubled Nd:YAG laser. This may give the YbF molecules a lower initial temperature.

The velocity of the pulse was found to be $367\,\mathrm{m\,s^{-1}}$ for the stock valve and $315\,\mathrm{m\,s^{-1}}$ for the modified solenoid valve. A lower velocity was achieved when using the modified valve as the helium had less interaction with the solenoid as it travelled through the valve. Using equation 2.18 it was found that the helium gas was 3 K colder in the modified valve. The velocity of the pulse was not found to decrease to the supersonic velocity of helium. The lowest velocity recorded with the modified valve was $308\,\mathrm{m\,s^{-1}}$ which corresponds to a helium temperature of 9 K, so a slower beam could be achieved with further improvements to the cooling of the helium before it expands.

3.3 Solenoid Valve with Open Cell

A source was developed that combined aspects of the solenoid valve with the buffer gas source. It was designed such that a short, cold pulse of helium would enter a cell directly in front of the YbF precursor as the ablation laser is fired. The helium gas would then expand to fill the cell and cool the YbF molecules. The cell slightly constrained the gas, providing an increased interaction time between the buffer gas and the hot molecules. This source should then produce beams that combine the high flux and low speed associated with a buffer gas beam with the short pulse of a supersonic beam.

3.3.1 Source Construction

The cell used is shown in figure 3.7. It was a copper cylinder with a radius of 15 mm and a height of 50 mm. The walls were 1 mm thick with several 5 mm wide slits along the length of the tube to provide optical access. Using open slits instead of windows prevented problems associated with the windows becoming coated in ablation products. The tube

was fully open at the top as the number density of helium provided by the pulsed valve is large enough to cool the YbF. A small aperture was then not required to increase the pressure inside the cell, as it would be with a continuous source.

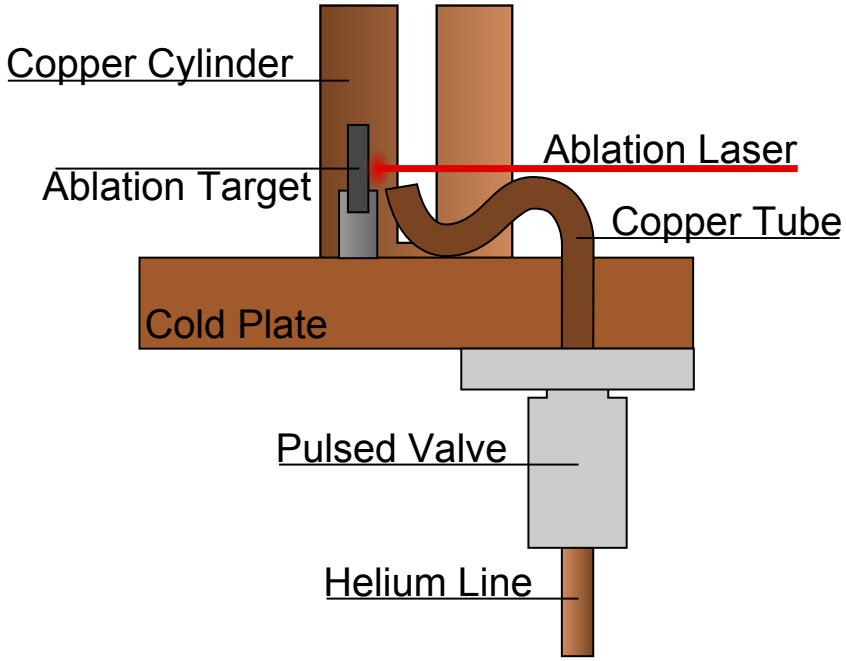

Figure 3.7: Diagram of the open cell source with the valve positioned off-axis

A General Valve Series 99 solenoid valve, with no modifications, was used to provide the pulse of helium to the cell. It was positioned under the cold plate, 55 mm from the centre. The valve was connected to the cell with a 1 mm diameter copper tube, which also helped cool the helium after it left the valve. As the tube entered the cell it was angled upwards and towards the target. This ensured that the helium interacted with the YbF plume, and had some momentum in the direction of the exit of the cell. The solid precursor was the same Yb\$AlF_3$ ceramic target as was used in the previous section and it sat in a notch on the end of a short aluminium rod with a set screw holding it in place. It was ablated with the same laser as described in section 2.1. The time between opening the valve and firing the ablation laser was varied in order to investigate how different conditions in the cell affected the molecular pulse. Molecules in their rotational ground state were detected 25 mm and 280 mm above the target using the LIF detection scheme described in section 2.1. The molecules were excited on the $A^2\Pi_{1/2}(v = 0) \leftarrow X^2\Sigma^+(v = 0)$ transition at 552 nm.

3.3.2 Results

After the valve has been opened the pressure in the tube is high. There is then a supersonic expansion from the tube exit. As the gas leaves the tube the pressure is reduced such that the beam becomes effusive. This results in a broadened gas pulse with a velocity which decreases with time. The number density and velocity of the molecular beam changes depending on which part of the gas pulse the YbF is ablated into. Figure 3.8 shows time-of-flight profiles for different delays between opening the solenoid valve and firing the ablation laser. When the ablation laser is fired before the gas pulse has reached the cell two peaks appear in the time-of-flight profile, shown in 3.8a). The first peak appears before the helium gas pulse has reached the cell and is due to YbF that is partially cooled by helium that has frozen to the target and is desorbed by the ablation laser. The initial peak has a typical velocity of $600\,\mathrm{m\,s^{-1}}$ as the helium density in the cell is too low to effectively slow these molecules. Molecules that have thermalised with the helium slowly diffuse out the cell, leading to the long tail in the pulse. When the gas pulse from the valve arrives it rapidly entrains the residual YbF in the cell, forming the second peak. This peak has a typical speed of $200\,\mathrm{m\,s^{-1}}$, since the YbF is fully thermalised and entrained in the helium flow. As the time between opening the valve and ablating the target is increased the gas pulse arrives sooner after the YbF is produced and the second peak appears earlier in the LIF profile, shown in 3.8b). Since there is more YbF at earlier times, the amplitude of the second peak is larger in this time-of-flight profile.

As the gas pulse and ablation plume begin to overlap the two peaks begin to merge to form a peak with a significantly larger amplitude, shown in 3.8c) and d). This is because the helium density is high enough that a much larger number of YbF molecules in the ablation plume are cooled and entrained in the helium flow. This single peak in the time-of-flight profile has a forward velocity of $\sim 350\,\mathrm{m\,s^{-1}}$.

If the delay between opening the valve and firing the ablation laser is increased still further, the YbF plume overlaps with the latter part of the gas pulse where the helium density and velocity is lower. The entrained YbF therefore has a lower velocity. The reduced helium density seems to lead to less complete entrainment, and some hot YbF molecules again start to form a fast peak at the beginning of the LIF profile, shown in 3.8e). As the delay is increased further, the helium density in the cell decreases and the amplitude of both peaks is reduced. There is a clear separation in time between the fast, uncooled YbF and a much slower diffusive YbF pulse, shown in 3.8f).

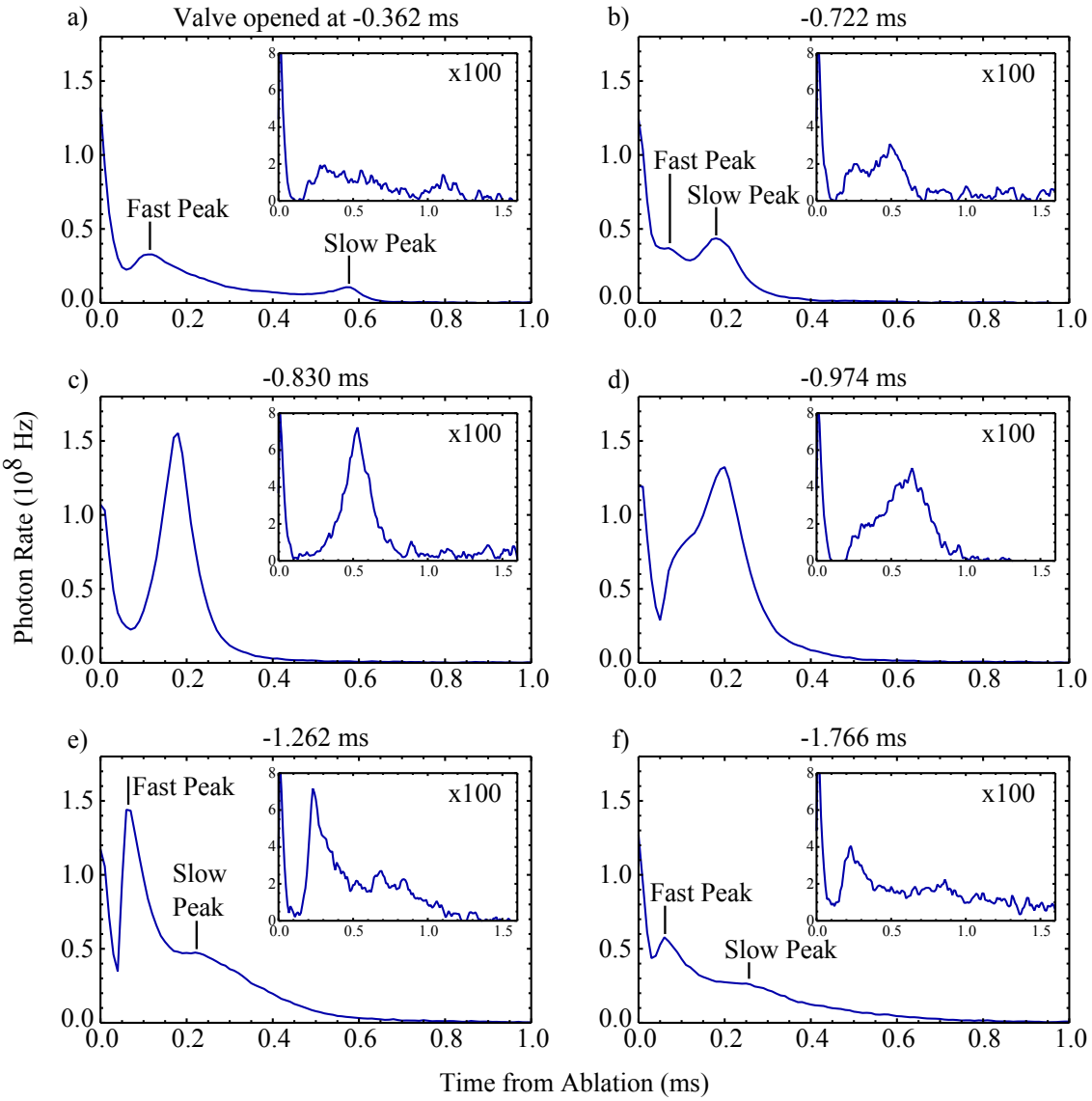

Figure 3.8: Laser induced fluorescence measurements of the YbF beam as the time between opening the valve and firing the ablation laser is varied. In all plots the ablation laser is fired at 0 ms which results in the decaying signal at early times. The main profile is from a detector 25 mm from the target and the inset is from a detector 156 mm from the target.

The optimum time between opening the valve and firing the ablation laser was found to be 1120 µs for a gas pulse length of 200 µs. Changing the length of the gas pulse altered this optimum time, but not the molecular beam characteristics. Figure 3.9 shows a time-of-flight profile for a molecular beam produced under optimum conditions, with a fit to equation 3.2. The forward velocity was found to be $(206 \pm 5)\,\mathrm{m\,s^{-1}}$ with a translational temperature of $(12.3 \pm 0.5)\,\mathrm{K}$. These results compare favourably with those from the cryogenic source without a thermalisation cell. By cooling the helium after it leaves the valve, and using a thermalisation cell, the forward velocity is reduced to that expected from a supersonic expansion of helium at 4 K and the temperature is halved. The total number of molecules detected per stedradian per pulse is 4.5×10^{10} which is an increase on the number detected with an on-axis valve. This is probably due to the increased interaction time between the YbF and helium leading to a greater degree of cooling and entrainment of the ablation plume.

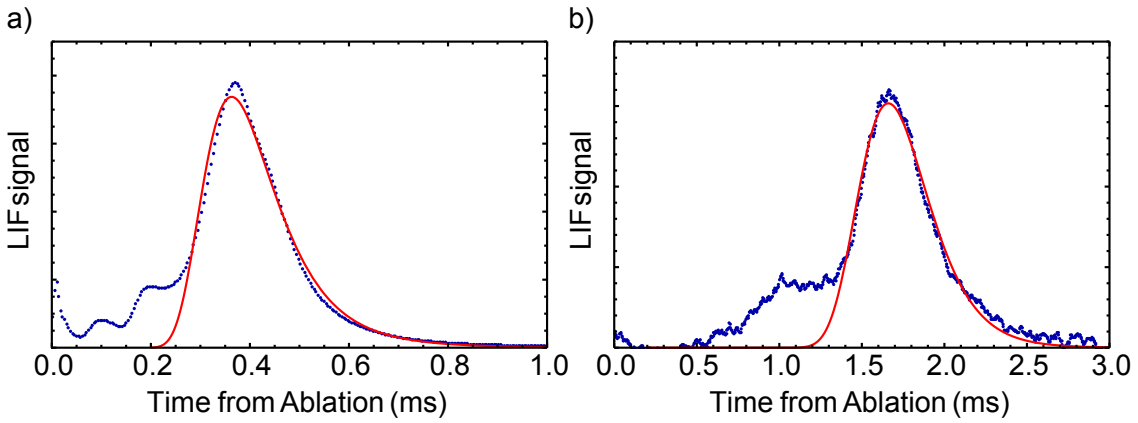

Figure 3.9: Time-of-flight profiles of YbF for the open cell source under optimal conditions, taken a) 25 and b) 280 mm from the target

3.4 Conclusion

The molecular beam produced by a General Valve series 99 solenoid valve was characterised under different conditions. YbF was produced by ablating a solid precursor target of Yb/AlF_3, before becoming entrained in the gas jet from the valve. Continued ablation of a single area on the precursor target led to a reduction in signal as the surface was altered. The maximum beam intensity was 6×10^9 molecules per steradian per pulse. The typical

full width half maximum (FWHM) of the molecular pulse was ~100 µs.

The translational temperature was found to depend on the power of the ablation laser used to produce the molecules, and the carrier gas used. For a helium carrier gas the translation temperature was 23.3 K with an ablation pulse energy of 128 mJ, while a reduction in pulse energy to 20 mJ resulted in a minimum temperature of 6.8 K. A lower pulse energy could be used as the frequency of the ablation laser was doubled, leading to a wavelength of 532 nm rather than 1064 nm. Changing the carrier gas from helium to the heavier neon reduced the temperature to 11 K with a pulse energy of 128 mJ. The temperature was found to be independent of the carrier gas temperature.

The velocity of the pulse was found to depend on the temperature of the carrier gas as expected from equation 2.18. When the stock solenoid valve was used with 200 V across the solenoid, the velocity of the beam corresponded to a temperature 8 K higher than the temperature of the top plate. This heating can be attributed to the solenoid in the valve as the amount the gas was heated increased as the voltage applied to the solenoid was increased. A brass extension was added to the valve which allowed the helium to leave the valve without passing the solenoid. The velocity of the beam then corresponded to a temperature 5 K above the top plate temperature.

It was found that the velocity and temperature of the beam could be reduced by sending the helium pulse through a cooled copper tube and into an open copper cylinder. The YbF was produced in the cylinder and then entrained in the helium pulse. The intensity of the beam was increased by a factor 10 over the standard supersonic source while the length of the molecular pulse increased to ~200 µs. This source was used to measure the Franck-Condon factors as described in chapter 5. It also informed the design of a new source described in chapter 6.

Chapter 4

Deceleration of YbF in a travelling-wave decelerator

4.1 Introduction

The sources discussed in chapter 3 are suitable for providing high intensity molecular beams with velocities of hundreds of meters per second, greatly improving the sensitivity of current precision measurements. A further improvement in sensitivity is possible if the forward velocity of the molecules is reduced with as little reduction in number density as possible [95]. One possible method for achieving this is to use a Stark decelerator [34].

The Stark effect is a change in the energy levels of an atom or molecule in the presence of an electric field. If the electric field has a gradient the molecule will experience a force in the direction that minimises its internal energy. The energy levels can be shifted to higher or lower energies and so the molecule can experience a force towards or away from an area with a higher electric field. If the particle is accelerated towards an area with a lower (higher) electric field it is known as a weak (strong) field seeker. The Stark effect can be used to slow down weak-field seeking polar molecules by introducing a positive electric field gradient in the direction that the molecule is travelling.

In a weak-field (WF) Stark decelerator this field gradient can be created using a series of electrodes as shown in figure 4.1. They are arranged such that the molecules travel between two parallel electrodes with each pair positioned 90° to the previous pair. To produce an electric field gradient the even-numbered electrodes are set to V_{high} and the odd are set to V_{low}. The electric field then changes sinusoidally along the decelerator and molecules are decelerated as they travel towards an electrode pair. Once the molecule is

close to the electrode the field is switched so the odd electrodes are held at V_{high} and the molecule is in a field minimum. This is repeated along the decelerator and energy is removed from the molecule each time the field is switched. As adjacent electrode pairs are perpendicular to each other the direction of confinement in the transverse direction changes as the molecules travel from one electrode pair to the next. Averaged over the length of the decelerator the molecules are confined radially [96]. When the molecules in the decelerator are travelling at low speeds the time they spend in an area where they are not confined in one transverse direction increases. This leads to losses which are amplified when a long decelerator is required [97].

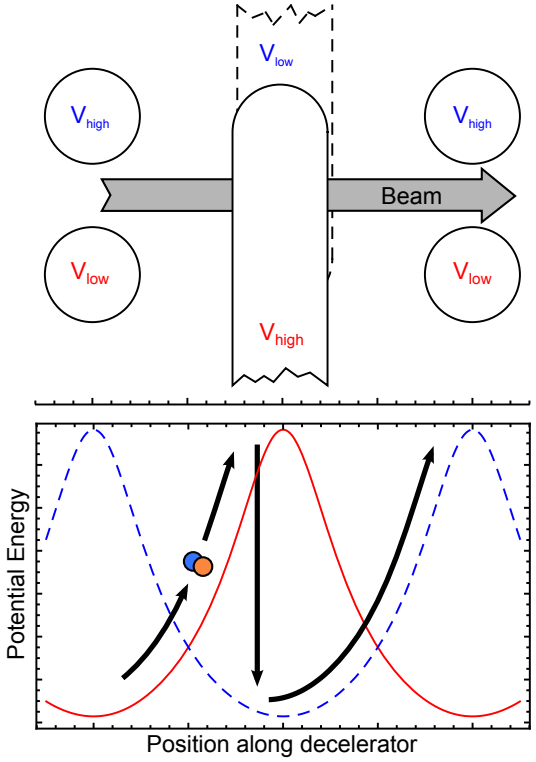

Figure 4.1: Diagram of the electrode pairs in a weak field decelerator and the potential energy of a molecule as it travels along the decelerator.

Heavy molecules, such as YbF, are hard to decelerate in a WF Stark decelerator as only weak field seeking molecules are confined radially and the lower rotational levels of YbF become high field seeking in relatively weak electric fields, as shown in figure 4.2. This limits the field strength at the electrodes, and so the amount of kinetic energy that can be removed in each deceleration stage. As heavy molecules have a large amount of kinetic energy many decelerator stages are required which results in a long decelerator.

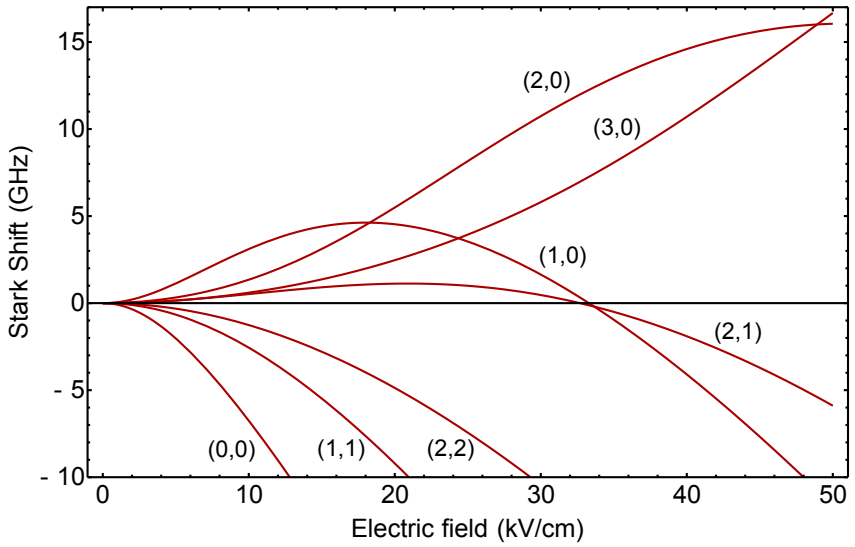

Figure 4.2: The change in Stark shift with increasing electric field for the lowest lying (N, M_N) states of YbF, where N is the rotational level and M_N is the magnetic substate. The Stark shift is shown relative to the energy of the rotational state with no applied electric field. These Stark shifts were calculated by Mike Tarbutt.

To negate some of these issues a decelerator was designed which could decelerate molecules in strong-field seeking states, known as an alternating gradient (AG) decelerator [37]. In this decelerator the molecules are alternately focussed and defocussed at each deceleration stage and an overall net focussing achieved through careful arrangement of the electrodes. It was successfully used to slow molecules but suffered from low acceptance and difficult construction [98].

This chapter demonstrates the use of a new kind of decelerator for slowing heavy molecules. In this decelerator the molecules are confined in three dimensions in a trap which moves along the length of the decelerator with the molecules. The fields used to trap the molecules can be kept below the level at which the molecules become strong field seeking, and so all the molecules that are trapped at the start of the decelerator will be guided to the exit. By decelerating the traps the kinetic energy of the molecules can be reduced while maintaining a high number density. The deceleration of YbF with a travelling wave decelerator will be discussed. The results in this chapter were previously published in [99].

4.2 The Travelling Wave Decelerator

The decelerator was designed and built at the Fritz-Haber Institute in Berlin [100] which is also where the experiment was performed. A previous demonstration of this decelerator is given in [39]. The decelerator was composed of 320, 4 mm diameter rings with the molecular beam passing through the centre of each. The separation of adjacent rings was 1.5 mm and they were connected to eight 6 mm diameter stainless steel poles which ran parallel to the beam as shown in figure 4.3. The structure was periodic such that every 8th ring was attached to the same pole. The first ring was centred 29 mm above the tip of the skimmer.

A sinusoidal voltage was applied to each pole of the form,

$$V_n(t) = V_0 \cos\left(\phi(t) + 2\pi\frac{n}{8}\right), \tag{4.1}$$

where V_0 is the amplitude of the applied voltage, n is the number of the pole from 1 to 8 and $\phi(t)$ is a time-dependent phase. Figure 4.4 shows the potential energy of a YbF molecule inside the decelerator when $\phi = 0$, $\phi = \pi/16$ and $\phi = \pi/8$. As the value of ϕ is increased the trap minimum moves along the decelerator. By expressing ϕ as $\int_0^t \omega(\tau)\,\mathrm{d}\tau$, where $\omega(\tau)$ is the time dependent frequency of the voltage applied to each electrode, the velocity of the trap at time t is

$$v(t) = \frac{\omega(t)}{2\pi}L, \tag{4.2}$$

where L is the period length.

The value of V_0 used when decelerating YbF was 10 kV which corresponds to a maximum electric field of 37.3 kV/cm along the centre of the trap. At this electric field, the Stark shift is -2.3 GHz for the $(N,\ M_N) = (1,0)$ state, 13.8 GHz for the (2,0) state and 9.2 GHz for the (3,0) state. The acceptance of the decelerator is highest for molecules in the (2,0) state.

The trajectories of molecules travelling through the decelerator were modelled using a Monte Carlo simulation. A program written specifically for use with this decelerator was used to predict the arrival time of molecules at the detector. This program was originally written by Sam Meek and was adapted to run on the Imperial College computing cluster. An initial distribution of molecules was created with parameters taken from the source characterisation discussed in section 3.2. The only unknown was the longitudinal distribution of the pulse in the decelerator which is set to be a Gaussian distribution with full width half maximum of 9.4 mm. The trajectory calculation was terminated if

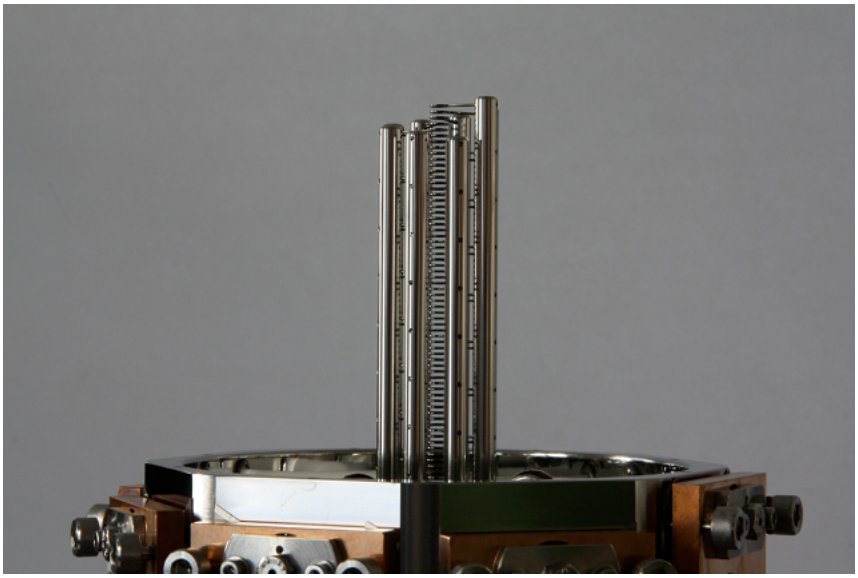

Figure 4.3: Photograph of the upper section of the travelling wave decelerator taken at the Fritz-Haber Institute in Berlin. Reprinted with permission from Meek, S. A. et al. Rev. Sci. Instrum. 82, 093108 (2011). Copyright 2011, American Institute of Physics.

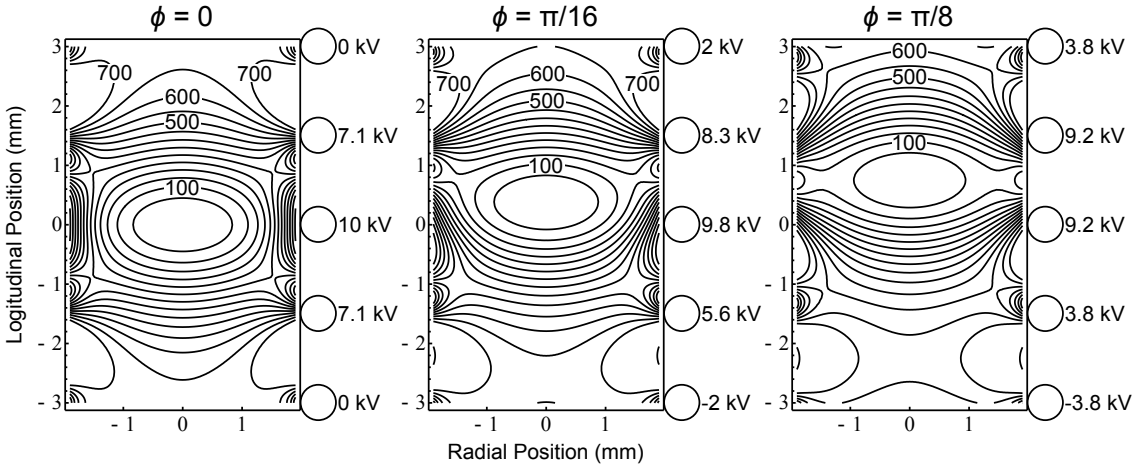

Figure 4.4: The potential energy of YbF in the (N, M_N) = (2,0) state as a function of position inside the decelerator and for different values of ϕ. The contours are labelled in mK and the voltages applied to the surrounding rings are shown on the right of each image. The amplitude of the applied voltage is 10 kV.

the molecule did not pass through the skimmer, or if it reached the radius of the rings. The electric field generated by the decelerator was approximated by a sum of sinusoidal functions in the direction along the decelerator, and a sum of Bessel functions in the radial direction. This is the general solution to Laplace's equation, where the solution is cylindrically symmetric, bounded at $r = 0$ and periodic in z with a period length L. The coefficients used are obtained by taking the Fourier transform of a numerically-calculated potential along the line $r = 0$ over one period. The acceleration of each molecule was then calculated from the Stark shift induced by this field. The Stark shift of molecules in the (2,0) state were used in the simulation. The time taken for the molecules to reach the detection region was recorded and binned to produce simulated time-of-flight profiles.

4.3 Experiment

The cryogenic pulsed valve source described in section 3.2 was used to produce a molecular beam of YbF that was subsequently slowed in a travelling trap decelerator as shown in figure 4.5. This source was chosen as the pulses it produced had the shortest width of the sources characterised. Molecules that had their velocity reduced were therefore easier to distinguish from the background of molecules that did not interact with the decelerator.

As described in the previous section, continuous ablation of a single point led to a reduction in beam intensity. To alleviate this problem the target was rotated from outside the vacuum chamber using a feedthrough. An aluminium dowel was attached to the target and housed in a PEEK tube for frictionless rotation at low temperatures. The PEEK tube was held, by several set screws, in an aluminium block, which was then mechanically attached to the top plate. As the cryogenically cooled components contracted during cooling the inner component of a speedometer cable was used to connect the feedthrough to the aluminium dowel. A speedometer cable is comprised of several copper wires twisted together such that a rotation at one end rotates the other end independent of bends in the cable. A short piece of plastic was also used to provide a thermal disconnect between the dowel on the top plate and the feedthrough at room temperature.

The chamber used in this experiment is different to the one previously described, although the cryocooler and source remain the same. Two differentially pumped chambers were used, one containing the source and the other the decelerator. The two chambers were separated by a 3 mm diameter skimmer located 143 mm above the valve nozzle. Charcoal

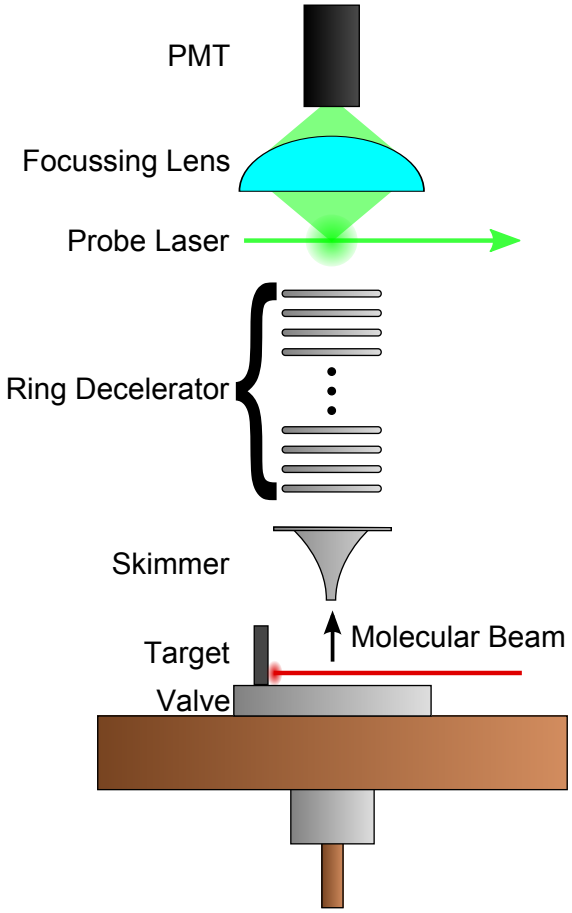

Figure 4.5: Diagram of the experimental apparatus used to produce, decelerate and detect YbF molecules.

sorbs were used in the source chamber to reduce the amount of helium above the valve. When the charcoal sorbs became saturated the pressure in the source chamber could quickly rise and affect the pressure in the decelerator chamber. To reduce the chance of arcing in the decelerator a high pressure trigger would turn off the voltages to the decelerator electrodes once the pressure had risen above 10^{-3} mbar in the source chamber.

Molecules are initially trapped by turning on the electrode voltages as the molecular pulse passes through the first ring of the decelerator. The value of ω is chosen such that the traps initially travel at the same speed as molecules present in the pulse. By gradually decreasing the value of ω whilst the molecules are in the decelerator their forward velocity is reduced. Molecules leaving the decelerator are detected by light induced fluorescence as described in section 2.1.1. The four hyperfine components of the $N = 2$ rotational level, shown in figure 4.6, are partly resolved in the spectrum and we detect the upper two components, $F = 1$ and 2. In high fields half of the M_F substates present in these hyperfine components correlate to $M_N = 0$ and half to $M_N = \pm 1$. Molecules in the $M_N = 0$ state are strongly focussed through the decelerator due to their large Stark shift.

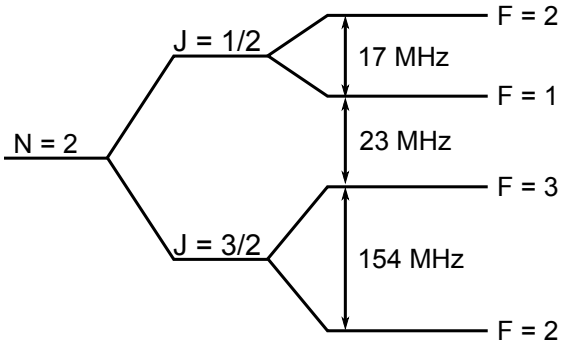

Figure 4.6: Fine and hyperfine splitting of the $N = 2$ rotation level.

4.4 Results

Figure 4.7 shows experimental and simulated time-of-flight traces taken from 47.5 mm above the decelerator exit. The signals have been normalised to the amplitudes of the time-of-flight profiles obtained when the decelerator was off. For the traces shown, a frequency of 25 kHz was applied to the electrodes. Using equation 4.2 this corresponds to a constant trap velocity of $300\,\mathrm{m\,s^{-1}}$ so molecules with a similar velocity will be guided through the decelerator. Molecules that were not guided by the traps are present in the

trace as a Gaussian background signal centred on 2150 ms. Although these molecules were not longitudinally trapped they experienced some radial confinement so the amplitude of the entire pulse is larger than when the decelerator was off. The simulated time-of-flight trace displays all the main features of the experimental trace. The simulated trace was normalised in the same way as the experimental. The difference in overall amplitude between the two traces is due to the fact that the experimental normalisation data was taken at a later time, when the signal was reduced due to target degradation. It was found from simulations of the M_N substates of the $N = 2$ rotational level, that 90% of the molecules detected are in the $M_N = 0$ state and the rest are in the more weakly confined $M_N = \pm 1$ state. The simulated results were reduced by half to correct for the fact that only half of the molecules in the $M_N = 0$ state were detected.

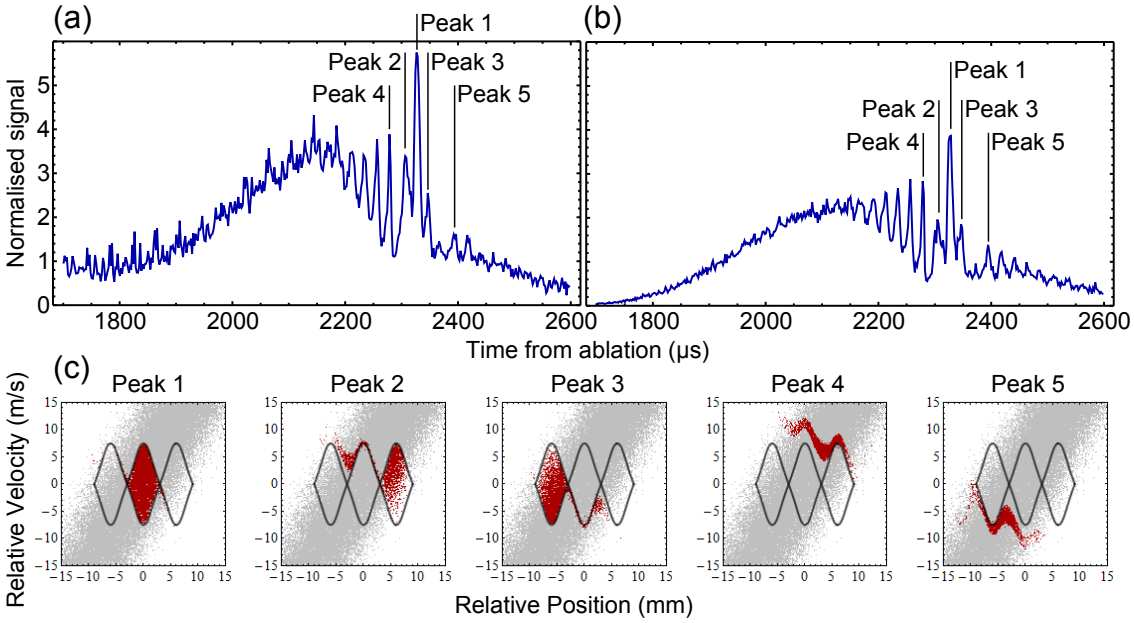

Figure 4.7: (a) Experimental and (b) simulated time-of-flight traces for molecules taken 47.5 mm above the decelerator. (c) Phase space plots of the molecules at the time the trap is fully on. The red points correspond to molecules that form the labelled peaks, the grey points correspond to molecules from the rest of the time-of-flight profile.

Figure 4.7(c) shows a series of plots of the simulated longitudinal velocity and position of the molecular pulse at the time the decelerator has been turned fully on. In these plots, position is relative to the centre of the central trap and velocity is relative to 300 $\mathrm{m\,s^{-1}}$ which is the speed of the travelling traps. Each point in the plot represents one molecule

whose trajectory was simulated. The highlighted molecules are those that create the labelled peaks in the time-of-flight trace. The solid black lines show the maximum velocity the molecules can have whilst remaining trapped, known as the separatrix. These were calculated by considering the difference between the Stark potential at a given position, and the Stark potential at the maximum of the trap. This was equated to kinetic energy to obtain the longitudinal velocity required for a molecule to escape from the trap. An analytical equation for the separatrix was created using the same algorithm used to calculate the Stark potential in the simulation.

Peak 1 is composed of molecules that are travelling at the same speed as the central trap in the decelerator. The peak is large because the molecules are confined both longitudinally and radially and so do not spread out. Due to the longitudinal width of the initial molecular pulse the traps to either side of the central trap also contain molecules. These molecules produce peaks 2 and 3. They are separated from the main plot by $\pm 20\,\mu s$, corresponding to a distance of $\pm 6\,mm$ which is the separation between neighbouring traps. From the phase space plots it can be seen that the central trap is the most densely filled, so this produces the largest peak.

Peak 4 is composed of molecules that lie close to the separatrix in the phase space plots, but are travelling faster than the traps in the decelerator. The molecules experience a force from the decelerator but it is insufficient to fully trap them. Instead their velocity is reduced as they travel across maxima of the trapping field, and increased as they travel across minima. In this way they become bunched at the maxima and appear as a peak in the time-of-flight profile. The same effect produces the other peaks that appear earlier than peak 4. These peaks become gradually smaller as the velocity of the molecules increases and the force they experience from the trapping field affects them less. Peak 5 is composed of molecules that are travelling slower than the traps, but is formed by the same bunching effect that forms peak 4.

By linearly chirping the value of $\omega(\tau)$ a constant decelerating force is applied to the molecules. Figure 4.8 shows the time-of-flight traces taken with various levels of deceleration applied, from an initial speed of $300\,m\,s^{-1}$. The trajectories of molecules through the same decelerating fields were simulated and are shown next to the experimental results. Both experimental and simulated time-of-flight profiles show the trapped molecules appearing at later times as they are decelerated. The largest deceleration applied to the molecules was $14.4 \times 10^3\,m\,s^{-2}$, after which the molecules left the decelerator travelling

at 276 m s^{-1}. This corresponds to an energy reduction of 15%. As the decelerating force is increased the amplitude of the peaks decreases. The decelerating force is equivalent to adding a linear shift to the potential that the molecules see. This has the effect of reducing the potential barrier at the leading edge of each trap, as shown in figure 4.9. This loss of trap depth means that the fraction of molecules that are stably trapped is reduced in the presence of deceleration. This explains why the amplitudes of the decelerated peaks gets smaller as the deceleration increases.

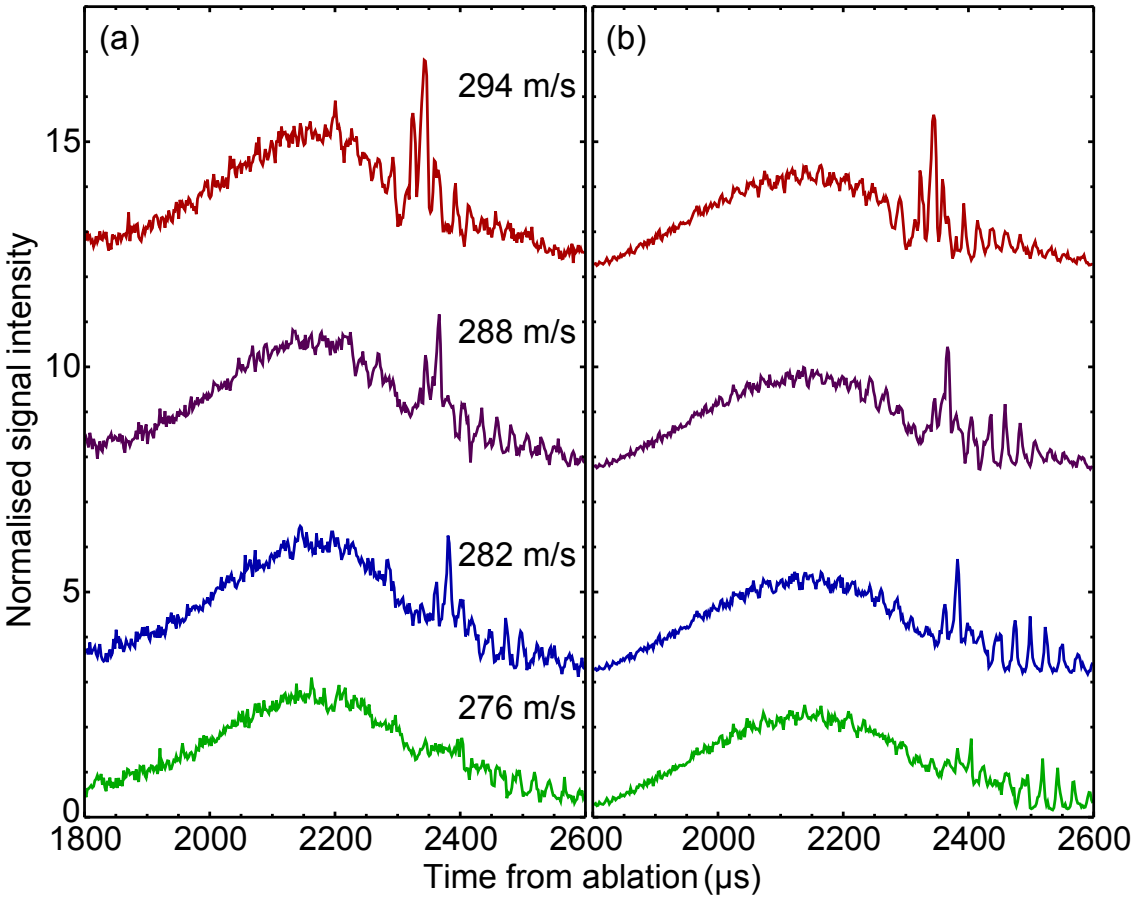

Figure 4.8: Time-of-flight distributions of decelerated YbF molecules, a) measured and b) simulated. Profiles are offset for clarity. The deceleration applied is 3710 m s^{-2} for a final velocity of 294 m s^{-1}, 7350 m s^{-2} for 288 m s^{-1}, 10 900 m s^{-2} for 282 m s^{-1} and 14 400 m s^{-2} for 276 m s^{-1}.

The peaks that are formed from the bunching of untrapped molecules are also affected by the change in the trap potential. As the potential barrier at the leading edge of the traps becomes lower, the molecules travelling faster than the traps experience less bunching

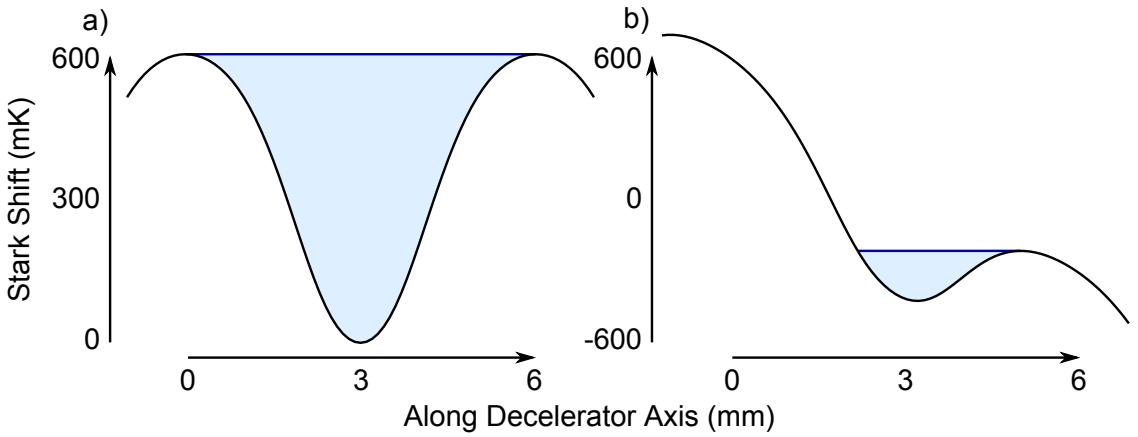

Figure 4.9: The Stark shift experienced by molecules in the (2,0) state in the case of (a) no deceleration and (b) $7400\,\mathrm{m\,s^{-2}}$ deceleration. The blue shaded region indicates the number of molecules that can be trapped.

than those that are travelling slower than the traps. The peaks that appear before the peaks due to the trapped molecules are then suppressed while the peaks that appear later, and are due to molecules that are travelling slower than the traps, are enhanced.

The acceptance of the decelerator is found by simulating a number of molecules uniformly distributed in a cubic phase space volume that is larger than the expected acceptance volume, with a central velocity of $300\,\mathrm{m\,s^{-1}}$. They are decelerated at various rates for 10 ms to find the fraction of molecules that remain in the central trap after this time. The acceptance of the decelerator corresponds to the initial phase space volume multiplied by this fraction. Figure 4.10 shows the acceptance for various levels of deceleration. For a deceleration of $10^4\,\mathrm{m\,s^{-2}}$ the acceptance of the travelling wave decelerator is $4200\,\mathrm{mm^3[m/s]}^3$. This is much greater than the $352\,\mathrm{mm^3[m/s]}^3$ previously reported for the same deceleration using a WF Stark decelerator [95].

The travelling wave decelerator is an improvement over both the weak field and alternating gradient design of decelerator as it offers a greater acceptance and can apply greater levels of deceleration to the molecules at lower electric fields. As the molecules are trapped along the length of the decelerator there are no losses beyond the initial loading. The decelerator can then be extended in length so that the molecules are brought to rest without lowering the acceptance. Using a deceleration of $10^4\,\mathrm{m\,s^{-2}}$, the molecules from this source could be decelerated to rest in 4.5 m. The final stage of the decelerator could then be used as a static electric trap. This is difficult to achieve however as a custom

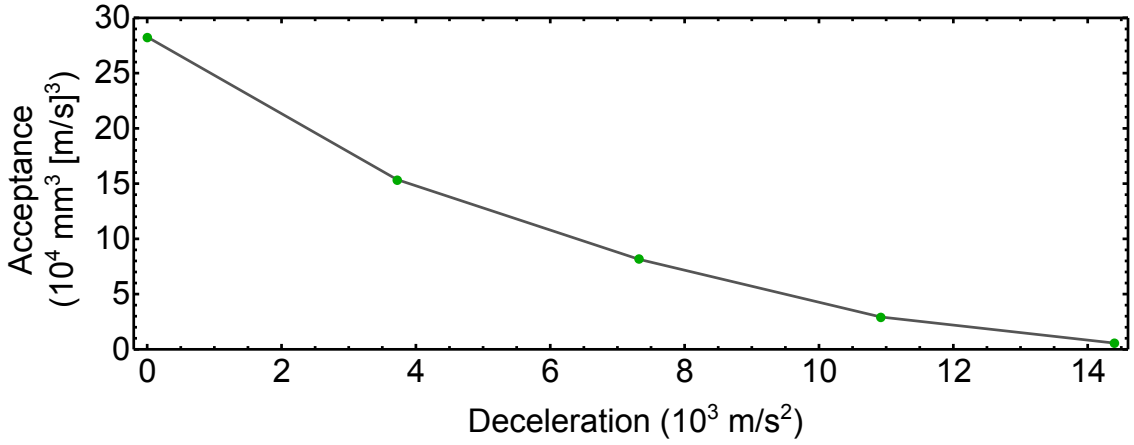

Figure 4.10: Acceptance of the decelerator at various levels of deceleration. The points correspond to the amount of deceleration applied to our molecules

built amplifier is required to amplify the range of frequencies that would be used in such a decelerator.

The length of the decelerator required to bring the molecules to rest could be reduced by using a supersonic source with a thermalisation cell as discussed in chaper 3. Although the longer pulse length and lower forward velocity of this source results in a pulse that is more diffuse at the entrance of the decelerator compared to the supersonic source, the higher beam intensity provides a net gain in the number of molecules that are accepted by the decelerator. The number of molecules that lie inside the separatrix can be compared for the two sources and this shows that, for a deceleration of $10^4\,\mathrm{m\,s^{-2}}$, there will be approximately 5 times as many molecules if a thermalisation cell is used. With this deceleration the molecules can be brought to rest in a 2 m long decelerator.

Chapter 5

Measurement of the Franck-Condon Factors of the $A^2\Pi_{1/2} - X^2\Sigma^+$ transition of YbF

5.1 Introduction

The Franck-Condon principle states that the probability of an electronic transition between two vibrational levels depends on the overlap between the two vibrational wave functions [101]. It is a consequence of the Born-Oppenheimer approximation, that the motion of nuclei happens on a time-scale much longer than electronic transitions. As such the distance between the nuclei in a molecule, r, does not change during an electronic transition. The probability of an electronic transition to a vibrational state is high if there is a high probability of the nuclei separation being r in that state, shown in figure 5.1.

The change in vibrational level in an electronic transition is not governed by selection rules. Instead the probability of each vibrational branch is given by the Franck-Condon factor which is the square of the overlap integral between the vibrational part of the wavefunction for the upper and lower state. It is an important property for laser cooling of molecules as it is a measure of the number of times an electron can be excited before it decays to a different vibrational level to the one it was excited from. Molecules that have a vibrational transition with a large Franck-Condon factor are easier to laser cool as many photons will be scattered on that transition. For example, SrF was calculated to have a Franck-Condon factor of 0.98 on the $X^2\Sigma^+(v'' = 0) \leftarrow A^2\Pi_{1/2}(v' = 0)$ transition

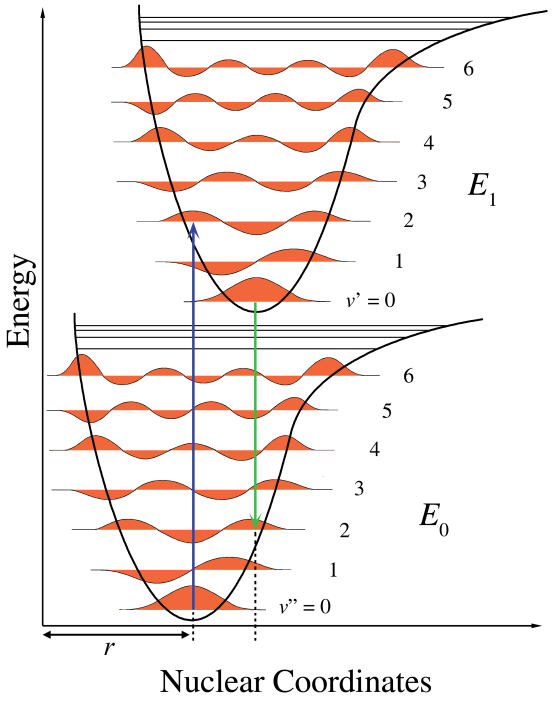

Figure 5.1: Diagram showing preferred transitions in molecules, original image from [102]

[103]. Subsequently a beam of SrF was slowed to $50\,\mathrm{m\,s^{-1}}$ using radiative forces [16]. By measuring the Franck-Condon factors of YbF we can assess its suitability for such slowing. The data presented in this chapter have previously been published in [104].

5.2 Experimental

The chamber and source described in section 3.3 are used to measure the Franck-Condon factors of the $A^2\Pi_{1/2}(v' = 0) - X^2\Sigma^+(v'')$ transition of YbF. A dye laser operating at 552 nm is used to excite molecules to the $A^2\Pi_{1/2}$ $(v' = 0)$ level. They then decay into various vibrational levels of the $X^2\Sigma^+$ state and fluoresce at the corresponding frequency as shown in figure 5.2. These frequencies can be isolated using a range of bandpass filters and the intensity of each transition compared to find the Franck-Condon factors.

The same detection scheme as described in section 2.1.1 was used to measure the fluorescence. As shown in figure 5.3 the collimated fluorescence light leaving the chamber was split into normalisation and signal paths by a 70%/30% beam splitter. The normalisation arm was used to remove any variation in the signal level due to fluctuations in either the molecular or probe beams as described below. It included a 40 nm wide interference

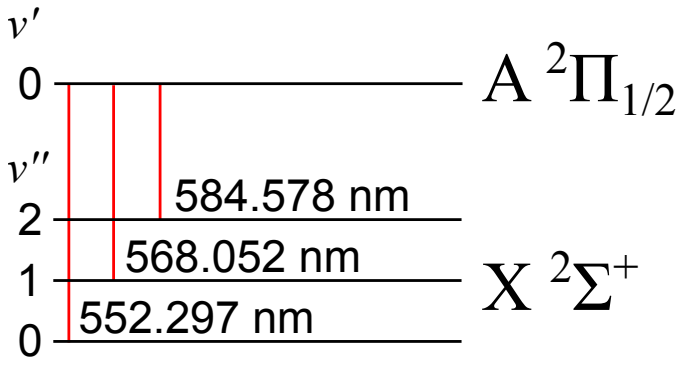

Figure 5.2: The vibrational levels studied in this chapter, showing the wavelength of three transitions. The wavelengths were calculated using the molecular constants from [105].

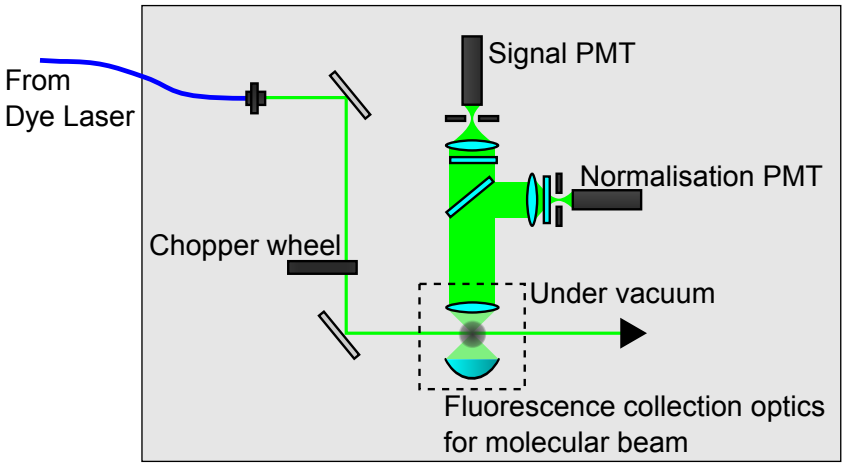

Figure 5.3: Diagram of the experimental set-up for the measurement of the Franck-Condon factor. The target and ablation laser are not shown.

filter to capture fluorescence due to transitions to the first three vibrational levels. In the signal arm the filters used to isolate each transition had a 10 nm wide passband centred on 550 nm, 570 nm and 580 nm. The fluorescence due to transitions to higher vibrational levels was measured using a 590 nm long-pass filter. The manufacturer's transmittance curves for these filters are shown in figure 5.4, along with the wavelengths of the transitions. The filters were used multiple times with different rotational alignment to account for any polarisation dependence. The laser-induced fluorescence transmitted through each filter was measured multiple times with the filters switched in a random order.

When the target was ablated products other than YbF were created and entered the molecular beam. Some particles were in excited states that fluoresced at a similar fre-

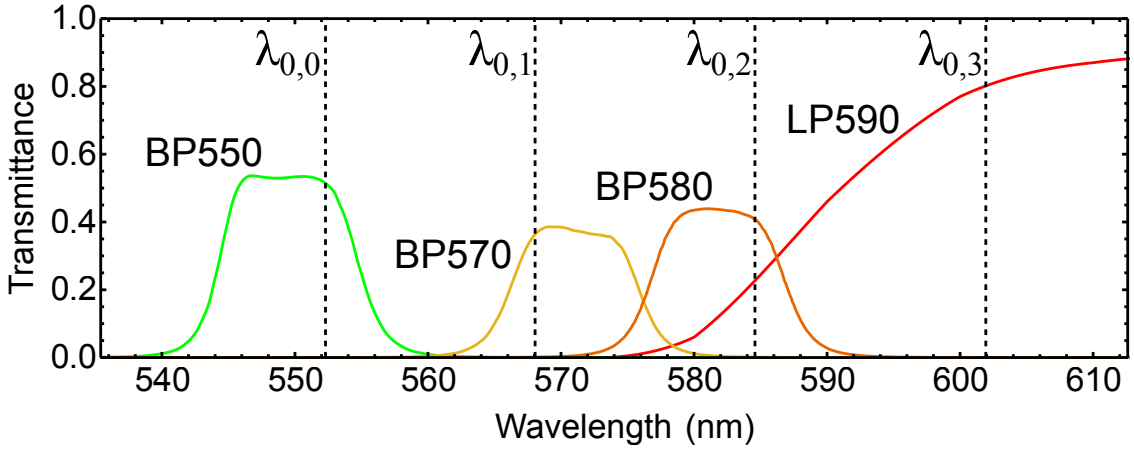

Figure 5.4: Transmission curves as given by the manufacturer for the three 10 nm filters (BP550, BP570 and BP580) and the long pass filter, LP590. The dashed lines indicate the transition wavelengths.

quency to the transitions we were observing, independent of the probe beam. To remove this extraneous light a chopper wheel was placed in the path of the probe beam before it entered the chamber and was synchronised to the Q-switch of the ablation laser. On every second shot a time-of-flight trace was taken of the additional fluorescence along with any light from the ablation laser which remained after the filter. Both these additions could then be removed, along with any background light due to room lights and laser scatter.

The ratio, R^i, between the signal from the normalisation and signal arms for a filter i can be described with the following equation,

$$R^i = \frac{I_{\text{signal}}}{I_{\text{norm}}} = \frac{\zeta}{I_{\text{norm}}} \left(f_{0,0}\ B_0\ T_0^i\ \varepsilon_0\ + f_{0,1}\ B_1\ T_1^i\ \varepsilon_1\ + \cdots\right), \tag{5.1}$$

where ζ is the total number of photons emitted by the molecules and collimated by the collection optics, I_{norm} is the intensity of the normalization arm, $f_{0,x}$ is the Franck-Condon factor for a transition to the vibrational level x, B_x is the transmittance of the beam splitter, T_x^i is the transmittance of filter i and ε_x is the efficiency of the detector, all at the wavelength of the transition to the vibrational level x. The factor ζ/I_{norm} is a constant as the normalisation arm is not changed during the experiment. The values of T^i for the four different filters are measured at each of the relevant wavelengths and these values, combined with the fact that the sum of all the Franck-Condon factors is 1, allows $f_{0,0}$, $f_{0,1}$ and $f_{0,2}$ to be determined once B_x, T_x^i, and ε_x are known.

As the majority of the fluorescence is at $\lambda_{0,0}$ and $\lambda_{0,1}$ the transmittances of the beam

splitter and filters were accurately measured at these wavelengths. A Coherent 899 ring dye laser pumped by a Spectra Physics BeamLok 2080-15S argon-ion laser was used with Rhodamine 560 dye to produce light at these wavelengths. To account for changes in the laser power over time two photo-diodes were set up to collect the transmitted and reflected laser light from the beam splitter. The photo-diodes were swapped to remove any effect from the variation in their efficiencies and the two ratios multiplied to get the square of the true ratio. This could then be used to calculate the transmittance of the beam splitter using the equation $B_x = R_x^B/(1 + R_x^B)$, where R_x^B is the ratio of transmitted to reflected light at the wavelength x. The transmittance of each filter was found by placing it in the path of the transmitted beam. When the filters were rotated it was found that they had a polarisation dependence which altered the transmission by 0.1%. The ratio of transmitted light to reflected light with and without the filter was compared to obtain the transmittance of the filter. The transmittances measured were in good agreement with the transmission curves supplied by the manufacturer. The efficiency of the PMT was taken from the manufacture's datasheet as shown in figure 5.5.

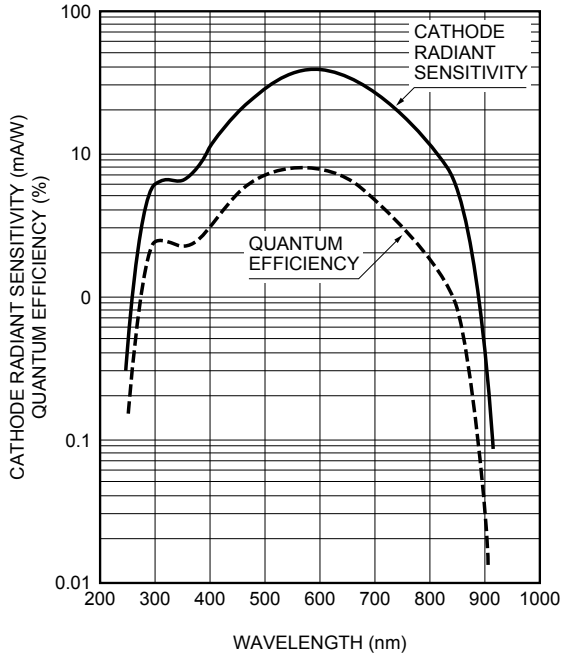

Figure 5.5: Change in quantum efficiency and cathode radiant sensitivity with frequency for a Hamamatsu R2228 PMT [106].

5.3 Results

Typical time of flight traces are shown in figure 5.6 for two different filters. Each has been averaged over 100 shots and any constant light background has been removed. Each plot includes the time of flight trace taken with the probe laser on and off and an inset which shows the difference between the two. At early times a fast decay is present which is due to light from the ablation laser. This decay and the light due to extraneous fluorescing particles have a larger effect on the trace taken with the 580 nm filter than with the 550 nm filter as fewer molecules fluoresce at this wavelength. When the light that is not due to molecules fluorescing is removed the time of flight profile has a similar shape to the profile taken with the 550 nm filter.

Once the fluorescence due to YbF molecules has been recovered the signal is integrated from 120 µs to 600 µs. The ratios between the normalisation and signal arms for each filter are used in equation 5.1 to obtain the Franck-Condon factors, shown in table 5.1. The dominant error in the calculation comes from the uncertainty in the PMT efficiency. An error of 5% was used as this was the level of accuracy with which the value could be read from the manufacture's datasheet.

$f_{0,x}$	IC	ASU[1]	ASU[2]	Calculated
$f_{0,0}$	0.928 ± 0.005	0.927 ± 0.010	0.937 ± 0.004	0.915
$f_{0,1}$	0.069 ± 0.005	0.073 ± 0.010	0.063 ± 0.004	0.083
$f_{0,2}$	$(3.0 \pm 0.5) \times 10^{-3}$	$< 5 \times 10^{-3}$	$< 5 \times 10^{-3}$	2.7×10^{-3}
$\sum_{n>2} f_{0,n}$	$(0.0 \pm 0.5) \times 10^{-3}$			

Table 5.1: Franck Condon factors of YbF measured at Imperial College (IC) and Arizona State University (ASU).

This experiment was performed in collaboration with the Arizona State University where a second set of measurements were performed and calculations of the Franck Condon factors of YbF undertaken. Their results are also shown in table 5.1. The relative intensities of the electronic transitions to different vibrational levels were obtained with a scanning monochromator, which was used to measure the laser induced fluorescence due to excitation of the R(2) branch feature (ASU[1]) and near the $P_1 + Q_{12}$ band head (ASU[2]). The calculation of the Frank Condon factors was performed with the suite of programs developed by Prof. Robert LeRoy (Waterloo University) [107]. More information on the

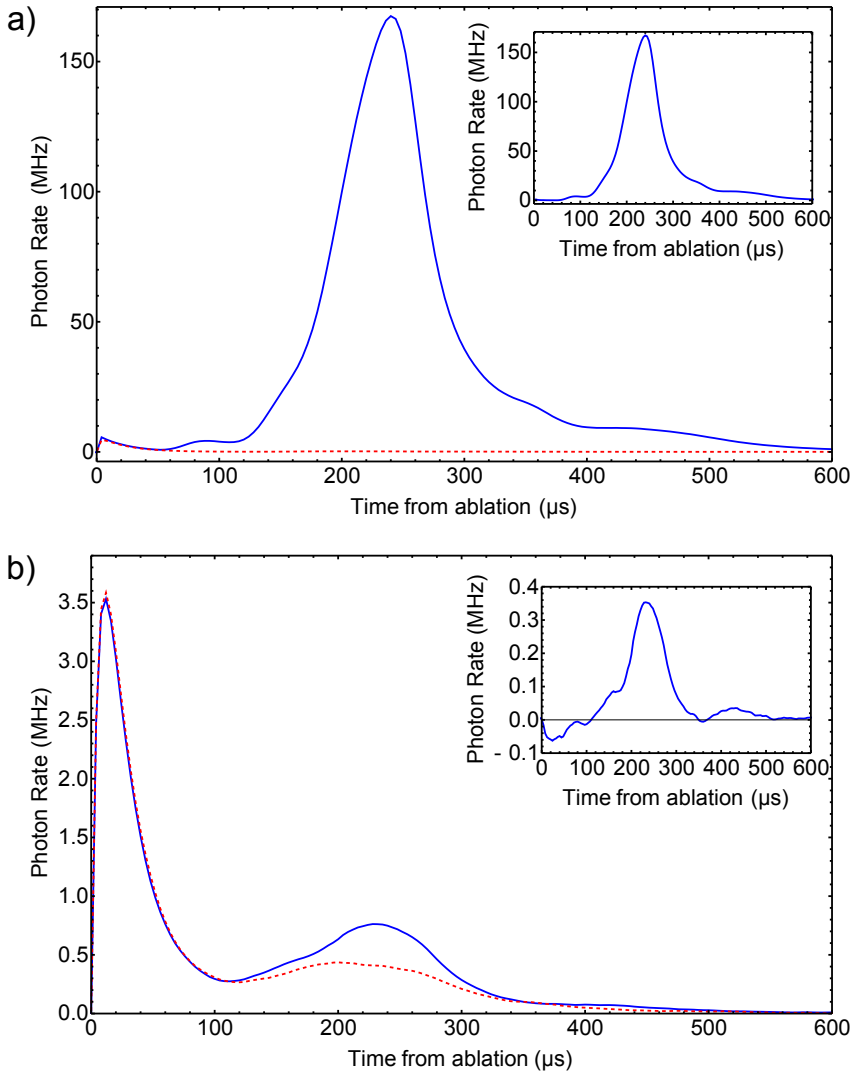

Figure 5.6: Time of flight traces for the a) 550 nm and b) 580 nm filters. Traces are shown for when the probe laser is on (solid line) and off (dashed line). The extraneous light has a larger impact when the 580 nm filter is used as the laser-induced fluorescence rate at this wavelength is low. The inset in each figure shows the time of flight trace with all light not due to fluorescing YbF removed. The negative fluorescence rate at early times is due to shot-to-shot noise in the ablation pulse that is not averaged out. The gate window chosen does not include these early times.

work done at Arizona State University can be found in ref [104].

5.4 Discussion

Knowing the Franck-Condon factors of YbF allows us to assess its suitability for laser cooling. For laser cooling, a transition where an electron can be excited to a higher state then decay to the same state it was excited from is most attractive. In this way an unlimited number of photons can be scattered by addressing a single transition. In cases where this is not possible, such as with molecules, multiple lasers must be used. The frequency of these lasers must be such that molecules that decay to a different state are repumped back into the cooling cycle. When using two such repumping lasers to address the first and second vibrational levels in the electronic ground state of YbF the maximum probability of a YbF molecule decaying to a dark state is 5×10^{-4}. This results in a YbF molecule scattering an average of 2000 photons before entering a dark state.

When Doppler cooling it is possible, with appropriate frequency detuning, for each scattered photon to average a net reduction in momentum of h/λ. This corresponds to a velocity change of

$$\Delta v = \frac{h}{M\lambda}, \tag{5.2}$$

where M is the molecular mass of YbF. When cooling on the $v' = 0 \leftarrow v'' = 0$ transition in YbF this equals $4 \times 10^{-3}\,\mathrm{m\,s^{-1}}$. As the average number of photons scattered by the YbF molecules is 2000, the average velocity reduction will be $8\,\mathrm{m\,s^{-1}}$ before the molecule enters a dark state. For the sources currently available this makes the laser cooling scheme more suited to transverse cooling of a molecular beam than to slowing of the centre of mass velocity. Laser cooling of YbF from an effusive cryogenic source is discussed in reference [108].

Our results agree well with the measured and calculated results from the Arizona State University, given the typical uncertainty associated with calculations of this kind.

Chapter 6

Conclusion and Outlook

6.1 Conclusion

In this thesis three different methods were explored for producing a molecular beam from a cryogenic source. The aim was to create a source that would increase the sensitivity of precision measurements such as the measurement of the electron EDM. For this measurement the sensitivity depends on the interaction time between the molecules and electric and magnetic fields, and the square root of the molecule flux so an ideal beam will have a high intensity and a low velocity. It is also important to maximise the number of molecules in their rotational ground state, as this is the state used for the EDM measurement, and the duty cycle of the source.

It was found that the slowest beam velocity could be obtained using a buffer gas source with a low flow rate of helium though the cell. Beam velocities as low as $65\,\mathrm{m\,s^{-1}}$ were recorded for a flow rate of 1 SCCM. At this flow rate the helium in the cell is in the free molecular regime and the extraction efficiency of the cell is 0.03%. For the EDM measurement, and to better compare this buffer gas source to the other sources tested, it is useful to estimate the number of ground state YbF molecules per steradian per pulse that would be produced in a buffer gas source. The total number of YbF produced when a ceramic target was ablated in a similarly shaped cell was 3×10^{13} molecules [76]. With the temperature and divergence of our beam the expected number of YbF molecules in the beam in the ground state will be 4×10^{9} molecules per steradian per pulse. The beam produced from a buffer gas source with a low flow of helium is slower than the source currently in use in the EDM experiment by a factor 10 [70], and 4 time more intense than a room temperature supersonic source of YbF [93].

Increasing the flow of helium through the cell to 60 SCCM increased the velocity of the beam as the gas began to expand supersonically from the aperture. The upper limit to the velocity was $204\,\mathrm{m\,s^{-1}}$ which corresponds to the supersonic velocity of helium at 4 K. The extraction efficiency also increased with increasing helium flow, while the divergence decreased. This results in a more intense molecular beam calculated to be 3×10^{12} molecules per steradian per pulse. Although the velocity of the beam has increased by a factor 3, the intensity has increased by a factor 750 so the sensitivity of a measurement is increased by a factor 9 over using a low flow of helium through the cell. This makes the high flow beam a better choice for precision measurements.

From this simple analysis of the beam parameters it appears that a buffer gas source is a much improved method for producing a beam for precision measurements, however there are a number of issues which make a buffer gas source less attractive for this purpose. The first is that the molecular pulse can be up to 50 ms long as it leaves the aperture. The number density will then be much lower for applications in which only hundreds of microseconds of the pulse can be used, such as in the current EDM measurement method. The second is the fact that a static target is used so the signal quickly drops off as the same spot is ablated. The position of the ablation laser on the target can be moved, however this can often decrease the signal further as the molecules are formed in a part of the cell where the helium is not travelling towards the aperture. The continuous flow of helium also limits the length of time the experiment can be run as the charcoal sorbs can only absorb a certain volume of helium before becoming saturated. Once they are saturated the flow of helium must be stopped for $\sim$30 minutes before the experiment can be run again. This decreases the duty cycle of the source.

The need for charcoal sorbs is removed if neon is used as a buffer gas instead of helium. As neon has a higher boiling point than helium any 4 K surface will act as a cryopump, greatly increasing the surface area that can absorb the buffer gas outside the cell. The cell can be held at a temperature above the boiling point of neon by decreasing the thermal conductivity between the cell and the cold plate of the cryocooler. Heaters positioned on the cell can then be used to set the temperature of the cell. For the number density in the cell to be high enough that the gas is hydrodynamic the temperature must be above 12 K. At this temperature the supersonic velocity of neon is $160\,\mathrm{m\,s^{-1}}$ so a slower molecular beam is also expected.

Shorter molecular pulses were obtained by using a pulsed valve to create a supersonic

jet of helium. When the ceramic target was ablated directly into this jet the lowest velocity recorded for the molecular beam was $367\,\mathrm{m\,s^{-1}}$. This is much higher than the supersonic velocity of helium at 4 K and is due to heating of the helium as it travels through the valve. By modifying the valve such that the helium spends less time in contact with the hottest part of the valve the velocity was reduced to $315\,\mathrm{m\,s^{-1}}$. Neon was also used as a carrier gas and the lowest velocity measured was $330\,\mathrm{m\,s^{-1}}$ when the base temperature of the valve was 24.5 K. The highest beam intensity measured was 5×10^9 molecules per steradian per pulse. This is lower than the intensity expected from a buffer gas source with a high flow of helium, however these molecules are in a pulse with a FWHM of $\sim$100 µs at a distance of 50 mm from the valve nozzle. This makes this source more useful for applications which require a short pulse of molecules, such as trapping and decelerating.

A second pulsed source was characterised in which the helium entered a thermalisation chamber through a pipe which was angled upwards and towards the ceramic target. This is similar to the source used by Milani *et al* [58], however the exit of the chamber was left open to avoid the creation of clusters. As the helium travelled through a cooled copper pipe before expanding the velocity of the beam is lower than when it expands directly from the nozzle of the valve. The measured beam velocity is $206\,\mathrm{m\,s^{-1}}$ as expected for a supersonic expansion of helium at 4 K. The intensity of the beam is 4.5×10^{10} molecules per steradian per pulse with a FWHM of $\sim$200 µs. The beam intensity has increased with the inclusion of a thermalisation chamber as there is a higher density of helium in the chamber and the ablation plume is constrained. There is then a greater probability that molecules with a high energy will be cooled and entrained in the helium jet.

6.2 Outlook

Using what was learned from these sources, a new source has now been designed that aims to solve the problems associated with a buffer gas source. It is based on the pulsed source with a thermalisation chamber and is shown in figure 6.1. The main chamber of the source is a 10 mm diameter cylinder with an angled base and open top. The helium enters the cell through a tube that is at the same angle as the base. The edge of the base is curved so the helium will travel up a wall and form a fast flow region across the target. When the target is ablated the YbF is constrained to an area where it will be quickly swept out

the cell.

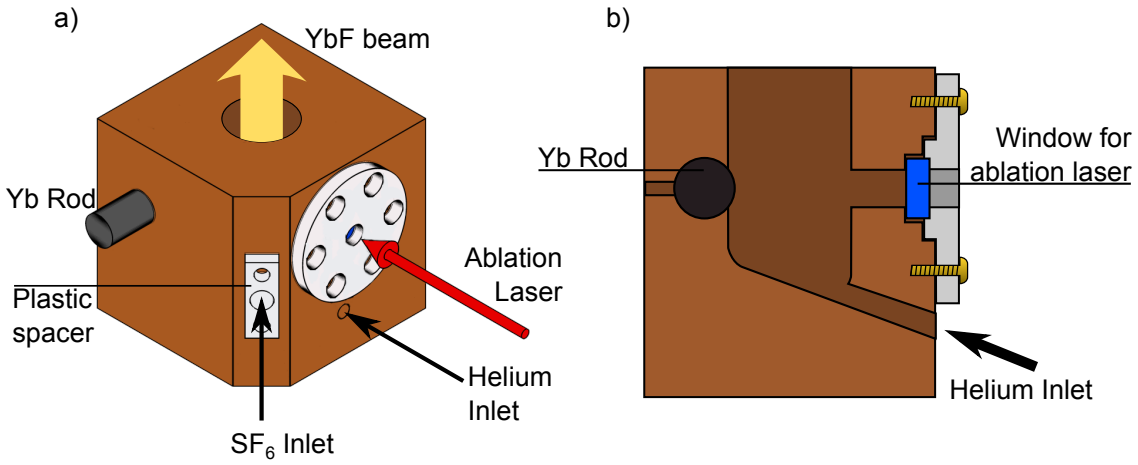

Figure 6.1: a) Isometric and b) cross-sectional view of the open buffer gas cell design.

The YbF molecules are created by ablating a Yb rod into a mixture of helium and SF_6. The Yb is in rod form so that it can be rotated and moved into and out of the cell. This increases the surface area that can be ablated and reduces the loss of signal that occurs when a single point is ablated multiple times. The SF_6 enters the cell separately from the helium. The boiling point of SF_6 is 206 K which is much higher than the temperature of the cell. To avoid the SF_6 from freezing in the fill line it is thermally disconnected from the cell using a polyetherimide insulating jacket. A heater is attached to the fill line so it can be heated in the event of SF_6 freezing in the fill line.

The helium flow through this source has been simulated in the case of a continuous flow of 60 SCCM through the cell with a 30% mesh at the exit to maintain a sufficiently high pressure in the thermalisation chamber. The source could also be used with a pulsed valve providing the helium in short, high pressure pulses. The simulated flow of helium is shown in figure 6.2. As expected there is a high helium velocity next to the target which will quickly sweep the YbF out the cell. There is also a recirculation region further from the target however the YbF molecules will be swept out the cell before they can expand into this region.

An initial YbF plume consisting of a 5 mm radius sphere offset from the centre by 2.5 mm towards the target rod was simulated and the extraction efficiency was found to be 63%. This is higher than both the measured and simulated extraction efficiencies of the buffer gas cell. The beam is expected to have a small divergence of 10° as the molecules will experience a large number of collisions inside the cell, which will

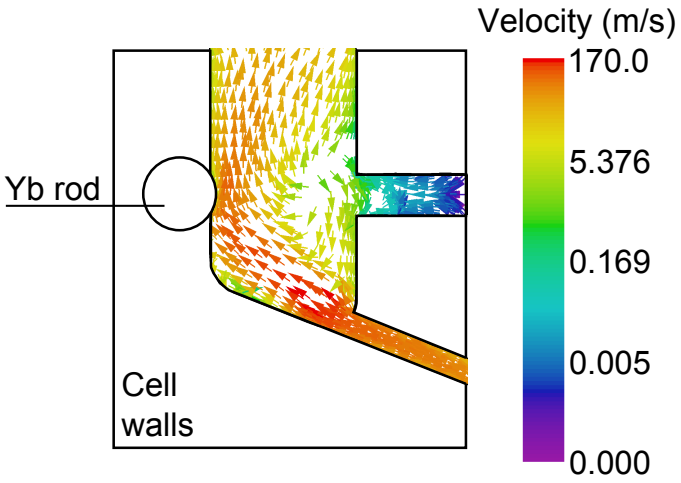

Figure 6.2: Helium flow through the cell with a flow rate of 60 SCCM and a 30% mesh across the exit. The arrows indicate the direction of flow and the colour is the velocity magnitude on a log scale.

collimate the beam, and few outside the cell. Assuming the same amount of YbF is formed in the new source as in the buffer gas cell the molecular beam intensity will be 2×10^{13} molecular per steradain per pulse. The simulation predicts a beam velocity of $120\,\mathrm{m\,s^{-1}}$ and a FWHM for the molecular pulse of 340 µs. With this source we will be able to produce a beam that is both slower and more intense than the current source used in the EDM experiment, and that has a short enough pulse length that the majority of the molecules can be used.

To further improve the sensitivity of the EDM measurement the YbF molecules can be trapped in an optical molasses then used to create a molecular fountain. A scheme for performing this is set out in [108]. To create the initial beam of YbF a buffer gas cell is used with a high flow of helium so a large fraction of YbF is swept out the aperture. After the molecules leave this cell they enter a second cell with a large, mesh covered aperture that reflects some of the helium from the first cell. The reflected helium will collide with the YbF and reduce the forward velocity of the beam [69]. A curved magnetic guide is positioned in front of the second cell to steer the YbF molecules away from the residual helium beam. The guide also removes the fastest molecules and molecules that are too hot to be radially confined leaving a slow, cold beam that is suitable for laser cooling. Using the Franck-Condon measurements presented in this thesis the branching ratios of the vibrational states can be calculated and used to model the motion of the molecules

in a 6 beam optical molasses. It was found that 5.9×10^6 molecules are trapped in the optical molasses after 100 ms, assuming 1×10^{13} are created in the buffer gas cell. Once the molecules have been accumulated in the trap they can be forced upwards by detuning the vertical lasers to create a molecular fountain.

Bibliography

[1] Chu, S., Kasevich, M., Moler, K., Riis, E., and Weiss, D. In *Precision Electromagnetic Measurements, 1990. CPEM '90 Digest., Conference on*, 5–6, (1990).

[2] Essen, L. and Parry, J. V. L. *Nature* **176**, 280–282 August (1955).

[3] Bouchendira, R., Cladé, P., Guellati-Khélifa, S., Nez, F., and Biraben, F. *Physical Review Letters* **106**(8), 080801 February (2011).

[4] Parthey, C. G., Matveev, A., Alnis, J., Pohl, R., Udem, T., Jentschura, U. D., Kolachevsky, N., and Hänsch, T. W. *Physical Review Letters* **104**(23), 233001 June (2010).

[5] Mohr, P. J., Taylor, B. N., and Newell, D. B. *Journal of Physical and Chemical Reference Data* **41**(4), 043109 December (2012).

[6] Darquie, B., Stoeffler, C., Shelkovnikov, A., Daussy, C., Amy-Klein, A., Chardonnet, C., Zrig, S., Guy, L., Crassous, J., Soulard, P., Asselin, P., Huet, T. R., Schwerdtfeger, P., Bast, R., and Saue, T. *Chirality* **22**(10), 870–884 (2010).

[7] Santos, L., Shlyapnikov, G. V., Zoller, P., and Lewenstein, M. *Physical Review Letters* **85**, 1791–1794 August (2000).

[8] Hudson, J. J., Sauer, B. E., Tarbutt, M. R., and Hinds, E. A. *Physical Review Letters* **89**(2), 023003 June (2002).

[9] Hudson, J. J., Kara, D. M., Smallman, I. J., Sauer, B. E., Tarbutt, M. R., and Hinds, E. A. *Nature* **473**, 493–496 May (2011).

[10] Vutha, A. C., Campbell, W. C., Gurevich, Y. V., Hutzler, N. R., Parsons, M., Patterson, D., Petrik, E., Spaun, B., Doyle, J. M., Gabrielse, G., and DeMille, D. *Journal of Physics B Atomic Molecular Physics* **43**(7), 074007 April (2010).

[11] Krems, R. V. *Physical Chemistry Chemical Physics (Incorporating Faraday Transactions)* **10**, 4079 (2008).

[12] Hudson, E. R., Ticknor, C., Sawyer, B. C., Taatjes, C. A., Lewandowski, H. J., Bochinski, J. R., Bohn, J. L., and Ye, J. *Physical Review A: Atomic, Molecular, and Optical Physics* **73**(6), 063404 June (2006).

[13] DeMille, D., Glenn, D. R., and Petricka, J. *European Physical Journal D* **31**, 375–384 November (2004).

[14] van Veldhoven, J., Bethlem, H. L., and Meijer, G. *Physical Review Letters* **94**(8), 083001 March (2005).

[15] DeMille, D. *Physical Review Letters* **88**(6), 067901 February (2002).

[16] Barry, J. F., Shuman, E. S., Norrgard, E. B., and DeMille, D. *Physical Review Letters* **108**(10), 103002 March (2012).

[17] Hummon, M. T., Yeo, M., Stuhl, B. K., Collopy, A. L., Xia, Y., and Ye, J. *Physical Review Letters* **110**(14), 143001 April (2013).

[18] Zhelyazkova, V., Cournol, A., Wall, T. E., Matsushima, A., Hudson, J. J., Hinds, E. A., Tarbutt, M. R., and Sauer, B. E. *ArXiv e-prints* August (2013).

[19] Vanhaecke, N., de Souza Melo, W., Laburthe Tolra, B., Comparat, D., and Pillet, P. *Physical Review Letters* **89**(6), 063001 July (2002).

[20] Jones, K. M., Tiesinga, E., Lett, P. D., and Julienne, P. S. *Reviews of Modern Physics* **78**, 483–535 April (2006).

[21] Köhler, T., Góral, K., and Julienne, P. S. *Reviews of Modern Physics* **78**, 1311–1361 October (2006).

[22] Sage, J. M., Sainis, S., Bergeman, T., and DeMille, D. *Physical Review Letters* **94**(20), 203001 May (2005).

[23] Ospelkaus, S., Pe'Er, A., Ni, K.-K., Zirbel, J. J., Neyenhuis, B., Kotochigova, S., Julienne, P. S., Ye, J., and Jin, D. S. *Nature Physics* **4**, 622 August (2008).

[24] Greiner, M., Regal, C. A., and Jin, D. S. *Nature* **426**, 537–540 December (2003).

[25] Ostendorf, A., Zhang, C. B., Wilson, M. A., Offenberg, D., Roth, B., and Schiller, S. *Physical Review Letters* **97**(24), 243005 December (2006).

[26] Wallis, A. O. G. and Hutson, J. M. *Physical Review Letters* **103**(18), 183201 October (2009).

[27] Tokunaga, S. K., Skomorowski, W., Żuchowski, P. S., Moszynski, R., Hutson, J. M., Hinds, E. A., and Tarbutt, M. R. *European Physical Journal D* **65**, 141–149 November (2011).

[28] Weinstein, J. D., DeCarvalho, R., Guillet, T., Friedrich, B., and Doyle, J. M. *Nature* **395**, 148–150 September (1998).

[29] DeCarvalho, R., Doyle, J. M., Friedrich, B., Guillet, T., Kim, J., Patterson, D., and Weinstein, J. D. *European Physical Journal D* **7**, 289–309 October (1999).

[30] Ramsey, N. *Molecular Beams*, volume 1. Oxford University Press, Oxford, England, (1986).

[31] Ghaffari, B., Gerton, J. M., McAlexander, W. I., Strecker, K. E., Homan, D. M., and Hulet, R. G. *Physical Review A: Atomic, Molecular, and Optical Physics* **60**, 3878–3881 November (1999).

[32] Rangwala, S. A., Junglen, T., Rieger, T., Pinkse, P. W., and Rempe, G. *Physical Review A: Atomic, Molecular, and Optical Physics* **67**(4), 043406 April (2003).

[33] Hogan, S. D., Motsch, M., and Merkt, F. *Physical Chemistry Chemical Physics (Incorporating Faraday Transactions)* **13**, 18705 (2011).

[34] Bethlem, H. L., Berden, G., and Meijer, G. *Physical Review Letters* **83**, 1558–1561 August (1999).

[35] Scharfenberg, L., Haak, H., Meijer, G., and van de Meerakker, S. Y. T. *Physical Review A: Atomic, Molecular, and Optical Physics* **79**(2), 023410 February (2009).

[36] Bethlem, H. L., van Roij, A. J., Jongma, R. T., and Meijer, G. *Physical Review Letters* **88**(13), 133003 April (2002).

[37] Wall, T. E., Kanem, J. F., Dyne, J. M., Hudson, J. J., Sauer, B. E., Hinds, E. A., and Tarbutt, M. R. *Physical Chemistry Chemical Physics (Incorporating Faraday Transactions)* **13**, 18991 (2011).

[38] Procter, S. *Chemical Physics Letters* **374**, 667–675 June (2003).

[39] Osterwalder, A., Meek, S. A., Hammer, G., Haak, H., and Meijer, G. *Physical Review A: Atomic, Molecular, and Optical Physics* **81**(5), 051401 May (2010).

[40] Lavert-Ofir, E., Gersten, S., Henson, A. B., Shani, I., David, L., Narevicius, J., and Narevicius, E. *New Journal of Physics* **13**(10), 103030 October (2011).

[41] Quintero-Pérez, M., Jansen, P., Wall, T. E., van den Berg, J. E., Hoekstra, S., and Bethlem, H. L. *Physical Review Letters* **110**(13), 133003 March (2013).

[42] Trottier, A., Carty, D., and Wrede, E. *Molecular Physics* **109**(5), 725–733 (2011).

[43] Elioff, M. S., Valentini, J. J., and Chandler, D. W. *Science* **302**, 1940–1943 December (2003).

[44] Fulton, R., Bishop, A. I., Shneider, M. N., and Barker, P. F. *Nature Physics* **2**, 465–468 July (2006).

[45] Levy, D. H. *Annual Review of Physical Chemistry* **31**, 197–225 October (1980).

[46] Hopkins, J. B., Langridge-Smith, P. R. R., Morse, M. D., and Smalley, R. E. *The Journal of Chemical Physics* **78**, 1627–1637 February (1983).

[47] Smalley, R. E., Wharton, L., and Levy, D. H. *Accounts of Chemical Research* **10**(4), 139–145 (1977).

[48] Smalley, R. E., Wharton, L., and Levy, D. H. *The Journal of Chemical Physics* **63**, 4977–4989 December (1975).

[49] Liverman, M. G., Beck, S. M., Monts, D. L., and Smalley, R. E. *The Journal of Chemical Physics* **70**, 192–198 January (1979).

[50] Gentry, W. R. and Giese, C. F. *Review of Scientific Instruments* **49**, 595–600 May (1978).

[51] Auerbach, A. and McDiarmid, R. *Review of Scientific Instruments* **51**, 1273–1275 September (1980).

[52] Proch, D. and Trickl, T. *Review of Scientific Instruments* **60**, 713–716 April (1989).

[53] Otis, C. E. and Johnson, P. M. *Review of Scientific Instruments* **51**, 1128–1129 August (1980).

[54] Miller, T. A. *Science* **223**(4636), pp. 545–553 (1984).

[55] Monts, D., Dietz, T. G., Duncan, M. A., and Smalley, R. E. *Chemical Physics* **45**, 133–139 January (1980).

[56] Powers, D. E., Hansen, S. G., Geusic, M. E., Puiu, A. C., Hopkins, J. B., Dietz, T. G., Duncan, M. A., Langridge-Smith, P. R. R., and Smalley, R. E. *The Journal of Physical Chemistry* **86**(14), 2556–2560 July (1982).

[57] Neal, C. M., Breaux, G. A., Cao, B., Starace, A. K., and Jarrold, M. F. *Review of Scientific Instruments* **78**(7), 075108 July (2007).

[58] Milani, P. and Deheer, W. A. *Review of Scientific Instruments* **61**, 1835–1838 July (1990).

[59] Billas, I. M. L., Châtelain, A., and de Heer, W. A. *Journal of Magnetism and Magnetic Materials* **168**, 64–84 April (1997).

[60] Shirley, J., Scurlock, C., Steimle, T., Simard, B., Vasseur, M., and Hackett, P. A. *The Journal of Chemical Physics* **93**, 8580–8585 December (1990).

[61] Whitham, C. J., Soep, B., Visticot, J.-P., and Keller, A. *The Journal of Chemical Physics* **93**, 991–1000 July (1990).

[62] Fletcher, D. A., Jung, K. Y., Scurlock, C. T., and Steimle, T. C. *The Journal of Chemical Physics* **98**, 1837–1842 February (1993).

[63] Maxwell, S. E., Brahms, N., DeCarvalho, R., Glenn, D. R., Helton, J. S., Nguyen, S. V., Patterson, D., Petricka, J., DeMille, D., and Doyle, J. M. *Physical Review Letters* **95**(17), 173201 October (2005).

[64] Patterson, D. and Doyle, J. M. *Journal of Chemical Physics* **126**(15), 154307 April (2007).

[65] Wu, T., Wang, X., Lu, H., and Lu, P. *Journal of Physics D Applied Physics* **45**, 5203 November (2012).

[66] Hutzler, N. R., Parsons, M. F., Gurevich, Y. V., Hess, P. W., Petrik, E., Spaun, B., Vutha, A. C., DeMille, D., Gabrielse, G., and Doyle, J. M. *Physical Chemistry Chemical Physics (Incorporating Faraday Transactions)* **13**, 18976 (2011).

[67] Patterson, D., Rasmussen, J., and Doyle, J. M. *New Journal of Physics* **11**(5), 055018 May (2009).

[68] Barry, J. F., Shuman, E. S., and DeMille, D. *Physical Chemistry Chemical Physics* **13**, 18936 (2011).

[69] Lu, H. I., Rasmussen, J., Wright, M. J., Patterson, D., and Doyle, J. M. *Physical Chemistry Chemical Physics (Incorporating Faraday Transactions)* **13**, 18986 (2011).

[70] Smallman, I. J. *A New Measurement of the Electron Electric Dipole Moment Using Ytterbium Fluoride.* PhD thesis, Imperial College London, (2013).

[71] Sedgley, D. W. and Tobin, A. G. Technical report, Department of Energy, (1984).

[72] Pauly, H. *Atom, Molecule, and Cluster Beams I.* Springer, (2000).

[73] Hasted, J. B. *Physics of Atomic Collisions.* London Butterworths, second edition, (1972).

[74] Egorov, D., Lahaye, T., Schöllkopf, W., Friedrich, B., and Doyle, J. M. *Physical Review A: Atomic, Molecular, and Optical Physics* **66**(4), 043401 October (2002).

[75] Chapman, S. *Royal Society of London Proceedings Series A* **93**, 1–20 December (1916).

[76] Skoff, S. M., Hendricks, R. J., Sinclair, C. D. J., Hudson, J. J., Segal, D. M., Sauer, B. E., Hinds, E. A., and Tarbutt, M. R. *Physical Review A: Atomic, Molecular, and Optical Physics* **83**(2), 023418 February (2011).

[77] Skoff, S. M. *Buffer gas cooling of YbF molecules.* PhD thesis, Imperial College London, (2011).

[78] Rott, N. *Annual Review of Fluid Mechanics* **22**, 1–11 (1990).

[79] Peng, D.-Y. and Robinson, D. B. *Industrial & Engineering Chemistry Fundamentals* **15**(1), 59–64 (1976).

[80] http://trc.nist.gov/.

[81] Nacher, P. J. *Journal of Chemical Physics* **101**, 6367–6368 October (1994).

[82] Bich, E., Hellmann, R., and Vogel, E. *Molecular Physics* **105**, 3035–3049 December (2007).

[83] Sazhin, O. *Soviet Journal of Experimental and Theoretical Physics* **109**, 700–706 October (2009).

[84] Bulleid, N. E., Skoff, S. M., Hendricks, R. J., Sauer, B. E., Hinds, E. A., and Tarbutt, M. R. *Physical Chemistry Chemical Physics* **15**, 12299 (2013).

[85] Kramida, A., Yu. Ralchenko, Reader, J., and NIST ASD Team. NIST Atomic Spectra Database (ver. 5.1), [Online]. Available: `http://physics.nist.gov/asd` [2013, September 26]. National Institute of Standards and Technology, Gaithersburg, MD., (2013).

[86] Kimball, D. F., Clyde, D., Budker, D., DeMille, D., Freedman, S. J., Rochester, S., Stalnaker, J. E., and Zolotorev, M. *Physical Review A: Atomic, Molecular, and Optical Physics* **60**, 1103–1112 August (1999).

[87] Willey, D. R., Crownover, R. L., Bittner, D. N., and de Lucia, F. C. *The Journal of Chemical Physics* **89**, 1923–1928 August (1988).

[88] DePaul, S., Pullman, D., and Friedrich, B. *The Journal of Physical Chemistry* **97**(10), 2167–2171 (1993).

[89] Smith, R. A., Ditmire, T., and Tisch, J. W. G. *Review of Scientific Instruments* **69**, 3798–3804 November (1998).

[90] Ghazarian, V., Eloranta, J., and Apkarian, V. A. *Review of Scientific Instruments* **73**, 3606–3613 October (2002).

[91] Anderson, J. B. and Fenn, J. B. *Physics of Fluids* **8**, 780–787 May (1965).

[92] Tarbutt, M. R., Hudson, J. J., Sauer, B. E., and Hinds, E. A. In *Cold Polar Molecules: Creation and Applications*. CRC Press March (2009).

[93] Tarbutt, M. R., Hudson, J. J., Sauer, B. E., Hinds, E. A., Ryzhov, V. A., Ryabov, V. L., and Ezhov, V. F. *Journal of Physics B Atomic Molecular Physics* **35**, 5013–5022 December (2002).

[94] Bethlem, H. L., Crompvoets, F. M., Jongma, R. T., van de Meerakker, S. Y., and Meijer, G. *Physical Review A* **65**(5), 053416 May (2002).

[95] Tarbutt, M. R., Hudson, J. J., Sauer, B. E., and Hinds, E. A. *Faraday Discussions* **142**, 37 (2009).

[96] Bethlem, H. L., Berden, G., van Roij, A. J. A., Crompvoets, F. M. H., and Meijer, G. *Physical Review Letters* **84**, 5744–5747 June (2000).

[97] Sawyer, B. C., Stuhl, B. K., Lev, B. L., Ye, J., and Hudson, E. R. *European Physical Journal D* **48**, 197–209 July (2008).

[98] Tarbutt, M. R. and Hinds, E. A. *New Journal of Physics* **10**(7), 073011 July (2008).

[99] Bulleid, N. E., Hendricks, R. J., Hinds, E. A., Meek, S. A., Meijer, G., Osterwalder, A., and Tarbutt, M. R. *Physical Review A: Atomic, Molecular, and Optical Physics* **86**(2), 021404 August (2012).

[100] Meek, S. A., Parsons, M. F., Heyne, G., Platschkowski, V., Haak, H., Meijer, G., and Osterwalder, A. *Review of Scientific Instruments* **82**(9), 093108 September (2011).

[101] Condon, E. U. *Physical Review* **32**, 858–872 December (1928).

[102] http://en.wikipedia.org/wiki/File:Franck-Condon-diagram.png.

[103] Shuman, E. S., Barry, J. F., Glenn, D. R., and DeMille, D. *Physical Review Letters* **103**(22), 223001 November (2009).

[104] Zhuang, X., Le, A., Steimle, T. C., Bulleid, N. E., Smallman, I. J., Hendricks, R. J., Skoff, S. M., Hudson, J. J., Sauer, B. E., Hinds, E. A., and Tarbutt, M. R. *Physical Chemistry Chemical Physics* **13**, 19013 (2011).

[105] Dunfield, K. L., Linton, C., Clarke, T. E., McBride, J., Adam, A. G., and Peers, J. R. D. *Journal of Molecular Spectroscopy* **174**(2), 433 – 445 (1995).

[106] http://www.hamamatsu.com/resources/pdf/etd/R2228_TPMH1062E01.pdf.

[107] Le Roy, R. J. University of Waterloo Chemical Physics Research Report CP -657R (2004).

[108] Tarbutt, M. R., Sauer, B. E., Hudson, J. J., and Hinds, E. A. *New Journal of Physics* **15**(5), 053034 May (2013).